Spring 2022

Bosonic Quantum Simulation in Circuit Quantum Electrodynamics

Christopher Shen Wang

Yale University Graduate School of Arts and Sciences, cswang93@gmail.com

Abstract

Bosonic Quantum Simulation in Circuit Quantum Electrodynamics

Christopher S. Wang

2022

The development of controllable quantum machines is largely motivated by a desire to simulate quantum systems beyond the capabilities of classical computers. Investigating intrinsically multi-level model bosonic systems, using conventional quantum processors based on two-level qubits is inefficient and incurs a potentially prohibitive mapping overhead in the current "near-term intermediate-scale quantum" (NISQ) era. This motivates the development of hybrid quantum processors that contain multiple types of degrees of freedom, such that one can leverage an optimal one-to-one mapping between the model system and simulator. Circuit quantum electrodynamics (cQED) has emerged as a leading platform for quantum information processing owing to the immense flexibility of engineering high fidelity coherent interactions and measurements. In cQED, microwave photons act as bosonic particles confined within a nonlinear network of electromagnetic modes. Controlling these photons serves as the basis for a hardware efficient platform for simulation of naturally bosonic systems. In this thesis, we present two experiments that encapsulate this idea by simulating molecular dynamics in two different regimes of electronic-nuclear coupling: adiabatic and nonadiabatic. In the first experiment, we implement a boson sampling protocol for estimating Franck-Condon factors associated with photoelectron spectra. Importantly, we fulfill the scalability requirement by developing a novel single-shot number-resolved quantum non-demolition detector for microwave photons. In the second experiment, we develop and employ a model for simulating dissipative nonadiabatic dynamics through a conical intersection as a basis for modeling photochemical reactions. We directly observe branching of a coherent wave-packet upon passage through the conical intersection, revealing the competition between coherent evolution and dissipation in this system. The tools developed for the experiments in this thesis serve as a basis for implementing more complex bosonic simulations.

Bosonic Quantum Simulation in Circuit Quantum Electrodynamics

A Dissertation
Presented to the Faculty of the Graduate School
of
Yale University
in Candidacy for the Degree of
Doctor of Philosophy

by
Christopher S. Wang

Dissertation Director: Robert J. Schoelkopf

May 2022

Contents

List of Figures

List of Tables

Acknowledgements

It is often illuminating to learn about the human elements of scientific research – how ideas are born from conversation, how collaborations are formed, and how individual scientists grow and mature. In the era of modern science, it is essentially a requirement that scientists work together to execute the most complex experiments to date that rely heavily on a tremendous foundation of knowledge and expertise. I have been very fortunate to work in a space that is founded on such collaboration and an open sharing of resources. Here, I would like to convey the immense support, generosity, wisdom, and friendship that I have received from those around me over the course of my PhD.

I am primarily indebted to my advisor Rob Schoelkopf, who placed a lot of trust in me and allowed me to freely explore my interests. Rob taught me the importance of conveying a concise and distinctive message, though I am perhaps still learning to be as confident as he would like me to be. Rob also deserves credit for 1) bringing together a wonderful group of individuals that define the collaborative culture of the lab and 2) providing the resources for all members of his group to do cutting-edge science[1].

These two facets are quite literally doubled thanks to Michel Devoret, and the result is a scientific community and environment that fosters success for every participant. Michel's knowledge and expertise runs deep and his door is usually open for insightful scientific discussions. In particular, I am grateful to Michel for sowing the seeds for my final experiment and allowing me to take full ownership.

Liang Jiang and Steve Girvin have been wonderful theorist collaborators, rounding out the quantum information science community at Yale for the majority of my PhD. Liang has a cheer and optimism to him that is matched by his clever ideas that guided many experiments in recent years until his departure in in 2019. Steve shares Liang's kind demeanor and is an excellent communicator of complex ideas. I trust Steve deeply and am grateful to have had the opportunity of working with him.

Rob and Michel's groups would not function if not for Luigi Frunzio. In addition to

managing the fabrication equipment, facilitating administrative tasks, and contributing to various research projects, Luigi has an unbounded enthusiasm that he shares with every member of the fourth floor of Becton, often in the form of amusing anecdotes.

The administrators of Applied Physics welcomed me with open arms since my arrival in the summer of 2015. Thanks to Giselle Maillet, Terri Evangeliste, Nuch Graves, and Maria Rao for creating a cheerful and laid back atmosphere that allowed everyone to momentarily take their mind off science in stressful times. This graciousness extends to Stephanie Hessing, Florian Carle, and Racquel Miller of the Yale Quantum Institute.

Jacob Blumoff and Kevin Chou adopted me when I first joined the lab and showed me the world of experimental superconducting quantum computing research. They allowed me to be involved in every stage of their final experiment and made me feel like a genuine part of their team, even though I had a lot to learn. I am grateful for their mentorship and am happy that Kevin has remained in New Haven as a close friend, though I can hear Jacob cheering me from afar and preaching about exchange-only spin qubits.

One day in the summer of 2017, Rob introduced me to Sal Elder and tasked me with advising him on an exciting experiment proposed by Connor Hann and Liang. Sal made me prove to him that I knew what I thought I knew, and it turned into one of the most challenging but rewarding mentor-mentee relationships of my graduate career. For this, I thank Sal deeply. It has also been a pleasure to work with Connor, who manages to convey deep wisdom in the calmest of manners.

Brian Lester, in many ways, defined the course of my PhD. He brought the ideas of quantum simulation to Rob's group, and it was immediately clear to me that I was hooked. Moreover, Brian was and continues to be one of the kindest people I have gotten the pleasure of knowing and working with, which was just as impactful on me as his scientific prowess. His abrupt departure was bittersweet, but in retrospect he provided me with complete ownership and agency for what would ultimately become this thesis.

Brian's ideas set the stage for a large collaborative effort between engineers, physicists, and chemists, which resulted in the first experiment of this thesis. Our discussions were a valuable opportunity for me to experience interdisciplinary collaboration. I am grateful to have worked primarily with Jacob Curtis. Jacob is open to new ideas, thorough in his understanding, and overall a great person to do research with. Moreover, he provided a lot of software infrastructure that made our lives as smooth as can be. It was also a pleasure to work with Yaxing Zhang, whose elegant theory managed to explain essentially every feature of our experiment. Thanks to Jessica Freeze, Victor Batista, Lidor Foguel, Zachary Vealey, and Patrick Vaccaro for providing indispensable chemistry insight, calculations, and support that made our work possible. I was extremely fortunate to interact with Ike Chuang in a professional setting. Ike has effectively served as an external mentor, instilling me with a confidence that has had a deep impact on my graduate career.

I am grateful for Ben Chapman for being a solid mentor, friend, labmate, and basketball

Chapter 1

Introduction

It is difficult to overstate the impact of computer simulations on modern scientific discovery and technological development, as they provide a simple and time efficient way to predict the behavior or performance of an otherwise unexplored system. The first use of computer simulations dates back to as early as the Manhattan Project era, where Monte Carlo methods were developed and deployed for understanding neutron diffusion. Since then, the capabilities of computer simulations have tracked closely with the exponentially growing computational power of modern transistor-based digital computers. Central to these simulations are a combination of powerful computational machines and successful physical and empirical theories, connected together via algorithms.

In parallel, the advent of quantum mechanics in the 20th century as a more complete theory of nature has led us not only to a deeper understanding of the physical world, but also to the invention of a staggering number of modern technologies. Lasers and atomic clocks rely on the discrete nature of atomic transitions. Nuclear magnetic resonance, which is at the heart of magnetic resonance imaging, is based on the intrinsically quantum mechanical spin of atomic nuclei. The understanding of band gaps in semiconductors ultimately led to the transistor, which one can arguably claim provides the backbone of modern society.

Despite the resounding success of quantum mechanics, there are still mechanisms in nature that are not well understood, such as the specific reaction pathways of biological catalysts and the physical origin of high-temperature superconductivity. This is in part due

to a fundamental property of quantum mechanics, first noted by Richard Feynman in 1982 — the computational cost of simulating quantum systems on a classical computer grows *exponentially* with system size [Feynman 1982]. A solution to this problem would be a new type of computer; one that fundamentally operated via the rules of quantum mechanics as opposed to classical logic. Specifically, it would operate on quantum bits, or qubits, as opposed to classical bits.

Subsequent developments in the next decade or so crystallized the utility of such a machine and brought the idea of a quantum computer to the forefront of scientific research. Most notably, Peter Shor developed a quantum integer factorization algorithm in 1994 that could break current public-key encryption schemes [Shor 1994; Steane 1996]. Many more quantum algorithms followed suit, including ones that may truly provide a new paradigm for computational chemistry [Aspuru-Guzik et al. 2005], further confirming the advantages that would come with such a machine.

It was not at all obvious, however, that a quantum computer could practically be built. Preserving quantum information is much more difficult than preserving classical information, since it requires complete isolation of the qubits from their environment. Add on the requirement of manipulating and measuring many qubits in a fully controlled manner, and the task seems insurmountable — how could you possible isolate and control a large set of qubits at the same time? Fortunately, the advent of quantum error correction (QEC) [Shor 1995] gave hope and life to the field. Thus initiated worldwide investment towards building a quantum computer.

In the two decades or so since then, tremendous theoretical and experimental progress has brought us closer to not only building a quantum computer, but developing and harnessing a new generation of quantum technologies. This places us in the so-called "second quantum revolution", where we are able to fully control the quantum state of a system for not just computation, but also simulation, communication, and sensing. In fact, these efforts have birthed the interdisciplinary field of quantum information science — spanning physics, computer science, engineering, and materials science.

It is natural to ask: Where are we now, collectively, as a field? How far away is a quantum machine that can transform our lives? On one hand, progress has been rapid. We now

are able to quite faithfully control and measure individual qubits across a wide range of experimental platforms such as (in no particular order) trapped ions, neutral atoms, semiconductor electron spins, and superconducting circuits, facilitated by modern advances in technologies such as lasers, vacuum systems, control electronics, nanofabrication, and cryogenics. Notably, control of $\sim$50 qubits has been recently demonstrated with both neutral atoms [Bernien et al. 2017] and superconducting circuits [Arute et al. 2019], which has respectively implemented simulation and computational tasks at the brink of the capabilities of modern supercomputers.

On the other hand, the gap between where we are now and implementing large scale algorithms of practical relevance is still quite substantial. This is primarily due to the staggering difficulty of performing QEC, owing to stringent requirements on gate and measurement fidelities in a large scale processor. It is for this reason that to this day, implementing QEC in a manner than significantly *improves* performance of a quantum processor compared to operating on its native qubits has yet to be demonstrated.

Rather than seeing a long and arduous road ahead, it is insightful to consider the ways in which progress has been made thus far. The development of superconducting qubits is particularly illuminating, which we elaborate on in Chapter 3. One of the most notable breakthroughs was the development of the transmon qubit in 2007 here at Yale [Koch et al. 2007], offering an elegantly *simple* architecture for a high-performance qubit that has made it ubiquitous among both academic and industrial groups. Combining this idea with a refined fabrication process, sophisticated control electronics, and meticulous calibration strategies has led to experiments that challenge the computational power of modern supercomputers [Arute et al. 2019; Wu et al. 2021]. This exemplifies how progress is made by combining clever, creative, and ideally simple ideas with careful, meticulous, and impressive engineering.

A core tenet of the research philosophy at Yale is developing and refining novel approaches to quantum information processing that may have tangible benefits in the long run. The most recent instance of this approach is the pioneering of bosonic quantum error correction, where information is stored and manipulated in quantum harmonic oscillators as opposed to qubits. The key idea is hardware efficiency, where a single quantum har-

monic oscillator mode can encode a logical error-correctable qubit as opposed to using many physical qubits, potentially reducing the hardware overhead. This approach has led to many wonderful experiments that not only hold promise with regards to performance, but have offered an elegant and expanded framework for understanding QEC.

This thesis draws inspiration from bosonic QEC and aims to apply the same underlying concept of hardware efficiency to problems in quantum simulation. The experimental techniques developed in this thesis continue to push the boundaries of novel control and measurement schemes that our superconducting platform is capable of. Most importantly, the capabilities are sophisticated enough to motivate the experimental investigation of simple models of realistic chemical phenomena.

1.1   Outline of this thesis

We begin with a brief introduction to quantum computational chemistry in Chapter 2, which provides the basis for a general class of Hamiltonians which we will consider in this thesis. For both context and completeness, we highlight modern approaches for solving the electronic structure problem using quantum hardware.

Next, we attempt a comprehensive yet concise overview of our programmable bosonic quantum simulator in Chapter 3, which begins with introducing the fundamentals of bosons and how to control and characterize them. We then provide a historical account of circuit quantum electrodynamics, highlighting the most notable developments that steered the platform to where it is today. Finally, we present the specific device that we will be utilizing and describe both old and new techniques developed for such an architecture. Much of this chapter leans heavily on the work of those who have come before me, as I attempt to summarize a monumental amount of hard work which has enabled the experiments of this thesis.

The following two chapters describe the two main experiments this thesis is centered on. These experiments aim to model dynamical processes in molecular systems upon interaction with light. The first experiment, described in Chapter 4, considers what happens in photoelectron spectroscopy when there is significant vibronic coupling between two distinct

adiabatic potential energy surfaces. The output spectrum contains peaks with varying intensities, known as Franck-Condon factors, which we efficiently estimate by sampling directly from our programmable bosonic simulator. Importantly, we fulfill the scalability requirement by developing the first single shot photon number resolving detector in the microwave domain. The second experiment, described in Chapter 5, is inspired by a prominent photochemical reaction in nature — *cis-trans* isomerization of rhodopsin — which is central to vision. In this case, an optically excited wave-packet rapidly evolves towards a so-called conical intersection, proceeding to branch towards a reactant or product configuration. We implement a minimal model of this reaction landscape in a hybrid qubit-boson simulator and directly observe wave-packet branching upon passage through the conical intersection, revealing the competition between coherent evolution and dissipation in a strongly interacting system.

Finally, we conclude in Chapter 6 with a few perspectives and potential future directions.

Chapter 2

Quantum computational chemistry

Along the same timeline of the development of quantum mechanics and modern computers, computational chemistry emerged as an indispensable component of chemistry. Facing the same fundamental bottleneck as physicists, chemists needed to invent clever schemes to analyze and predict the behavior of increasingly larger and more complex systems. Great progress has been made, with the advent of techniques such as density functional theory (DFT) and Car-Parrinello molecular dynamics [Car and Parrinello 1985] pushing the boundaries of what kinds of calculations are possible and representing much of the current state-of-the-art. Nevertheless, outstanding challenges still remain. Leveraging quantum algorithms is a promising approach moving forward, but still requires further theoretical and experimental research to be truly impactful. Examples include accurate calculations of electronic energies of transition states in chemical reactions which may elucidate reaction mechanisms and inform the design of artificial catalysts.

The experiments in this thesis are concerned with simulating interacting molecular electronic and nuclear degrees of freedom in various regimes on quantum hardware. As such, this chapter is divided into two main sections. Section 2.1 provides an overview of the full molecular Hamiltonian. We begin by reviewing the basic formalism for the electronic structure problem in the Born-Oppenheimer regime, and proceed to further quantize the nuclear motion as well. We then consider situations where the Born-Oppenheimer separation is invalid and introduce a model for analyzing such systems. Finally, we discuss the time-dependent problem associated with photochemical processes. Section 2.2 discusses, at

a high level, the primary considerations for using quantum hardware to address quantum chemistry. For the sake of completeness, we provide an overview of electronic structure methods on quantum computers, though this thesis is not focused on performing these types of calculations on quantum hardware.

2.1 The molecular Hamiltonian

In atomic units, the Hamiltonian for a molecule consisting of N_e electrons and N_n nuclei is

$$\mathcal{H} = \underbrace{-\sum_{i=1}^{N_e} \frac{1}{2}\nabla_i^2}_{T_e(\partial_{\vec{r}})} \underbrace{-\sum_{\alpha=1}^{N_n} \frac{1}{2M_\alpha}\nabla_\alpha^2}_{T_n(\partial_{\vec{R}})} + \underbrace{\sum_{i=1}^{N_e}\sum_{j>i}^{N_e} \frac{1}{|\vec{r}_i - \vec{r}_j|}}_{V_{ee}(\vec{r})} - \underbrace{\sum_{i=1}^{N_e}\sum_{\alpha=1}^{N_n} \frac{Z_\alpha}{|\vec{r}_i - \vec{R}_\alpha|}}_{V_{en}(\vec{r},\vec{R})} + \underbrace{\sum_{\alpha=1}^{N_n}\sum_{\beta>\alpha}^{N_n} \frac{Z_\alpha Z_\beta}{|\vec{R}_\alpha - \vec{R}_\beta|}}_{V_{nn}(\vec{R})}$$

$$(2.1)$$

which is simply the sum of kinetic energies T and pairwise Coulomb interaction energies V of the electrons with positions $\vec{r}_i$ and nuclei with positions $\vec{R}_\alpha$. Here, M_α are the nuclear masses expressed in units of the electron mass m_e, and $\{Z_\alpha\}$ are atomic numbers. At a glance, solving the time-independent Schrödinger equation for $\mathcal{H}$ appears to be quite challenging — there in general is no way to rigorously separate the electronic and nuclear degrees of freedom. Moreover, molecular dynamics corresponding to photochemical processes will necessarily require a time-dependent treatment involving interactions with light, further expanding the scope of the problem.

2.1.1 Electronic structure in the Born-Oppenheimer regime

Fortunately, the pioneering work of Born & Oppenheimer provided an elegant framework to simplify the treatment of $\mathcal{H}$ in a way that not only simplified the calculations (though they are still extremely difficult), but also offered an intuitive way to visualize molecular states and dynamics [Born and Oppenheimer 1927]. The central task is to solve the non-relativistic time-independent Schrödinger equation

$$\mathcal{H}\Psi(\vec{r}, \vec{R}) = E\Psi(\vec{r}, \vec{R}) \tag{2.2}$$

for the molecular Hamiltonian $\mathcal{H}$. The typical starting point for solving Eq. (2.2) relies on a bit of intuition: nuclei are much heavier than electrons and therefore should move more slowly, suggesting that the motion may be decoupled to some degree. The approach of Born & Oppenheimer is to cast the Hamiltonian in terms of a dimensionless parameter $\kappa = \left(\frac{m_e}{\bar{M}}\right)^{\frac{1}{4}}$ of an average nuclear mass $\bar{M}$:

$$\mathcal{H} = \mathcal{H}_e + \kappa^4 \mathcal{H}_1 \tag{2.3}$$

where

$$\mathcal{H}_e = T_e(\partial_{\vec{r}}) + V_{ee}(\vec{r}) + V_{en}(\vec{r}, \vec{R}) + V_{nn}(\vec{R}) \tag{2.4}$$

$$\mathcal{H}_1 = \sum_{\alpha=1}^{N_n} \left(\frac{\bar{M}}{M_\alpha}\right) \frac{1}{2m_e} \nabla^2_\alpha \tag{2.5}$$

One can first solve the time-independent Schrödinger equation for $\mathcal{H}_e$ assuming the nuclear positions are fixed at $\vec{R}$:

$$\mathcal{H}_e \varphi_n(\vec{r}, \vec{R}) = \varepsilon_n(\vec{R}) \varphi_n(\vec{r}, \vec{R}) \tag{2.6}$$

and obtain a set of eigenenergies $\varepsilon_n(\vec{R})$ and eigenfunctions $\{\varphi_n(\vec{r}, \vec{R})\}$, where n is an electronic quantum number. As we will see later, $\varepsilon_n(\vec{R})$ can be interpreted as a *potential energy surface* for nuclear motion. In order to solve for the nuclear motion, we will need to go back and solve the Schrödinger equation for the full molecular Hamiltonian that includes the nuclear kinetic energy operator.

2.1.2 Solving for nuclear motion

Intuitively, we expect molecules to have stable nuclear configurations, i.e., local minima around which nuclear motion such as vibrations and rotations can be confined. Thus, we define a small nuclear displacement $\kappa \vec{u} = \vec{R} - \vec{R}_0$ relative to some reference position $\vec{R}_0$ that allows us to expand the electronic Hamiltonian, eigenenergies, and eigenfunctions in

powers of κ:

$$\mathcal{H}_e(\vec{r}, \partial_{\vec{r}}, \vec{R}) = \mathcal{H}_e(\vec{r}, \partial_{\vec{r}}, \vec{R}_0 + \kappa\vec{u}) = \mathcal{H}_e^{(0)}(\vec{R}_0) + \kappa\mathcal{H}_e^{(1)} + \kappa^2\mathcal{H}_e^{(2)} + \kappa^3\mathcal{H}_e^{(3)} + ... \quad (2.7)$$

$$\varepsilon_n(\vec{R}) = \varepsilon_n(\vec{R}_0 + \kappa\vec{u}) = \varepsilon_n^{(0)}(\vec{R}_0) + \kappa\varepsilon_n^{(1)} + \kappa^2\varepsilon_n^{(2)} + ... \quad (2.8)$$

$$\varphi_n(\vec{r}, \vec{R}) = \varphi_n(\vec{r}, \vec{R}_0 + \kappa\vec{u}) = \varphi_n^{(0)}(\vec{r}, \vec{R}_0) + \kappa\varphi_n^{(1)} + \kappa^2\varphi_n^{(2)} + ... \quad (2.9)$$

where $f^{(n)}$ depends on a nth order polynomial in $\vec{u}$. By expressing the nuclear kinetic energy operator in terms of $\vec{u}$ and adding its contribution to Eq. (2.7), we get an expansion for the full Hamiltonian $\mathcal{H}$:

$$\mathcal{H}(\vec{r}, \partial_{\vec{r}}, \vec{R}) = \mathcal{H}_e^{(0)} + \kappa\mathcal{H}_e^{(1)} + \kappa^2\big(\mathcal{H}_e^{(2)} + \mathcal{H}_1^{(2)}\big) + \kappa^3\mathcal{H}_e^{(3)} + ... \quad (2.10)$$

where we see that the nuclear kinetic energy appears only in the second order term. Finally, we can expand the full energy and wavefunctions of Eq. (2.2):

$$E_n \approx \varepsilon_n^{(0)} + \kappa E_n^{(1)} + \kappa^2 E_n^{(2)} + ... \quad (2.11)$$

$$\Psi_n \approx \Psi_n^{(0)} + \kappa\Psi_n^{(1)} + \kappa^2\Psi_n^{(2)} + ... \quad (2.12)$$

and solve the Schrödinger equation order by order in κ. By assuming an ansatz for the zeroth order full wave-function of the form

$$\Psi_n^{(0)}(\vec{r}, \vec{u}) = \varphi_n^{(0)}(\vec{r}, \vec{R}_0)\chi^{(0)}(\vec{u}) \quad (2.13)$$

we can write out the equations up to second order (demanding that the first order contribution to the energy vanishes at a local minimum) and integrate over the electronic eigenfunctions to get a reduced equation for $\chi^{(0)}(\vec{u})$:

$$\kappa^2\big(\mathcal{H}_1^{(2)}(\partial_{\vec{u}}) + \varepsilon_n^{(2)}\big)\chi^{(0)}(\vec{u}) = \kappa^2 E_n^{(2)}\chi^{(0)}(\vec{u}) \quad (2.14)$$

This is the well-known *harmonic approximation* for nuclear motion, and as such we are now able to interpret $\chi^{(0)}(\vec{u})$ as a nuclear wavefunction. Accordingly, the electronic energies
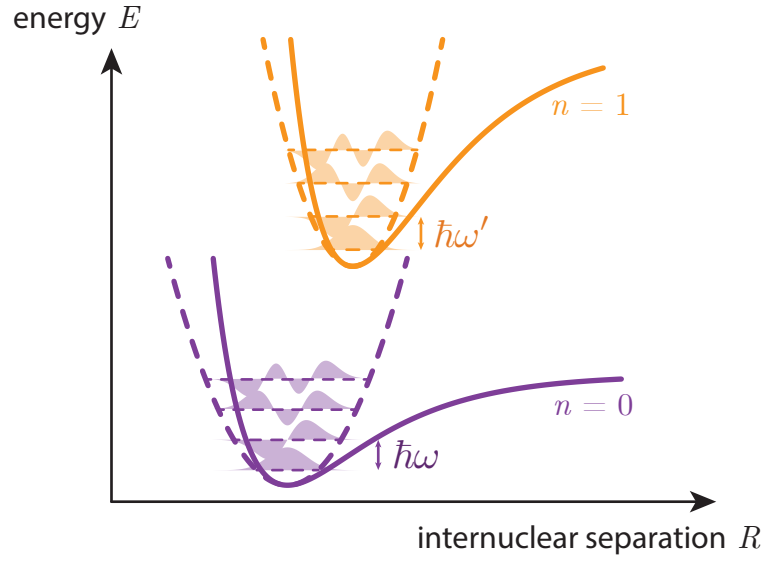
Figure 2.1 | **Potential energy surfaces for a diatomic molecule.** Two electronic states modeled with Morse potentials $\varepsilon(R) = V_{\mathrm{morse}}(R) = \frac{V_0}{2\alpha^2}(e^{-\alpha R} - 1)^2$ along with harmonic approximations (dashed surface) for the single vibrational degree of freedom, resulting in frequencies ω and ω' for the ground and excited potentials, respectively.

$\{\varepsilon_n(\vec{R})\}$ define *potential energy surfaces* for the nuclei (Fig. 2.1). The full zeroth order wavefunction may then be written as:

$$\Psi_n^{(0)}(\vec{r}, \vec{u}) = \varphi_n^{(0)}(\vec{r}, \vec{R}_0)\chi_n^{(0)}(\vec{u}) \tag{2.15}$$

Furthermore, by solving the second order equations for the wavefunctions and collecting all second order terms, the full wave-function can be written as:

$$\Psi_n(\vec{r}, \vec{u}) = \left(\chi^{(0)}(\vec{u}) + \kappa\chi^{(1)}(\vec{u}) + \kappa^2\chi^{(2)}(\vec{u})\right)\varphi_n(\vec{r}, \vec{R}) \tag{2.16}$$

This separable form of the nuclear and electronic wavefunctions is what is known as the *adiabatic approximation*, which describes how the electronic eigenfunctions themselves depend on the nuclear displacements and will correspondingly track with the nuclear motion without transitioning to other electronic states. Clearly, the harmonic approximation falls within the adiabatic approximation.

Finally, one can show that nuclear rotations can also be treated via these perturbative

methods and come in at the level of the fourth order equations, but are typically much lower in energy than vibrations especially for larger molecules. In general, a (linear) molecule will have $3N_n - (5)6$ vibrational degrees of freedom, with the rest being attributed to translations and rotations.

2.1.3 Beyond Born-Oppenheimer

When does the adiabatic Born-Oppenheimer approximation fail? To answer this question, we begin with the Born-Oppenheimer ansatz for a full molecular eigenfunction $\Psi_k(\vec{r}, \vec{R})$:

$$
\begin{aligned}
\Psi_k(\vec{r}, \vec{R}) &= \sum_{ij} c_{ij}^k \varphi_i(\vec{r}, \vec{R}) \chi_{ij}(\vec{R}) \\
&= \sum_i \varphi_i(\vec{r}, \vec{R}) h_i^k(\vec{R})
\end{aligned}
\tag{2.17}
$$

where we have integrated over the nuclear quantum numbers $\{j\}$ to define $h_i^k(\vec{R})$. At this point, we have an exact expansion if a full basis is considered. By substituting Eq. (2.17) into Eq. (2.2) and integrating both sides of the equation by $\varphi_j^*(\vec{r}, \vec{R})$, we arrive at:

$$
\left(T_n + \varepsilon_j(\vec{R})\right) h_j(\vec{R}) - \sum_i \Lambda_{ji} h_i(\vec{R}) = E_k h_j(\vec{R})
\tag{2.18}
$$

where

$$
\Lambda_{ji} = \delta_{ji} T_n - \langle \varphi_j(\vec{R}) | T_n | \varphi_i(\vec{R}) \rangle
\tag{2.19}
$$

are *non-adiabatic coupling terms* that arise from the action of the nuclear kinetic energy operator on the electronic eigenfunctions. One can show that these expectation values include terms of the form:

$$
\frac{\left\langle \varphi_j(\vec{r}, \vec{R}) \middle| \nabla_R \mathcal{H}_e \middle| \varphi_i(\vec{r}, \vec{R}) \right\rangle_{\vec{r}}}{\varepsilon_j(\vec{R}) - \varepsilon_i(\vec{R})}
\tag{2.20}
$$

which diverge as one approaches a degeneracy of the adiabatic potential energy surfaces. In the vicinity of such degeneracies, the adiabatic electronic basis fails to be an appropriate basis for calculations and analyses. We note that if the non-adiabatic coupling terms can be neglected, this framework is another way one can arrive at the Born-Oppenheimer

approximation of the molecular wavefunction.

Given the aforementioned issue, one can consider instead a diabatic electronic basis $\phi_k(\vec{r})$ such that the molecular wave-function can be expressed as

$$\Psi(\vec{r}, \vec{R}) = \sum_k \phi_k(\vec{r})\chi'_k(\vec{R}) \tag{2.21}$$

where the diabatic states are, by definition, diagonal in the nuclear kinetic energy operator. Off-diagonal couplings between electronic states must of course exist, but now they arise via the potential $\langle \phi_j | \hat{V}(\vec{r}, \vec{R}) | \phi_i \rangle$ and do not involve wave-function derivatives.

This forms the basis for a general vibronic coupling Hamiltonian [Domcke, Yarkony, and Köppel 2004]:

$$\mathcal{H}_{\text{vc}} = \sum_n |\phi_n\rangle \left(T_n + W_{nn}(\vec{R}) \right) \langle \phi_n| + \sum_{n \neq m} |\phi_n\rangle W_{nm}(\vec{R}) \langle \phi_m| \tag{2.22}$$

where $W_{nm}(\vec{R})$ are matrix elements of the electronic Hamiltonian in the diabatic basis. We will use this formulation explicitly for our reaction model in Chapter 5.

2.1.4 Vibronic spectroscopy and molecular dynamics

Spectroscopy is at the heart of light-matter interactions and is central to the physical sciences. In the context of chemistry, spectroscopy provides a method in which to extract information regarding the internal structure of a molecule with respect to its surrounding environment. There are many different types of spectroscopy given the many different energy scales involved in molecular motion. Here, we consider a class of spectroscopy known as *vibronic spectroscopy* aimed at probing vibrational-electronic (vibronic) couplings between distinct electronic states. This framework also applies to ioniziation processes, where the final electronic state is the ground electronic state of an ionized molecule.

We begin with a simple theoretical description of a single isolated diatomic molecule interacting with a light field, giving rise to some sort of spectrum in the frequency domain. Following the scenario depicted in Fig. 2.1, we have adiabatic separation between two potential energy surfaces and can write the full Hamiltonian in a subspace of two electronic

states which we denote as ground and excited $\{|g\rangle, |e\rangle\}$ as:

$$\mathcal{H} = |g\rangle\langle g| \otimes \mathcal{H}_{\text{vib}}^g + |e\rangle\langle e| \otimes \mathcal{H}_{\text{vib}}^e \qquad (2.23)$$

where $\mathcal{H}_{\text{vib}}^{g/e}$ are vibrational Hamiltonians on the nuclear Hilbert space. Under the electric dipole approximation, which is valid in the limit that the wavelength of a monochromatic light field is much larger than the extent of the molecule, the interaction is

$$\hat{V}(t) = -\hat{\mu} \cdot \hat{E}(t) \qquad (2.24)$$

where the dipole operator is $\hat{\mu} = \sum_j q_j \hat{r}_j$ accounts for *all* the charges in the system, including those of the nuclei. Expressed in the reduced electronic subspace, we can write the transition dipole matrix elements:

$$\hat{\mu} = \begin{pmatrix} 0 & \mu_{eg}(R) \\ \mu_{ge}(R) & 0 \end{pmatrix} \qquad (2.25)$$

where in general $\mu_{ij}(\vec{R}) = \left\langle \varphi_i(\vec{r}, \vec{R}) \middle| \hat{\mu} \middle| \varphi_j(\vec{r}, \vec{R}) \right\rangle_{\vec{r}}$ depends on the nuclear coordinates. Under the Condon approximation, which describes an electronic transition that occurs on a timescale much faster than nuclear motion, the transition dipole matrix elements can be taken to be constant.

$$\mu_{ge}(R) = \mu_{eg}(R) = \mu \qquad (2.26)$$

This corresponds to a so-called "vertical" transition, where a nuclear wave-packet instantly jumps to a different electronic surface but remains in the same position.

Given this framework, how should one proceed to interpret an experimental spectrum? To be concrete, we consider a technique called laser-induced fluorescence (LIF). LIF operates by scanning the frequency of a laser directed at an ensemble of molecules (ideally as a very dilute gas in vacuum) in the vicinity of a target electronic transition. Any absorption of the light by the molecules will be followed shortly thereafter by isotropic spontaneous emission, which is then detected and ultimately translated to a relative intensity. In the
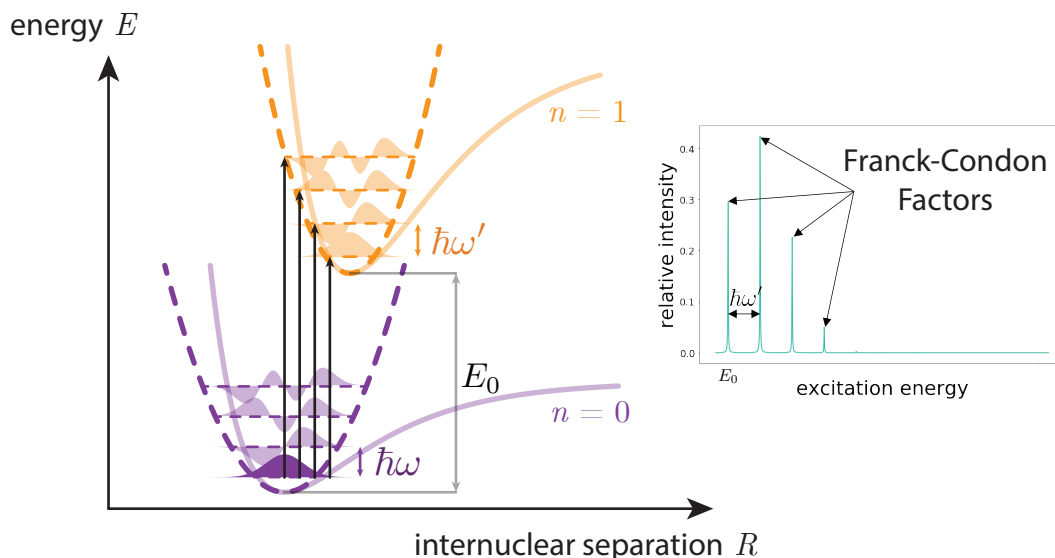
Figure 2.2 | **Modeling laser-induced fluorescence (LIF) spectra.** Under the harmonic approximation, molecules initially in the rovibrational ground state of an electronic ground state are vertically excited to an electronic excited state. The resulting spectrum (depiction not to scale) will have peaks whose relative amplitudes, known as Franck-Condon factors, are proportional to the wave-function overlap between the initial state and the final set of vibrational eigenstates in the electronic excited state.

case where the laser is far off resonance from any transition, there will be no intensity at the output.

An intuitive way to understand the resulting spectrum is shown in Fig. 2.2, where the peak intensities are called *Franck-Condon factors* (FCFs) and are equivalent to the wave-function overlap between an initial vibrational state $|\chi_g(0)\rangle$ in the electronic ground state and the complete set of vibrational states in the electronic excited state $\{|\chi_e^i\rangle\}$. The idealized spectrum can be described as:

$$\Sigma(\omega) = \sum_i \underbrace{|\langle \chi_e^i | \chi_g(0) \rangle|^2}_{\text{FCFs}} \delta(\hbar\omega - E_e^i) \tag{2.27}$$

The FCFs encode information about the structural relationship between the two potential energy surfaces. Historically, an approach to interpreting absorption spectra of small molecules amounted to fitting FCFs computed for various geometries to the experimental data.

14

A more elegant and encompassing approach is to consider a time-domain description [Heller 1981], where the absorption cross section can be written as:

$$\Sigma(\omega) = \int_{-\infty}^{\infty} e^{i\omega t} \langle \varphi(0)|\varphi(t) \rangle dt \qquad (2.28)$$

which is simply the Fourier transform of the state autocorrelation function. This representation is nice because it encodes more information than just the peak intensities and demonstrates how a spectrum emerges from recurrences in the autocorrelation function. One can utilize a quantum processor to directly measures this autocorrelation function, though it requires conditional multi-mode bosonic Hamiltonian propagation and effectively amounts to implementing a phase estimation algorithm. In the near term, such approaches will likely be coherence-limited.

2.2 Quantum chemistry on quantum computers

In order to use a quantum computing device to address quantum chemistry problems, one must first determine how to map the problem onto the hardware. For electronic structure, this requires a choice of basis for the atomic orbitals. We first briefly review this in section 2.2.1 from the domain of classical computational chemistry as they will readily apply to the quantum case. Next, the central constraint that we need to enforce is the anti-symmetrization of the wave-function under particle exchange due to the fact that we are dealing with indistinguishable fermions. Broadly speaking, there are two approaches that satisfy this requirement when using a qubit-based architecture. *First quantization* methods will enforce anti-symmetry via the wave-function, whereas *second quantization* places this constraints instead on field operators. We focus on second quantization methods as they have found the most success for various algorithms executed on near-term devices, though decisively determining which approach is more efficient remains an open research question. Finally, because qubits are not fermions, the field operators need to be translated to qubit operators to complete the mapping process, which we discuss in section 2.2.2. This sets the stage to overview current theoretical and experimental progress on algorithms for quantum

chemistry in section 2.2.3.

2.2.1 Basis sets

The first step of any encoding scheme is to choose an appropriate basis $\{\phi\}$ to represent the atomic orbitals. This choice defines the Hilbert space for the computation, which contains N electrons. As a rule, the larger the basis used, the more accurate the computation will be.

For classical computational methods, the choice of a basis set is critical for obtaining the most accurate results possible for a given problem size, computational method, and available computational resources. Innovation in basis sets have significantly improved accuracy of classical computations, and is central to computational chemistry research. Qualitatively speaking, the complexity of the basis set increases as one either considers molecules with more electrons or desires a more accurate computation for a given molecule size.

While there are many choices for basis sets, two primitive $1s$-type orbitals are Slater-type functions and Gaussian-type functions [Szabo and Ostlund 2012]:

$$\phi_{1s}^{\mathrm{SF}}(\zeta, \vec{r} - \vec{r}_0) = \left(\frac{\zeta^3}{\pi}\right)^{\frac{1}{2}} e^{-\zeta|\vec{r} - \vec{r}_0|} \tag{2.29}$$

$$\phi_{1s}^{\mathrm{GF}}(\alpha, \vec{r} - \vec{r}_0) = \left(\frac{2\alpha}{\pi}\right)^{\frac{3}{4}} e^{-\alpha|\vec{r} - \vec{r}_0|^2} \tag{2.30}$$

where $\zeta(\alpha)$ is the Slater (Gaussian) orbital exponent. The $2p, 3d$, etc. extensions of these functions follow the same form, but multiplied against polynomial functions in the various Cartesian coordinates as determined by the angular momentum. Quantitatively, Slater-type functions are clearly superior to Gaussian-type functions in that they more accurately represent typical orbitals. From a computational perspective, however, performing integrals involving Slater-type functions is computationally demanding, whereas integrals of Gaussian-type functions are efficient owing to the fact that computing the product of Gaussians returns another Gaussian. Thus, a standard compromise that is made is to generate what are known as Slater-type orbitals using a linear combination of L primitive Gaussian functions (STO-LG). This way, one can more accurately represent a true Slater-type function

while retaining the efficient computational properties of using Gaussian functions.

A *minimal basis set* considers only one basis function per atomic orbital. One can go beyond this by considering n different basis functions per atomic orbital, denoted by $n-\zeta$ (colloquially referred to as double-zeta, triple-zeta, etc.). A common technique to reduce the number of basis functions is to use a split-valence approach, where core electron orbitals are represented by a single basis function, but all valence electrons are represented by multiple basis functions. Further accuracy can be obtained by introducing additional *polarization* functions, which are orbitals that have larger angular momentum than that of the highest valence electron, as well as *diffuse* functions, which are STOs with larger radial extent. Finally, additional virtual orbitals can be added as in the case of the well known Dunning's correlation consistent basis set [Dunning Jr 1989] to provide even more accuracy, including all of the aforementioned features. These basis sets can typically only be deployed for small molecules, such as for our experiment in Chapter 4.

2.2.2 Second quantization and fermion-to-qubit mappings

In the second quantization formalism, the molecular Hamiltonian can be expressed in terms of fermionic creation and annihilation operators $c_\alpha^{(\dagger)}$:

$$\mathcal{H} = \sum_{\alpha,\beta=1}^{L} t_{\alpha\beta} c_\alpha^\dagger c_\beta + \sum_{\alpha,\beta,\gamma,\delta=1}^{L} v_{\alpha\beta\gamma\delta} c_\alpha^\dagger c_\gamma^\dagger c_\delta c_\beta \tag{2.31}$$

where L denotes the number of spin-orbitals and $t_{\alpha\beta}$ and $v_{\alpha\beta\gamma\delta}$ are one- and two-body integrals:

$$t_{\alpha\beta} = \int d\vec{x} \phi_\alpha^*(\vec{x}) \left(-\frac{\nabla^2}{2} - \sum_\alpha \frac{Z_\alpha}{|\vec{r}_i - \vec{R}_\alpha|} \right) \phi_\beta(\vec{x}) \tag{2.32}$$

$$v_{\alpha\beta\gamma\delta} = \int d\vec{x}_1 d\vec{x}_2 \frac{\phi_\alpha^*(\vec{x}_1)\phi_\gamma^*(\vec{x}_2)\phi_\beta(\vec{x}_2)\phi_\delta(\vec{x}_1)}{|\vec{r}_1 - \vec{r}_2|} \tag{2.33}$$

where $\vec{x}_i = (\vec{r}_i, \sigma_i)$ is a combined spatial-spin coordinate of the ith electron. Importantly, a basis set needs to be chosen here as described in the previous section. The fermionic creation and annihilation operators obey the anticommutation relation $\{c_i, c_j^\dagger\} = c_i c_j^\dagger + c_j^\dagger c_i =$

δ_{ij} signaling the presence of a minus sign on the wave-function under particle exchange. Thus, for a given ordering of fermions, the creation and annihilation operators $\{c_i^{(\dagger)}\}$ encode information regarding both the occupation $f_i \in \{0, 1\}$ of site i and the parity $(-1)^{\sum_{j<i} f_i}$.

Any fermion-to-qubit mapping must encode both the occupation and parity information. As such, there are three mappings that accomplish this in qualitatively distinct ways. The Jordan-Wigner (JW) mapping [Jordan and Wigner 1928]:

$$
\begin{aligned}
c_i &= \sigma_i^- \otimes \sigma_z^{i-1} \otimes ... \sigma_z^0 \\
c_i^\dagger &= \sigma_i^+ \otimes \sigma_z^{i-1} \otimes ... \sigma_z^0
\end{aligned}
\tag{2.34}
$$

encodes the occupation of site i locally but the parity information nonlocally. In contrast, a parity mapping [Seeley, Richard, and Love 2012] can be used to do the opposite and encode the parity information locally at the cost of encoding the occupation information non-locally. Both of these schemes require $\mathcal{O}(L)$ qubit operations to implement the action of a single fermionic operator. Alternatively, the Bravyi-Kitaev (BK) mapping [Bravyi and Kitaev 2002] strikes a balance by encoding both the occupation and parity information nonlocally, which actually reduces the gate overhead from $\mathcal{O}(L)$ to $\mathcal{O}(\log(L))$.

Ultimately, regardless of which mapping is chosen, the molecular Hamiltonian can be cast in the form:

$$
\mathcal{H} = \sum_{i=1}^{\mathcal{O}(L^4)} h_i P_i
\tag{2.35}
$$

where P_i are strings of Pauli operators acting on up to all of the qubits in the system.

2.2.3 Quantum algorithms for quantum chemistry

We have now set the stage for reviewing progress on quantum chemistry algorithms. The task at hand is solving the time-independent Schrödinger equation for the molecular Hamiltonian Eq. 2.2 to obtain electronic energies to within *chemical accuracy*, which is defined to be roughly $1.6 \times 10^{-3}\text{Ha} \approx 0.043\text{eV}$. Qualitatively, this corresponds to the energy resolution required to predict chemical reaction rates at room temperature. The first blueprint for using a quantum computer for this task was introduced in [Aspuru-Guzik et al. 2005], which uses the phase-estimation algorithm for obtaining eigenvalues of Hermitian operators

[Lloyd and Braunstein 1999]. Native operation fidelities of modern quantum processors, however, are not high enough to implement such operations for even modest sized systems with reasonable success probabilities owing to gate depths that scale as $\mathcal{O}(L^5)$.

This challenge almost certainly needs to be addressed through quantum error correction, but one can ask whether or not alternative strategies exist for extracting what computational power is available to us via current noisy, intermediate-scale quantum (NISQ) machines [Preskill 2018]. The answer to this question is hybrid quantum-classical variational algorithms, first introduced for quantum chemistry in [Peruzzo et al. 2014] as the variational quantum eigensolver (VQE). The central idea is to leverage the variational principle:

$$\frac{\left\langle \psi(\vec{\theta}) \middle| \mathcal{H} \middle| \psi(\vec{\theta}) \right\rangle}{\langle \psi(\vec{\theta}) | \psi(\vec{\theta}) \rangle} \geq E_0 \tag{2.36}$$

to iteratively optimize a trial wave-function $\left| \psi(\vec{\theta}) \right\rangle$ parameterized based on an appropriately chosen ansatz to obtain an estimate of the true ground state energy. In the kth round of the optimization, the energy is determined by measuring and summing the individual Pauli terms of Eq. 2.35, which is then given to a classical optimizer to update the parameters $\vec{\theta}_{k+1}$. As long as the initial wave-function has a non-vanishing overlap with the true ground state, the algorithm should converge to a solution. This approach circumvents the need for large depth circuits and only requires a single state preparation and measurement step, but comes at the cost of requiring many measurements. For an extensive review of variational algorithms, we refer the reader to [McClean et al. 2016].

Perhaps the most popular ansatz is the unitary coupled-cluster (UCC) ansatz, derived from the corresponding classical method. The ansatz is parameterized as [McArdle et al. 2020]:

$$\hat{U}(\vec{\theta}) = e^{\hat{T} - \hat{T}^\dagger} \tag{2.37}$$

where $\hat{T} = \sum_i \hat{T}_i$ is typically truncated at single and double excitations (thus referred to as

UCCSD):

$$\hat{T}_1 = \sum_{i\in\text{virtual},\alpha\in\text{occupied}} t_{i\alpha}\hat{a}_i^\dagger\hat{a}_\alpha$$

$$\hat{T}_2 = \sum_{i,j\in\text{virtual},\alpha,\beta\in\text{occupied}} t_{ij\alpha\beta}\hat{a}_i^\dagger\hat{a}_j^\dagger\hat{a}_\alpha\hat{a}_\beta \qquad (2.38)$$

$$\hat{T}_3 = ...$$

Central to VQE is the choice of ansatz and mapping, which ultimately set how accurate a given implementation can be. Furthermore, one can employ various error mitigation strategies to improve the accuracy of the calculation, but at a further overhead in the number of measurements. These considerations certainly depend on the hardware, which may have native, high-fidelity entangling operations that one would like to leverage compared to other schemes.

We discuss a rough timeline of VQE implementations and highlight their respective achievements, hopefully to give the reader a sense of what progress has looked like in nearly the past decade. [Peruzzo et al. 2014] performed the first proof-of-principle experiment for the He-H$^+$ molecule using a photonic processor encoding two qubits. [O'Malley et al. 2016] went a step further and implemented a simulation of the H$_2$ molecule with two qubits under a BK mapping using a superconducting processor. They run both VQE and phase estimation, and their VQE implementation achieved chemical accuracy under the unitary coupled cluster (UCC) ansatz. [Kandala et al. 2017] takes a leap by expanding to six superconducting qubits, enabling a VQE algorithm on molecules as large as BeH$_2$. A number of new techniques are explored including a hardware-efficient ansatz and a compact encoding of only the relevant atomic orbitals, similar in spirit to the split-valence approach described previously. The results, however, fall short of chemical accuracy, though subsequent work on employing error mitigation techniques significantly improved these results [Kandala et al. 2019]. Meanwhile, [Hempel et al. 2018] uses a trapped-ion system of up to four qubits to perform VQE with a processor that has a native all-to-all connectivity, rendering certain operations more efficient. They investigate both the JW and BK mapping for H$_2$ and a reduced active space BK mapping for LiH, and identify challenges moving forward.

Finally, [Google AI Quantum and Collaborators 2020] takes another leap in the number of qubits by using up to 12 superconducting qubits to perform VQE on hydrogen chains with a number of error mitigation strategies to reach the chemical accuracy threshold, however only for a noninteracting Hartree-Fock ansatz.

It is clear that obtaining high-fidelity results with a scaled up system is the core research thrust, and they necessarily come with strategies that optimally leverage the hardware capabilities. However, there is also still a heavy need for theoretical developments. For instance, the while the UCC ansatz can be systematically expanded to include higher order correlation effects, doing so becomes prohibitively costly in the classical subroutines. To address this challenge, [Grimsley et al. 2019; Tang et al. 2021] developed a powerful adaptive VQE algorithm that discovers an ansatz on a case-by-case basis to optimally extract the maximum amount of correlation energy at each step. This directly addresses the eventual desire of VQE algorithms to apply to molecules of interest that have large correlation energies which are classically intractable to calculate. A more recent work developed and implemented the use of a quantum processor to aid in the more traditional approach of classical fermionic quantum Monte-Carlo calculations [Huggins et al. 2022], highlighting the persistent advances that are being made towards practical quantum computation for quantum chemistry.

Chapter 3

Engineering a programmable bosonic quantum simulator

This chapter is dedicated to the hardware used to perform the experiments in this thesis. Our approach is based on the idea of hardware efficiency, suggesting that we have an optimal one-to-one mapping between the degrees of freedom of the model system and our quantum simulator. As with any controllable quantum device, we require the ability to initialize meaningful states, enact desired transformations, and measure the relevant observables of interest, all with high fidelity.

Our boson of choice the microwave photon. We confine, manipulate, and detect these photons in a nonlinear superconducting circuit network under an architecture known as circuit quantum electrodynamics (circuit QED). By incorporating microwave drives into our system in carefully engineered ways, we are able to dress the nonlinearities in a fashion that enables a wide range of operations.

We take a moment to clarify a point on nomenclature. For us, "bosonic quantum simulation" refers to the fact that we are simulating physical models that contain bosonic excitations spanning multiple energy levels. Correspondingly, we manipulate multiphoton states that live in weakly nonlinear harmonic oscillators. This is to contrast, say, simulations of spin models, where the target Hamiltonian only includes Pauli operators, using strongly nonlinear oscillators (such as the transmon which we will introduce in section 3.2.2) in

a qubit regime confined to the lowest two energy levels. We mention this not to draw boundaries, but to clarify and contextualize the experiments of this thesis.

We begin with a brief review of bosons and their unique properties in section 3.1. For photons confined in electromagnetic modes, the quantum harmonic oscillator serves as the most appropriate basis for all of the physics described in this thesis. We discuss how one can characterize and visualize quantum states in oscillators through the use of Wigner functions. Finally, we introduce Gaussian transformations as an important class of operations for manipulating harmonic oscillator states. Section 3.2 describes a historical path towards a modern realization of a circuit QED architecture that enables the experiments of this thesis. This story follows the early developments of cavity QED to the advent of circuit QED nearly two decades ago. Since then, the hardware has steadily improved, along with our understanding of the platform, which has enabled the implementation of sophisticated control and measurement schemes. We discuss these schemes concretely in section 3.3, where we introduce our programmable simulator and discuss its capabilities.

3.1 An overview of bosons

Under the Standard Model, all elementary particles can be classified as either fermions or bosons, named after Italian and Indian physicists Enrico Fermi and Satyendra Nath Bose, respectively. The primary distinction between the two types of particles lies in their quantum statistics owing to indistinguishability; fermions obey Fermi-Dirac statistics and bosons obey Bose-Einstein statistics. Furthermore, fermions necessarily possess half-integer spin whereas bosons possess integer spin.

The identification of bosons, however, extends beyond elementary particles. For example, while the photon is considered an elementary particle and the quantum of the electromagnetic field, collective excitations such as phonons or magnons also obey Bose-Einstein statistics and are considered bosonic. Notably, all of these bosons are massless field excitations, and we will be simulating processes that do not conserve particle number. As such, we begin by introducing the simplest framework and starting point for understanding these excitations: the quantum harmonic oscillator.
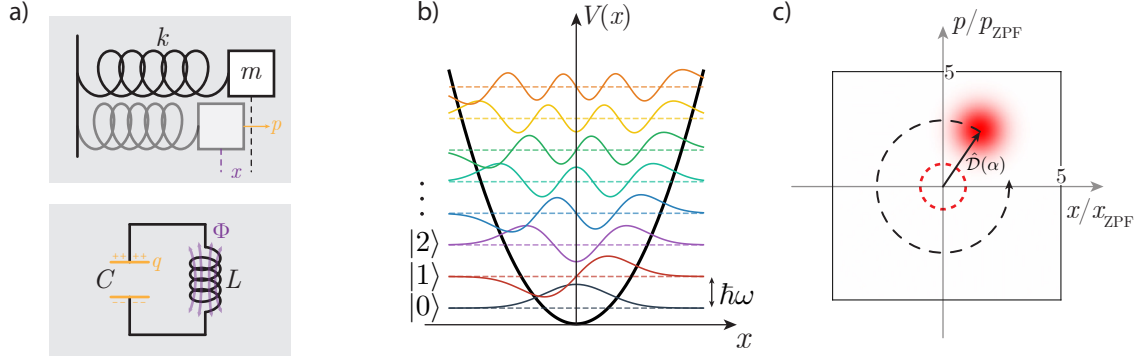
Figure 3.1 | **Overview of the quantum harmonic oscillator.** (a) Depiction of a mechanical oscillator (top) and lumped element LC oscillator (bottom). In the case of the LC oscillator, the charge on the capacitor and flux through the inductor serves the role of the position and momentum, respectively. (b) Eigenfunctions of the quantum harmonic oscillator, plotted against the classical potential energy. (c) Phase space representation of a coherent state, which can be obtained by performing a displacement operation $\hat{\mathcal{D}}(\alpha)$ on the vacuum state (dashed red circle). The coherent state will follow a classical circular trajectory in phase space at a rate ω (dashed black curve).

3.1.1   The quantum harmonic oscillator

The quantum harmonic oscillator, much like the classical harmonic oscillator, is one of the most ubiquitous models in physics. It is able to capture the behavior of a wide range of systems such as mechanical resonators, electromagnetic modes, and molecular rotations and vibrations. As with many models, the quantum harmonic oscillator may not always provide an exact description of real systems, but it serves as a useful starting point with analytical solutions.

The canonical 1D quantum harmonic oscillator has a Hamiltonian:

$$\hat{H}_{\text{QHO}} = \frac{\hat{p}^2}{2m} + \frac{1}{2}m\omega^2\hat{x}^2 \tag{3.1}$$

which describes a mass m confined to a quadratic potential (such as the one associated with a spring) in one dimension with a frequency ω. The same form of Hamiltonian can be used to describe a simple lumped-element model of an LC circuit:

$$\hat{H}_{\text{LC}} = \frac{\hat{Q}^2}{2C} + \frac{\hat{\Phi}^2}{2L} \tag{3.2}$$

where the charge $\hat{Q}$ on the capacitor with capacitance C can be thought of as a momentum and the flux $\hat{\Phi}$ through the inductor with inductance L can play the role of a position[1] (Fig. 3.1). The position and momentum operators obey the canonical commutation relation $[\hat{x}, \hat{p}] = i\hbar$ where $\hbar$ is the reduced Planck's constant. A more illuminating basis to work in are the creation and annihilation operators, defined as

$$\hat{a} = \sqrt{\frac{m\omega}{2\hbar}}\left(\hat{x} + \frac{i}{m\omega}\hat{p}\right) = \sqrt{\frac{1}{2\hbar Z_C}}\left(\hat{\Phi} + iZ_C\hat{Q}\right) \tag{3.3}$$

$$\hat{a}^\dagger = \sqrt{\frac{m\omega}{2\hbar}}\left(\hat{x} - \frac{i}{m\omega}\hat{p}\right) = \sqrt{\frac{1}{2\hbar Z_C}}\left(\hat{\Phi} - iZ_C\hat{Q}\right) \tag{3.4}$$

where $Z_C = \sqrt{\frac{L}{C}}$ is the characteristic impedance of the circuit, and the operators obey the commutation relation $[\hat{a}, \hat{a}^\dagger] = 1$. The Hamiltonian in this basis is simply:

$$\hat{H}_{\text{QHO}} = \hbar\omega\left(\hat{a}^\dagger\hat{a} + \frac{1}{2}\right) \tag{3.5}$$

We can define a number operator $\hat{n} = \hat{a}^\dagger\hat{a}$ and see that the energy eigenstates are the so-called Fock states $\{|n\rangle\}$ such that $\hat{n}|n\rangle = n|n\rangle$ where n is the number of excitations in the oscillator. In the position basis $\langle x|n\rangle$, these eigenstates are represented as Hermite functions $\psi_n(x)$. The ground state $|0\rangle$, otherwise known as the vacuum state, is a minimum uncertainty state in that it saturates the Heisenberg uncertainty principle.

Another class of states that are of interest are the coherent states. Formally defined as an eigenstate of the annihilation operator $\hat{a}|\alpha\rangle = \alpha|\alpha\rangle$, coherent states are labeled by an amplitude α which can take on any complex value. A useful representation of a coherent state is in the number basis:

$$|\alpha\rangle = e^{-\frac{|\alpha|^2}{2}} \sum_{n=0}^{\infty} \frac{\alpha^n}{\sqrt{n!}} |n\rangle \tag{3.6}$$

where the number probabilities follow a Poisson distribution. One can create a coherent

---

1. At this stage the identification of charge as momentum and flux as position is arbitrary — as we will see later, we choose this convention in anticipation of incorporating nonlinear inductances, which are much easier to analyze as a nonlinear potentials as opposed to non-quadratic momenta.

state in a quantum harmonic oscillator by performing a displacement operation

$$\hat{\mathcal{D}}(\alpha) = e^{\alpha \hat{a}^\dagger - \alpha^* \hat{a}} \tag{3.7}$$

on an initial vacuum state such that $\hat{\mathcal{D}}(\alpha) |0\rangle = |\alpha\rangle$. This can be understood from the fact that the position operator generates translations in momentum and vice-versa; here, the displacement axis is allowed to be along any direction in phase space. The ensuing trajectory, however, is completely classical; the expectation values of $\langle \hat{x} \rangle$ and $\langle \hat{p} \rangle$ follow the classical equations of motion for a harmonic oscillator.

3.1.2 Gaussian transformations

The displacement operation is perhaps the simplest operation one can perform on an oscillator state, amounting to a translation in phase space. In fact, the displacement operation belongs to a class known as *Gaussian* operations, which are defined as operations that transform Gaussian states into Gaussian states [Weedbrook et al. 2012]. We briefly discuss these states and operations in this section, as they will be an important foundation for the experiment performed in Chapter 4.

A Gaussian state is characterized by a $2N$-dimensional Wigner function that is Gaussian, where N is the number of modes. As such, the state is completely determined by its first and second statistical moments. If we define $\hat{\mathbf{z}} = (\hat{x}_1, \hat{p}_1, ..., \hat{x}_N, \hat{p}_N)^T$ with elements $\hat{z}_i$ where $i \in \{1, 2N\}$, then we can compactly write a mean vector and covariance matrix:

$$\bar{\mathbf{z}} = \mathrm{Tr}(\hat{\mathbf{z}}\hat{\rho}) \tag{3.8}$$

$$V_{ij} = \frac{1}{2}\mathrm{Tr}(\{\Delta\hat{z}_i, \Delta\hat{z}_j\}\hat{\rho}) \tag{3.9}$$

where $\{a, b\} = ab + ba$ is the anticommutator and $\Delta\hat{z}_i = \hat{z}_i - \langle \hat{z}_i \rangle$. We list a few examples:

- **Vacuum state** $|0\rangle$: $\bar{\mathbf{z}} = (0, 0), \hat{V} = \hat{\mathbf{1}}$

- **Coherent state** $|\alpha\rangle$: $\bar{\mathbf{z}} = (\mathrm{Re}(\alpha), \mathrm{Im}(\alpha)), \hat{V} = \hat{\mathbf{1}}$

- **Thermal state** $\hat{\rho}_{\mathrm{th}}(\bar{n})$: $\bar{\mathbf{z}} = (0, 0), \hat{V} = (2\bar{n} + 1)\hat{\mathbf{1}}$

For our definition, the Heisenberg uncertainty relation reads $V(\hat{x}_i)V(\hat{p}_i) \geq 1$, which is saturated by the vacuum and coherent states, but not for the thermal state with average occupation $\bar{n}$.

From the above characterization of Gaussian states, we now consider how Gaussian operators transform these states. In addition to the displacement operation, which translates the mean by some amount, the other two single-mode Gaussian operations are the rotation and squeezing operations:

$$\hat{R}_1(\theta) = e^{-i\theta\hat{a}^\dagger\hat{a}} \tag{3.10}$$

$$\hat{S}(\zeta) = e^{\frac{1}{2}(\zeta^*\hat{a}^2 - \zeta\hat{a}^{\dagger 2})} \tag{3.11}$$

The rotation operation is rather straightforward to understand: it simply rotates a state in phase space by an amount θ around the origin $\hat{a} \rightarrow \hat{a}e^{-i\theta}$. The squeezing operation is a bit more subtle, as it appears to create and annihilate excitations in pairs by an amount ζ. Qualitatively, it "squeezes" the phase space distribution of a state in a way that preserves the uncertainty bound along an axis defined by $\text{Arg}(\zeta/2)$ (Fig. 3.2). Another way to describe its action is by a Bogliubov transformation on the creation and annihilation operators:

$$\hat{a} \rightarrow \cosh(\zeta)\hat{a} - \sinh(\zeta)\hat{a}^\dagger \tag{3.12}$$

Though the operation looks quite simple, the applications and properties of squeezed states are vast and interesting [Walls 1983].

Finally, the singly most important two-mode Gaussian primitive is the two-mode rotation, also known as a beamsplitter:

$$\hat{R}_2(\theta) = e^{\theta(\hat{a}^\dagger\hat{b} - \hat{a}\hat{b}^\dagger)} \tag{3.13}$$

This operation linearly mixes the two modes $\hat{a}$ and $\hat{b}$ by an angle θ and amounts to the
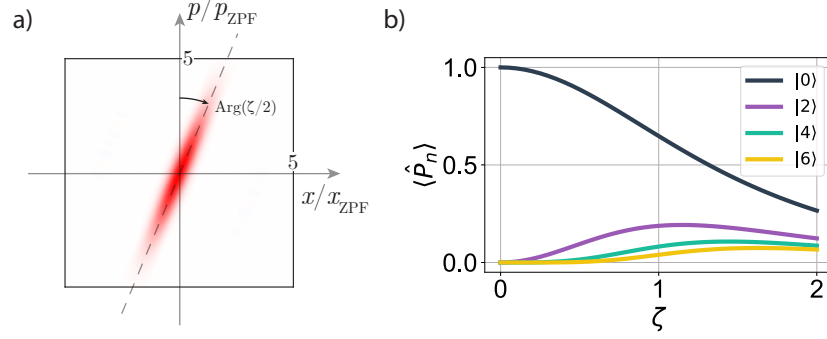
Figure 3.2 | Single-mode squeezing (a) Phase space distribution of a squeezed vacuum state $\hat{S}(\zeta)|0\rangle$ where $\zeta = e^{i\pi/4}$. (b) Excitation number populations as a function of ζ, cut off at $n = 6$. All odd excitation populations are identically zero, owing to the fact that the squeezing operation preserves parity.

following transformation of the mode operators:

$$
\begin{pmatrix} \tilde{a} \\ \tilde{b} \end{pmatrix} = \begin{pmatrix} \cos(\theta) & \sin(\theta) \\ -\sin(\theta) & \cos(\theta) \end{pmatrix} \begin{pmatrix} \hat{a} \\ \hat{b} \end{pmatrix}
\tag{3.14}
$$

In the context of electromagnetic modes, this operation results from a linear hybridization of two uncoupled modes and facilitates the exchange of energy between them in the uncoupled basis. For completeness, we note that the two-mode squeezing operator

$$
\hat{U}_{\text{TMS}}(\zeta) = e^{\frac{1}{2}(\zeta^* \hat{a}\hat{b} - \zeta \hat{a}^\dagger \hat{b}^\dagger)}
\tag{3.15}
$$

is the other two-mode Gaussian operation, though it can be constructed by concatenating two orthogonal single-mode squeezing operations with a 50:50 beamsplitter ($\theta = \pi/4$).

We notice that Gaussian operations are generated by terms either linear or bilinear in the creation and annihilation operators. Operations that are generated from terms that are higher order in $\{\hat{a}_i, \hat{a}_i^\dagger\}$ are called non-Gaussian. It has been shown that the addition of a single non-Gaussian operation can generate the action of a Hamiltonian of arbitrary order in $\{\hat{a}_i, \hat{a}_i^\dagger\}$ [Lloyd and Braunstein 1999], though such a construction relies on potentially costly (but polynomial!) compilation overhead. While the scope of Gaussian states and transformations is broad, we will see that our use of them in Chapter 4 is intuitively
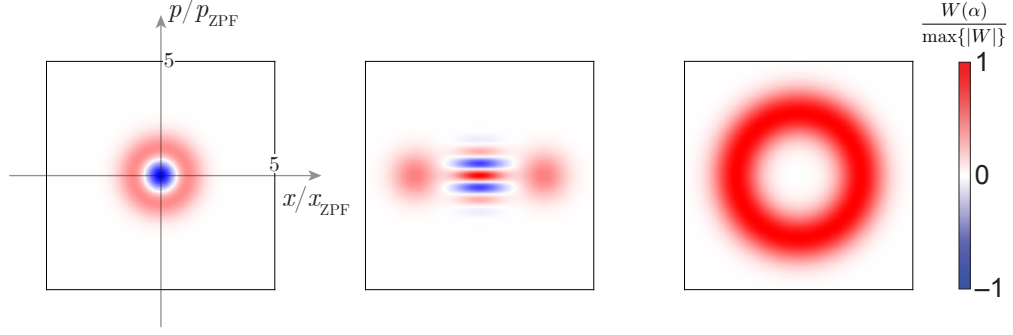
Figure 3.3 | **Wigner quasiprobability distributions.** Simulated Wigner functions for a Fock state $|n = 1\rangle$ (left), Schrödinger cat state $\frac{1}{\mathcal{N}}(|\alpha\rangle + |-\alpha\rangle)$ (middle) and mixed state (right). The mixed state represents a coherent state that has lost all phase coherence, i.e. $\hat{\rho} = \sum_n p_n |n\rangle \langle n|$ where $\{p_n\}$ are Poission distributed. Wigner functions are normalized to their extremal value for visualization purposes.

associated with physical transformations between molecular configurations.

3.1.3 State tomography & Wigner functions

Fock states and Gaussian states are perhaps the simplest states to understand for a quantum harmonic oscillator. However, we would like a general prescription for visualizing arbitrary states that has physical relevance with regards to our experimental measurements.

From an experimental perspective, performing tomography on a quantum system amounts to performing a number of repeated measurements on identically prepared states in order to reconstruct the elements of the density matrix $\hat{\rho}$. For a quantum system with d levels, the number of parameters needed to uniquely identify $\hat{\rho}$ is $d^2 - 1$ owing to the fact that the density matrix is Hermitian and constrained to have $\mathrm{Tr}(\hat{\rho}) = 1$. This translates to measuring expectation values of $d^2 - 1$ *linearly independent* operators to reconstruct the state. This poses a potential challenge for oscillator states that may span a large Hilbert space, particularly because it means one has to measure so many independent operators in a faithful and unbiased manner. Fortunately, the *Wigner function* offers a convenient solution if one is able to fulfill two requirements: measure the parity operator $\hat{\Pi} = e^{i\pi \hat{a}^\dagger \hat{a}}$ and perform displacements operations. One can see this by the following representation of the Wigner

function [Cahill and Glauber 1969]:

$$W_\rho(\alpha) = \frac{2}{\pi}\mathrm{Tr}\big(\hat{\rho}\hat{\mathcal{D}}(\alpha)\hat{\Pi}\hat{\mathcal{D}}^{-1}(\alpha)\big) \tag{3.16}$$

As such, one can obtain the Wigner function by measuring the expectation value of displaced parity for each point in phase space.

How should we physically interpret the Wigner function? By integrating the Wigner function along either position or momentum, one recovers a marginal distribution that acts as a probability distribution for the conjugate axis:

$$\int W_\rho(x' + ip)dx' = \langle p|\,\hat{\rho}\,|p\rangle \tag{3.17}$$

$$\int W_\rho(x + ip')dp' = \langle x|\,\hat{\rho}\,|x\rangle \tag{3.18}$$

which must be normalized. In this sense, the Wigner function can be used to obtain a probability distribution. The Wigner function itself, however, can take on negative values — this is indicative of a quantum mechanical state, and thus classifies the Wigner function as a quasiprobability distribution. Examples of Wigner functions for a few different states are given in Fig. 3.3.

By inverting the Wigner function, one can obtain the full density matrix, though care needs to be taken to ensure that enough measurements are performed to span enough of Hilbert space for an accurate reconstruction. In practice, maximum-likelihood estimation (MLE) techniques are used as opposed to direct inversion to avoid issues with numerically reconstructing unphysical density matrices. This technique was first implemented in the optical domain for measuring the Wigner function of classical [Banaszek et al. 1999] and non-classical [Bertet et al. 2002] states of light. Notably, the negativity in the Wigner function is a signature of a non-classical state. As we will see later, measuring Wigner functions is fairly straightforward in a circuit QED platform.

3.2 Circuit quantum electrodynamics

Today, one may hear that superconducting qubits are a "leading contender for building a quantum computer." The historical developments that make this statement true are rich with physics which should lead to a deep appreciation for how remarkable the technology is. While the full story is certainly beyond the scope of any single reference, we will attempt here to highlight notable developments that have brought us to the technology that we have today. Much of what follows originates from "Exploring the Quantum" [Raimond and Haroche 2006] and the large number of Ph.D. theses and review articles written by current and former members of the Yale team.

3.2.1 From Purcell to Cavity QED and the dispersive regime

Almost every realization of a physical qubit will rely on isolating and manipulating two distinct energy levels of a quantum system. These two energy levels may naturally represent the $|0\rangle$ and $|1\rangle$ states of the qubit, separated by some energy $E = \hbar\omega_{01}$. Perhaps even more common is for the $|0\rangle$ ($|1\rangle$) state to be a non-degenerate ground (excited) state. Assuming for the moment a cold environment $T = 0\,\mathrm{K}$, the first concern for controlling the qubit is the spontaneous emission of the excited state. Clearly, the rate of spontaneous emission needs to be much smaller than that of performing manipulations. On the other hand, it may be desirable to increase the rate of spontaneous emission for the purposes of performing measurements. As such, a method of controlling the spontaneous emission would be a very useful starting place.

Historically, the idea of controlling spontaneous emission dates back to Edward Purcell, who shared the 1952 Nobel Prize in Physics with Felix Bloch for developing nuclear magnetic resonance (NMR). The central problem that Purcell sought to address was the extremely long thermalization times of an ensemble of polarized nuclear spins in a solid material at room temperature. The experiment that Purcell and co-workers performed was to first place such a material (in their case paraffin) inside a resonant cavity, which was adjusted to have a frequency of roughly 30 MHz. A large static magnetic field first polarized the spins, followed by a weak RF tone applied perpendicular to the static field that slowly
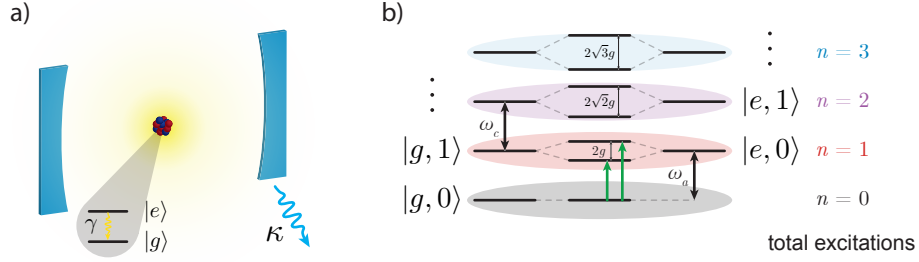
Figure 3.4 | Cavity quantum electrodynamics. (a) Depiction of cavity QED: a single atom is located inside a Fabry-Perot cavity with two energy levels (typically Rydberg levels) denoting $|g\rangle$ and $|e\rangle$ of a dipole-allowed transition with decay rate γ. The cavity has a decay rate κ. (b) Energy level diagram (not to scale) of the Jaynes-Cummings Hamiltonian for $\Delta = 0$. The eigenstates are hybridized in each subspace containing n total excitations. Vacuum Rabi splitting is observed when the system is probed from the vacuum state to the two $n = 1$ states (green arrows) when $g > \{\gamma, \kappa\}$.

energized the spins. By slowly tuning the static field and monitoring the output of the cavity, a distinct absorption was observed associated a value of the static field that matched the Larmor frequency of the spins with the frequeny of the cavity [Purcell, Torrey, and Pound 1946].

The interpretation here follows from a Fermi's golden rule argument regarding what determines the spontaneous emission rate. By placing the nuclear spins in a resonant cavity, the spontaneous emission rate is enhanced by a factor $\eta = 3Q\lambda^3/4\pi^2 V$ where Q, λ, and V are the cavity's quality factor, wavelength, and volume, respectively.

Even though Purcell's ideas are based on quantum mechanics, the experiments still involved a macroscopic ($\sim 10^{23}$) number of spins. Cavity quantum electrodynamics (CQED) further develops Purcell's ideas fully into the quantum realm, replacing nuclear spins with atoms and asking what happens at the level of individual atoms and single photons.

The canonical setup for a cavity QED system is as follows: a single atom is placed inside an electromagnetic cavity, typically at the location of the maximum field amplitude of a single cavity mode of interest (Fig. 3.4). The atom and cavity mode interact via a dipole interaction such that the Hamiltonian can be described by the Jaynes-Cummings

Hamiltonian:

$$\hat{H}_{\text{JC}}/\hbar = \omega_a \frac{\hat{\sigma}_z}{2} + \omega_c \hat{c}^\dagger \hat{c} + g\hat{\sigma}_x(\hat{c} + \hat{c}^\dagger) \tag{3.19}$$

$$\approx \omega_a \frac{\hat{\sigma}_z}{2} + \omega_c \hat{c}^\dagger \hat{c} + g(\hat{\sigma}^+ \hat{c} + \hat{\sigma}^- \hat{c}^\dagger) \tag{3.20}$$

where ω_a is an atomic transition frequency of interest, ω_c is the cavity frequency, and g is the interaction strength that is determined by the dot product of atom's transition dipole moment and the zero point electric field of the cavity. Note that we have performed the rotating wave approximation (RWA) and discarded non-excitation-conserving terms (see Appendix A). We assume that other frequencies of the system, i.e. other atomic transitions and higher order cavity modes, are sufficiently far away. Furthermore, we consider intrinsic relaxation rates $\{\gamma, \kappa\}$ of the selected atomic excited state and cavity field, respectively.

The Jaynes-Cummings model, though seemingly, simple, offers a wide range of qualitatively different regimes based on the interplay between the detuning between the atom and the cavity $\Delta = \omega_a - \omega_c$, the interaction strength g, and the relaxation rates γ and κ. We briefly describe a number of these regimes which have particular historical and technical relevance.

The first noteworthy set of experiments build on Purcell's pioneering work by enhancing [Goy et al. 1983] and even inhibiting [Hulet, Hilfer, and Kleppner 1985] spontaneous emission of Rydberg atoms passing through Fabry-Perot cavities. The interaction occurs while the Rydberg atoms occupy the cavity volume. Rydberg atoms are particularly well suited for cavity QED experiments owing to their huge ($\sim\mu$m) electric dipoles, which enable large coupling rates, and selective detection capabilities. From the perspective of the Jaynes-Cummings model, inhibiting spontaneous emission corresponds to a value of γ that is suppressed owing to the reduced density of states in the cavity volume. Intuitively, this occurs when the atomic transition is sufficiently detuned from the cavity modes.

Initial experiments operated in the regime where the relaxation rates, typically limited by the cavity rate κ, overwhelmed the interaction strength g leading to largely incoherent effects. A new regime, known as *strong coupling,* is unlocked when the interaction strength g is larger than both the atomic and cavity decay rates $\{\gamma, \kappa\}$. From a technological per-

spective, this was a difficult regime to access owing to large cavity decay rates. The break-through came by using superconducting Niobium microwave cavities [Meschede, Walther, and Müller 1985] and high-finesse optical cavities [Thompson, Rempe, and Kimble 1992].

The strong coupling regime can be understood by diagonalizing $\hat{H}_{\text{JC}}$ and expressing the resulting eigenstates in the original uncoupled basis. A nice feature that we can utilize is the fact that the interaction term preserves the total number of excitations in the system. This results in the full Hamiltonian being block-diagonal in the 2×2 constant excitation subspaces $\{|e, n - 1\rangle, |g, n\rangle\}$ for $n \geq 1$ being the total number of excitations. The ground state $|g, 0\rangle$ remains invariant under the interaction. The task is to then diagonalize each of these subspaces (setting $\hbar = 1$):

$$\hat{H}_{\text{JC}}^n = \begin{pmatrix} \omega_a + (n-1)\omega_c & g\sqrt{n} \\ g\sqrt{n} & n\omega_c \end{pmatrix} \tag{3.21}$$

resulting in eigenvalues $E_n^\pm = \frac{1}{2}\left((2n - 1)\omega_c + \omega_a \pm \sqrt{\Delta^2 + 4g^2 n} \right)$ and eigenvectors

$$\overline{|+, n\rangle} = \sin(\theta_n) |g, n\rangle + \cos(\theta_n) |e, n - 1\rangle \tag{3.22}$$

$$\overline{|-, n\rangle} = \cos(\theta_n) |g, n\rangle - \sin(\theta_n) |e, n - 1\rangle \tag{3.23}$$

where $\theta_n = \frac{1}{2}\arctan\left(\frac{2g\sqrt{n}}{\Delta}\right)$. We first qualitatively consider the resonant case where $\Delta = 0$. Here we see that the eigenstates become fully hybridized in each subspace and the single atomic excitation is shared equally between the atom and the cavity (Fig. 3.4). A distinct signature of this behavior is the so-called vacuum Rabi splitting, where the system can be probed spectroscopically to reveal two distinct peaks associated with the $\overline{|+, 1\rangle}$ and $\overline{|-, 1\rangle}$ hybridized states split by $2g$. The nomenclature refers to the fact that the hybridization emerges from the coupling of the atom to the zero point vacuum field of the cavity. Furthermore, the hybridization also balances the decay rates, giving each eigenstate an inherited decay rate of $(\gamma + \kappa)/2$. The first vacuum Rabi splitting was observed in an optical cavity QED setup [Thompson, Rempe, and Kimble 1992].

In contrast with the resonant regime, operating with $g \ll \Delta$ puts us in the so-called

dispersive regime. We can analyze this regime by performing a unitary transformation $\hat{U} = e^{\frac{g}{\Delta}(\hat{c}\hat{\sigma}^+ + \hat{c}^\dagger\hat{\sigma}^-)}$ and expanding to second order in $\frac{g}{\Delta}$:

$$\hat{H}_{\text{disp}}/\hbar = \left(\frac{\omega_a}{2} + \frac{g^2}{2\Delta}\right)\hat{\sigma}_z + \omega_c\hat{c}^\dagger\hat{c} + \frac{g^2}{2\Delta}\hat{\sigma}_z\hat{c}^\dagger\hat{c} \tag{3.24}$$

where we can define the dispersive shift $\chi = \frac{g^2}{\Delta}$ which can be interpreted as either a frequency shift χ of the cavity when the atom is excited or a frequency shift χ of the atom for each photon in the cavity. Furthermore, there is a Lamb shift $g^2/2\Delta$ of the atom's transition frequency originating from the zero point field of the cavity.

In the dispersive regime, the single-excitation hybridization $\sin(\theta_1) \approx \frac{g}{\Delta}$ is weak and thus we have defined atom-like and cavity-like modes in Eq. 3.24. The corresponding hybridization-induced decay rate of the atom is:

$$\gamma_\kappa = (\frac{g}{\Delta})^2\kappa \tag{3.25}$$

which is a good approximation in cavity QED where all of the other cavity modes can be taken to be far detuned.

The dispersive interaction is significant because the atom and the cavity now interact without directly exchanging energy. The primary implication of this is the ability to perform quantum non-demolition (QND) measurements of the atom in the $\hat{\sigma}_z$ basis via a measurement of the frequency of the cavity. Because $\hat{\sigma}_z$ eigenstates are eigenstates of the interaction Hamiltonian, successive measurements will return the same result after the first measurement collapses an arbitrary superposition state onto either $|g\rangle$ or $|e\rangle$. We return to this concept in more detail when describing modern circuit QED measurements in section 3.3.4. For a comprehensive treatment of quantum measurements, we refer the reader to [Clerk et al. 2010].

In cavity QED, operating in the strong dispersive regime led to many decisive breakthroughs, including the real-time tracking of quantum jumps for single photons [Gleyzes et al. 2007]. By the early 2000s, the stage had been set for taking the tale of cavity QED and applying it to superconducting circuits.
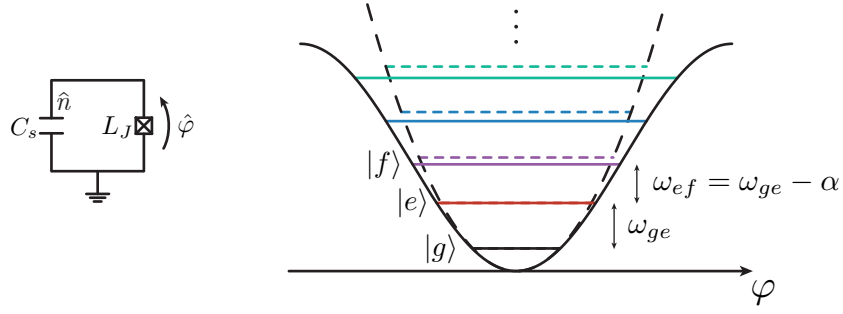
Figure 3.5 | Circuit depiction of a Josephson junction with kinetic inductance L_J shunted by a capacitance C_s. In the transmon regime $E_J/E_C \gg 1$, one can accurately describe the system as an anharmonic oscillator for low energy states.

3.2.2 Circuit QED with the transmon qubit

The development of superconducting qubits originated from a question regarding fundamental physics: can macroscopic degrees of freedom exhibit quantum phenomena? Remarkably, the answer is an affirmative yes, where the macroscopic degree of freedom is related to a single order parameter associated with two superconductors connected via a weak link now commonly known as a Josephson junction. Pioneering experiments in the 1980s by Michel Devoret, John Martinis, and John Clarke revealed for the first time that a Josephson junction possessed quantized energy levels [Martinis, Devoret, and Clarke 1985] and displayed macroscopic quantum tunneling [Devoret, Martinis, and Clarke 1985; Martinis, Devoret, and Clarke 1987] of Cooper pairs. For a modern synopsis on their experiments, we refer the reader to [Martinis, Devoret, and Clarke 2020].

The next challenge was to design and control a qubit using the Josephson junction. From a toolbox perspective, the other available circuit elements are simple capacitors and inductors. Fortunately, having these three elements and the freedom of engineering different energy scales and circuit topologies has enabled a extremely rich family of superconducting qubits which are still actively investigated, developed, and refined today [Wendin 2017; Kjaergaard et al. 2020].

In this section, we describe perhaps the simplest superconducting qubit which also turns out to be the one that has found the most widespread success in recent years: the transmon [Koch et al. 2007]. We consider a Josephson junction that is shunted by a capacitance

(Fig. 3.5). The corresponding Hamiltonian can be written in the charge basis $\{|n\rangle\}$, where n refers to the number of Cooper pairs on the superconducting island and can take any integer value:

$$\hat{H}_{\text{CPB}} = 4E_C(\hat{n} - n_g)^2 - \frac{E_J}{2}\sum_n(|n\rangle\langle n+1| + |n+1\rangle\langle n|) \tag{3.26}$$

The first term represents a capacitive energy (recall Eq. 3.2) where $E_C = e^2/2C_\Sigma$ is the single electron charging energy with a total capacitance $C_\Sigma = C_s + C_g$ to ground, where C_g is any additional capacitance to ground. The factor of 4 arises from considering Cooper pairs with charge $2e$ as our discrete unit, and n_g refers to an offset charge induced by local biasing electric field. The second term refers to the Josephson energy $E_J = \frac{\varphi_0^2}{2L_J}$ associated with Cooper pairs coherently tunneling across the barrier, where L_J is the kinetic inductance of the junction and φ_0 is the reduced flux quantum.

In the regime $E_C/E_J \geq 1$, this circuit is known as the Cooper-pair box, which is well described in the charge basis. It is worth noting that such a circuit was used to demonstrate the first coherent control of a superconducting qubit [Nakamura, Pashkin, and Tsai 1999] The transmon, however, operates in the opposite limit where $E_J/E_C \gg 1$. In this regime, the Josephson tunneling energy dominates and the charge basis is no longer an appropriate basis to treat the system. As such, we express the Josephson energy in the phase basis $\hat{\varphi}$, which is dual to the charge $\hat{n}$. By using the identity $|n\rangle = \frac{1}{2\pi}\int_0^{2\pi} d\varphi e^{-in\varphi}|\varphi\rangle$ [Devoret et al. 1995], we can write

$$\hat{H}_{\text{transmon}} = 4E_C(\hat{n} - n_g)^2 - E_J\cos(\hat{\varphi}) \tag{3.27}$$

where the phase φ is the superconducting phase drop across the junction and can be related to a generalized flux via $\varphi = \Phi/\phi_0$, where $\phi_0 = h/2e$ is the reduced magnetic flux quantum. We emphasize the subtlety that despite $\hat{n}$ and $\hat{\varphi}$ resembling the charge and flux operators of the quantum LC oscillator (Eq. 3.2), they differ in the fact that $n \in \mathbb{Z}$ and the phase φ is 2π periodic. These operators obey the dimensionless commutation relation $[\hat{\varphi}, \hat{n}] = i$, though strictly speaking only periodic functions of $\hat{\varphi}$ have meaning.

The prominent feature of the transmon is its exponential suppression to charge noise,

i.e. fluctuations in n_g, in the ratio E_J/E_C. In the transmon limit, we can to a good approximation ignore the periodic boundary conditions that lead to the sensitivity to charge noise and simply treat the phase variable as non-compact. Expanding the cosine potential to 4th order (and set $n_g = 0$ which corresponds to a specific choice of gauge in this picture):

$$\hat{H}_{\text{transmon}} = 4E_C\hat{n}^2 - E_J\left(1 - \frac{\hat{\varphi}^2}{2!} + \frac{\hat{\varphi}^4}{4!} - ...\right) \tag{3.28}$$

By neglecting a constant offset and recasting the charge and phase operators into dimensionless creation and annihilation operators via

$$\hat{n} = i\left(\frac{E_J}{8E_C}\right)^{\frac{1}{4}}\frac{(\hat{a} - \hat{a}^\dagger)}{\sqrt{2}} \tag{3.29}$$

$$\hat{\varphi} = \left(\frac{8E_C}{E_J}\right)^{\frac{1}{4}}\frac{(\hat{a} + \hat{a}^\dagger)}{\sqrt{2}} \tag{3.30}$$

we can recast Eq. (3.28) in a normal ordered form up to the 4th order Kerr nonlinearity, neglecting terms that do not conserve excitation number and rapidly rotate:

$$\hat{H}_{\text{transmon}}/\hbar \approx \omega_t\hat{a}_t^\dagger\hat{a}_t - \frac{\chi_{tt}^0}{2}\hat{a}_t^\dagger\hat{a}_t^\dagger\hat{a}_t\hat{a}_t \tag{3.31}$$

where $\omega_t = (\sqrt{8E_JE_C} - E_C)/\hbar$ is the frequency and $\chi_{tt}^0 \approx E_C/\hbar$ is the self-Kerr in the transmon limit, also known as the anharmonicity [Koch et al. 2007]. In practice, typical anharmonicities can be made to be up to $\sim$300 MHz, enabling single qubit gate speeds on the order of $\sim$10 ns.

Performing circuit QED with the transmon now amounts to coupling it to a microwave resonator. Intuitively, the physics ought to be similar to that of cavity QED: the nonlinear transmon (which acts as the atom) shares an electric dipole interaction with a linear microwave resonator (which acts as the cavity). The main difference is the form of the nonlinearity — in cavity QED, this came from the qubit nature of an atomic subspace, whereas for circuit QED the nonlinearity originates from the Josephson junction. For circuits, we follow a different approach based on the black-box quantization (BBQ) formalism [Nigg et al. 2012], and consider for simplicity a single Josephson junction and a single resonator
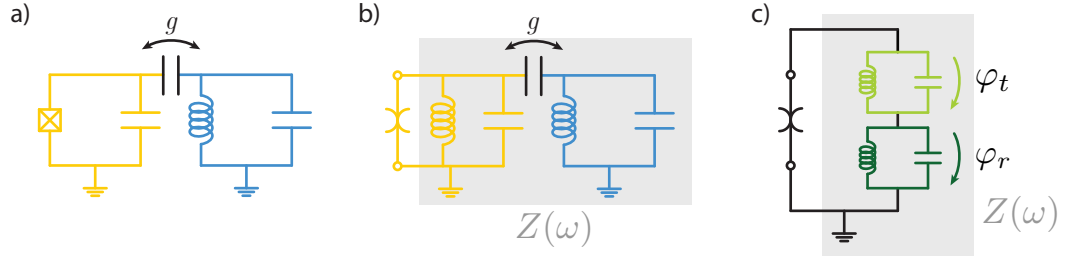
Figure 3.6 | Black-box circuit quantization. (a) Circuit diagram for a transmon artificial atom capacitively coupled to a single resonator mode with coupling strength g. (b) Splitting the Josephson junction into its linear (inductive) and nonlinear components, the circuit can be treated as an impedance $Z(\omega)$ as seen by the nonlinearity. (c) Diagonalizing the linear circuit, including the coupling, results in Foster's decomposition onto two eigenmodes with different voltage drops across the junction.

mode. For a more complete and detailed treatment, we refer the reader to [Blumoff 2017; Chou 2018] — we qualitatively highlight the main concepts here.

The central idea is that a passive one-port circuit can always be decomposed into Foster's first form [Foster 1924] consisting of parallel LCR oscillators (Fig. 3.6). Thus, one can consider the circuit network that the Josephson junction sees, i.e., the linear part of the circuit. Finding Foster's first form is equivalent to diagonalizing the linear circuit and determining a hybridized set of eigenmodes, which correspond to the poles of the impedance $Z(\omega)$. The influence of the Josephson junction may then be treated as a perturbation, since the lowest order nonlinearity originates from the 4th order term of the cosine expansion. This process results in transforming a capacitive coupling in the basis of "transmon" and "resonator" into decomposing the total flux across the Josephson junction into the contributions from the various eigenmodes:

$$\hat{\varphi} = \sum_i \hat{\varphi}_i = \sum_i \varphi_i(\hat{a}_i + \hat{a}_i^\dagger) \tag{3.32}$$

which will give rise to our couplings in the eigenbasis. The zero point phase fluctuations $\{\varphi_i\}$ can be determined either from the slope of the admittance $Y(\omega_i)$ or from the classical energy participation ratio of each mode's current contribution across the junction [Minev et al. 2021]. The resulting Hamiltonian for our simple example case by expanding up to 4th

order is:

$$\hat{H}_{tr}/\hbar = \omega_t \hat{a}_t^\dagger \hat{a}_t + \omega_r \hat{a}_r^\dagger \hat{a}_r - E_J \left(\cos(\hat{\varphi}) + \frac{\hat{\varphi}^2}{2} \right) \tag{3.33}$$

$$\approx \omega_t \hat{a}_t^\dagger \hat{a}_t + \omega_r \hat{a}_r^\dagger \hat{a}_r - \frac{E_J}{4!} \hat{\varphi}^4 \tag{3.34}$$

$$= \omega_t \hat{a}_t^\dagger \hat{a}_t + \omega_r \hat{a}_r^\dagger \hat{a}_r - \frac{E_J}{4!} \left(\sum_i \varphi_i (\hat{a}_i + \hat{a}_i^\dagger) \right)^4 \tag{3.35}$$

where identify the resonator as a readout mode and have removed the linear part from the cosine potential as they are absorbed into the mode frequencies. We reiterate that in this basis, the transmon mode $\hat{a}_t$ and readout mode $\hat{a}_r$ are the hybridized eigenmodes of the linear system. By expanding further and applying the rotating wave approximation, we arrive at a Hamiltonian with a dispersive coupling to a readout resonator:

$$\hat{H}_{tr}/\hbar \approx \omega_t \hat{a}_t^\dagger \hat{a}_t - \frac{\chi_{tt}}{2} \hat{a}_t^\dagger \hat{a}_t^\dagger \hat{a}_t \hat{a}_t + \omega_r \hat{a}_r^\dagger \hat{a}_r - \frac{\chi_{rr}}{2} \hat{a}_r^\dagger \hat{a}_r^\dagger \hat{a}_r \hat{a}_r - \chi_{tr} \hat{a}_t^\dagger \hat{a}_t \hat{a}_r^\dagger \hat{a}_r \tag{3.36}$$

with self-Kerr terms $\chi_{tt} = \frac{E_J}{2} \varphi_q^4$ and $\chi_{rr} = \frac{E_J}{2} \varphi_r^4$ of the transmon and readout resonator, respectively, and a cross-Kerr $\chi_{tr} = E_J \varphi_q^2 \varphi_r^2$, also known as the dispersive shift. We note that the transmon self-Kerr χ_{tt} is now slightly diluted compared to its standalone value χ_{tt}^0, which can be interpreted as the nonlinearity being distributed across every eigenmode in the system according to the energy participation ratios. We now have a Hamiltonian that strongly resembles Eq. (3.24). As we alluded to before, this Hamiltonian enables measurement of the state of the transmon by sending in a signal to probe the frequency of the readout resonator, which in turn depends on the qubit state. Such a technique, called dispersive readout (section 3.3.2.1), is ubiquitous for superconducting circuits and can be abstracted away as performing a measurement in the $\hat{\sigma}_z$ basis of the lowest two energy levels $\{|g\rangle, |e\rangle\}$ of the transmon.

In circuit QED, the treatment of the inherited decay rate of the transmon is a bit more complex compared to the cavity QED case. More often than not, the simple single-mode approximation (Eq. 3.25) fails. The primary difference comes from having a more complicated distributed electromagnetic environment, requiring a full circuit level treatment to properly predict the loss [Houck et al. 2008; Blumoff 2017]. This also motivates introduc-

ing *Purcell filters* to modify the impedance of the circuit as seen by the transmon, further suppressing the spontaneous emission [Reed et al. 2010].

This way of analyzing our circuits points to a (perhaps philosophical) difference between cavity QED and circuit QED. In cavity QED, there is a well-defined notion of a single atom and a single cavity before considering their interaction. Here, we see that in fact the hybridization and nonlinearity are treated separately. That is, diagonalizing the linear part of the circuit does take into account the hybridization of the modes, but does not yet factor in the nonlinearity. Hence, the concept of an isolated artificial atom and resonator mode is less meaningful given that it is the full electromagnetic environment that defines their existence.

3.2.3 Incorporating high-Q harmonic oscillators

The circuit QED architecture with transmon qubits was initially very successful and led to demonstrations of two-qubit algorithms [DiCarlo et al. 2009] and a simple three-qubit error correcting code [Reed et al. 2012]. In these experiments, however, the quality of the results were largely limited by the relaxation T_1 and decoherence T_2 times of the transmon qubits, which were consistently around 1 μs. It was clear that improving the coherence times would be a top priority for enabling the next generation of experiments.

The topic of decoherence in superconducting circuits is quite complex. Unlike atomic systems, superconducting circuits are macroscopic objects that are subject to the whims of materials science. There are many interfaces, all of which may be disordered at the microscopic scale, which may act as sources of loss for various qubit excitations. Furthermore, quasiparticles, which are single electron unpaired Cooper pairs that live above the superconducting gap, may tunnel across the junction and cause decoherence [Glazman and Catelani 2021]. Thus, the exact fabrication process and electromagnetic environment are critical components for determining qubit coherence.

Fortunately, there is a relatively simple formalism for breaking down the various sources of loss in a solid-state system known as *participation ratios*. The idea is that the total quality factor $Q = \omega T_1$ of an electromagnetic mode can be broken down as a sum of individual

lossy elements:

$$\frac{1}{Q} = \sum_i \frac{p_i}{q_i} \tag{3.37}$$

where $\{p_i\}$ are the participation ratios and $\{q_i\}$ are the intrinsic quality factors of the lossy elements. The participation ratio, as the name suggests, is defined as

$$p_i = \frac{\text{energy stored in element } i}{\text{total energy}} \tag{3.38}$$

for a given mode of interest. Under this formalism, we see two distinct avenues to increasing the quality factor: reduce the participation in lossy elements via geometric designs or improve the quality of the underlying materials. Addressing the latter is a challenging but necessary materials science endeavor which has only very recently begun to push the boundaries of transmon coherence [Place et al. 2021; Wang et al. 2022]. Around a decade ago, though, focusing on the former led to a new paradigm for superconducting circuits: going into the third dimension.

Of course, electromagnetic modes always live in three dimensions, but are relatively confined in a 2D planar architecture. The motivation behind going fully into 3D is simple: vacuum is the best dielectric since there is no loss, so we should focus on storing as much of the energy of the qubit as possible in vacuum. While this sounds promising, the concern is that one may sacrifice coupling strengths to resonators if the fields become too diluted. It turns out that this can be overcome simply by extending the size of the antenna pads for the transmon, which correspondingly increases the dipole moment. As such, the next leap in coherence times for transmon qubits came in a 3D architecture involving a rectangular cavity resonator, resulting in relaxation and decoherence times up to $\sim$60 and $\sim$20 μs, respectively [Paik et al. 2011].

This architectural shift spurred further innovations that unlocked a new paradigm for quantum information processing with circuit QED in the past decade. Centered on the belief that 3D cavity resonators (for which individual modes can be modeled as harmonic oscillators, see section 3.1.1) should in principle be able to have extremely high quality factors, the question arises: can circuit QED facilitate storing and processing quantum information

in a harmonic oscillator? Continuous-variable quantum computing had certainly been pro-
posed [Lloyd and Braunstein 1999], but experimental demonstrations had been elusive.
Of course, one still needs a nonlinear element in order to create and manipulate quantum
states of harmonic oscillator [Reinhold 2019], so we cannot abandon the transmon (or any
Josephson-junction based circuit element) completely.

Fortunately, incorporating an additional cavity mode to store and process quantum in-
formation (which we will now refer to as a storage cavity) to a circuit QED setup with a
single transmon and readout is fairly straightforward, and in fact can be done rather flexibly
in a 3D architecture. The storage cavity will want to remain as isolated from the environ-
ment as possible, but still be in the strong dispersive regime with respect to the transmon in
order to have sufficient control. Thus, the task is to engineer strong coupling between the
transmon and storage cavity while minimizing the coupling between the storage cavity and
the readout, which necessitates spatial and spectral separation of the cavity and readout
modes. If all the modes are coupled dispersively, the Hamiltonian can be written as:

$$\hat{H}_{ctr}/\hbar \approx \omega_c \hat{a}_c^\dagger \hat{a}_c + \omega_t \hat{a}_t^\dagger \hat{a}_t - \frac{\chi_{tt}}{2} \hat{a}_t^\dagger \hat{a}_t^\dagger \hat{a}_t \hat{a}_t + \omega_r \hat{a}_r^\dagger \hat{a}_r$$
$$- \chi_{ct} \hat{a}_c^\dagger \hat{a}_c \hat{a}_t^\dagger \hat{a}_t - \chi_{tr} \hat{a}_t^\dagger \hat{a}_t \hat{a}_r^\dagger \hat{a}_r - \chi_{cr} \hat{a}_c^\dagger \hat{a}_c \hat{a}_r^\dagger \hat{a}_r \qquad (3.39)$$
$$- \frac{\chi_{cc}}{2} \hat{a}_c^\dagger \hat{a}_c^\dagger \hat{a}_c \hat{a}_c - \frac{\chi_{rr}}{2} \hat{a}_r^\dagger \hat{a}_r^\dagger \hat{a}_r \hat{a}_r$$

Similar to the decay that an isolated atom inherits from a lossy cavity in the dispersive
regime of cavity QED (Eq. 3.25), the otherwise isolated cavity mode inherits an "inverse
Purcell" decay from a dispersive coupling to a lossy transmon [Reagor et al. 2016]:

$$\kappa_\gamma \approx (\frac{g}{\Delta})^2 \gamma \qquad (3.40)$$

where g and Δ now refer to the coupling strength and detuning between the transmon and
cavity modes, respectively. As previously discussed for the transmon case, a more rigorous
treatment carefully considers the distributed electromagnetic field profile of each mode in
relation to sources of loss. Nevertheless, a standard operating regime to balance interaction
strengths with hybridization-induced decay and high-fidelity readout of the entire system
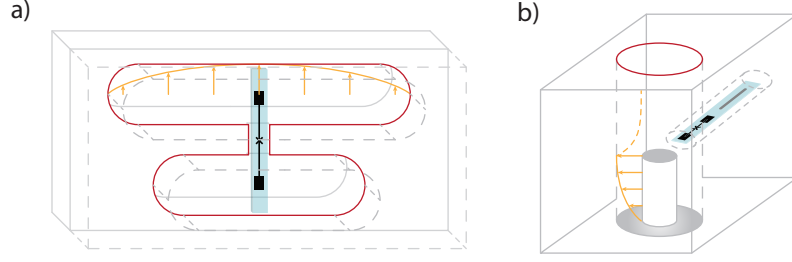
Figure 3.7 | 3D circuit QED module designs. (a) First generation architecture using rectangular cavities as storage (top) and readout (bottom) cavities. (b) Second generation architecture using a $\lambda/4$ coaxial cavity resonator as the storage with a planar stripline readout resonator. Red lines indicate seam location, yellow field lines depict fundamental storage cavity mode. The field directly above the cylindrical post is exponentially attenuated if the frequency is below the cutoff of the waveguide. Coupling ports are not shown, which are typically overcoupled to the readout resonator and undercoupled to the storage cavity and transmon modes.

is to have cross-Kerr strengths between the cavity/transmon $\chi_{ct}/2\pi$ and transmon/readout $\chi_{tr}/2\pi$ around $\sim 1\,\mathrm{MHz}$. Furthermore, the 6th order term $\chi'_{ct}\hat{a}^{\dagger}_c\hat{a}^{\dagger}_c\hat{a}_c\hat{a}_c\hat{a}^{\dagger}_t\hat{a}_t$ can be relevant when addressing larger photon numbers, though accurately predicting the strength (and even the sign) of such higher order nonlinear terms requires a more careful circuit analysis [Frattini et al. 2018].

Early experiments began to test the waters by using rectangular cavity resonators (Fig. 3.7) to encode quantum information in Schrödinger cat states [Vlastakis et al. 2013], tracking single photon jumps (much like in cavity QED!) [Sun et al. 2014], and manipulating quantum oscillator states [Heeres et al. 2015]. Simultaneously, theoretical developments of an error correcting code for a single harmonic oscillator mode [Leghtas et al. 2013; Mirrahimi et al. 2014] culminated in the first experiment to demonstrate quantum error correction at the break-even level [Ofek et al. 2016]. While these experiments certainly demonstrate the promise of bosonic quantum computation and error correction, the cavity resonator lifetimes were still only on the order of $\sim 100\,\mu\mathrm{s}$, in part due to losses at the seam of merging two halves to create the cavity.

This brings us to the modern era, where the design of a seamless coaxial cavity resonator brought single photon lifetimes to $\sim 1\,\mathrm{ms}$ while maintaining strong coupling to a transmon qubit in a circuit QED architecture [Reagor et al. 2016; Axline et al. 2016]. This design
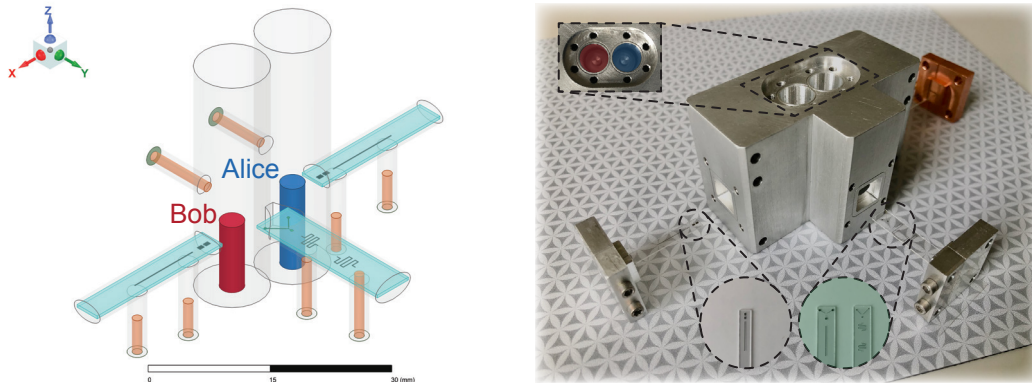
Figure 3.8 │ **A 3D double cavity circuit QED system.** ANSYS HFSS schematic (left) and photo (right) of the cQED device used in this thesis. Two coaxial cavity resonators Alice (blue) and Bob (red) are coupled via a Y-mon (green). The device is modular in that different Y-mon designs may be used for operating the simulator in different regimes (green inset); lower anharmonicity via a larger capacitance to ground for mixing purposes (left, used in Chapter 4) and larger anharmonicity to operate more in the qubit regime (right, used in Chapter 5).

has been amenable to various connectivities between cavities and qubits, and has served as the hardware for performing a large number of experiments, including the ones in this thesis. Looking ahead, it will be interesting to see the emergence of new creative 3D cavity designs with even greater performance. One particularly promising approach are seamless multimode cavities [Chakram et al. 2020; Chakram et al. 2021], which double down on the concept of hardware efficiency and are readily applicable towards quantum random access memories [Naik et al. 2017] and many-body physics. Finally, it is important to keep in mind that subsequent materials developments may very well motivate one to revisit the designs of a previous generation under a new light. For instance, the development and optimization of micromachined cavities [Lei et al. 2020] has revealed that seam loss should in fact not be a limiting factor for state-of-the-art devices.

3.3 A programmable bosonic quantum simulator

In this section, we present details on the hardware used for the experiments in this thesis. Both experiments consider emulating two nuclear degrees of freedom, so we utilize a device

containing two coaxial cavity resonators. Such a device was first designed and operated to demonstrate creating a two-mode Schrödinger cat state [Wang et al. 2016], and has since been further expanded and employed for performing operations between multiphoton states in each resonator [Rosenblum et al. 2018; Gao et al. 2018; Gao et al. 2019]. Design credit for the current version goes to Yvonne Gao and Brian Lester.

A schematic of the device is shown in Fig. 3.8. To a large extent, the design of devices involving coaxial cavity resonators can be quite modular [Axline et al. 2016]. Specifically, each cavity can couple to its own control module consisting of a transmon and a read-out resonator (and a potential additional Purcell filter) patterned on a dielectric substrate. Additionally, a coupling module using a transmon with a Y-shaped antenna (colloquially referred to as a "Y-mon") can be used to couple to both cavities and mediate interactions between them in various ways, as we discuss further in section 3.3.3. We will be interested in operating in the strong dispersive regime between all neighboring modes, necessitating a deliberate separation of frequencies.

3.3.1 Experimental design & controls

While there are many approaches to experimental design, we find that a useful starting exercise is to list a hierarchy of energy scales that needs to be satisfied for a given experiment. This helps constrain an otherwise broad engineering landscape and can help inform important design choices along the way. Qualitatively speaking, the landscape will be bounded on either end by an intrinsic decoherence scale Γ and a maximum allowable interaction strength $g_{\text{int}}^{\max}$ such that $\Gamma < E_{\text{other}} < g_{\text{int}}^{\max}$. Of course, the full set of energy scales need not fall on a linear relationship as suggested above. The next consideration is the method of engineering the set of desired interactions. As we will see in section 3.3.3, our choice of activating various Hamiltonian terms via parametric driving will enforce additional constraints and design considerations. We describe these high-level design criteria for each experiment in sections 4.2 and 5.2.

Designing a circuit QED device consists of two primary steps: 1) a geometric design that defines a set of linear electromagnetic modes and 2) a circuit quantization procedure that
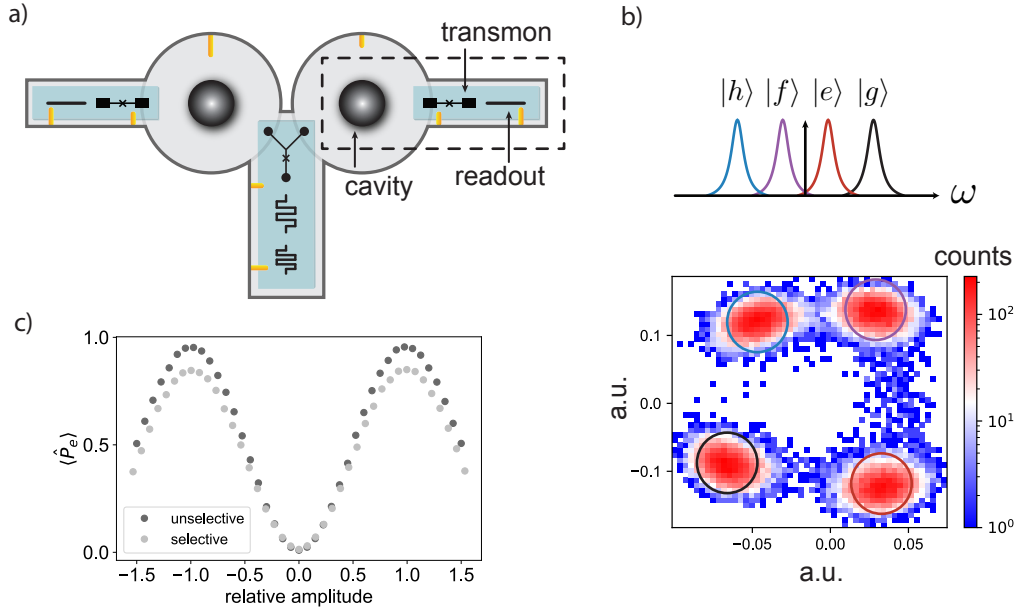
Figure 3.9 | **Single qubit calibrations.** (a) We consider a minimal "module" consisting of a single cavity, transmon, and readout resonator. (b) Dispersive measurement of the transmon states, where the spectrum of the readout resonator depends on the state of the transmon. In this case, the readout is able to distinguish between the first four transmon levels $\{|g\rangle, |e\rangle, |f\rangle, |h\rangle\}$ by driving the resonator between ω_r^e and ω_r^f. (c) Calibrating a selective and unselective π pulse between the transmon's two lowest eigenstates $\{|g\rangle, |e\rangle\}$. The selective pulse suffers more from decoherence, thus resulting in a lower contrast.

translates a set of modes to a target Hamiltonian after incorporating Josephson nonlinearities. The former utilizes a finite-element simulation tool, Ansys HFSS, for solving Maxwell's equations subject to the appropriate boundary conditions imposed on the system. From those results, one can apply either black-box quantization (BBQ) formalism [Nigg et al. 2012] or the energy-participation ratio (EPR) approach [Minev et al. 2021] to obtain an effective low energy Hamiltonian for the modes of interest. We refer the reader to [Gao 2018] for a comprehensive overview of the design process.

3.3.2 Basic capabilities & system characterization

In this section, we describe the basic functionalities of our system. Standard system characterization and calibration amounts to identifying the resonance frequencies of the modes, calibrating a set of pulses, and measuring self-Kerr and cross-Kerr terms as well as decoherence rates. Though this process is somewhat of an art, it can certainly be approached

systematically and is very well documented in [Chou 2018].

3.3.2.1 Dispersive readout

Performing readout using the dispersive shift of a resonator frequency based on the transmon state is ubiquitous in circuit QED. The basic idea is to send a probe tone to the readout resonator, which will have a different amplitude and phase response depending on the detuning of the probe tone from the resonant frequencies associated with the various transmon states (Fig. 3.9). By recording, digitizing, and integrating the signal against a reference signal, one acquires a single complex number. Averaging many trajectories together generates a histogram, which can be used to set a threshold for identifying what the qubit state was at the beginning of the measurement.

3.3.2.2 Resonant pulses

Here, we highlight the different types of resonant pulses that are commonly used in our system. We first consider a pulse with a Gaussian envelope that has a standard deviation in time σ_t. The frequency domain spectrum of such a pulse is also Gaussian with a standard deviation in frequency $\sigma_f = 1/2\pi\sigma_t$. When it comes to manipulating the transmon, a pulse that has a center frequency near ω_q that satisfies $\sigma_f \gg \chi$ is called *unselective* as it rotates the qubit between its eigenstates in a manner that is largely independent on the photon number distribution in the cavity. The unselective pulse must also have a bandwidth that is smaller than the self-Kerr $\sigma_f < \chi_{tt}$ in order to avoid exciting to higher transmon energy levels. In the opposite limit, a pulse centered on $\omega_q - n\chi + (n^2 - n)\chi'$ with $\sigma_f \ll \chi$ is called *selective* as it will only rotate the transmon if the cavity has identically n photons. It is of interest to calibrate the aforementioned pulses to perform a π rotation[2] around the Bloch sphere, such that the action is to exchange the two qubit states $|g\rangle \leftrightarrow |e\rangle$. Since selective π-pulses are longer than unselective π-pulses, they suffer more from decoherence.

Selective pulses enable the measurement of the cross-Kerr χ and 6th order nonlinear term χ' as well as calibration of displacement operations 3.10. Similar to the transmon

---

2. For a transmon, the presence of the Kerr nonlinearity and the second excited state $|f\rangle$ requires a detuning Δ away from ω_q and derivative pulse to efficiently enact a π-pulse [Motzoi et al. 2009].
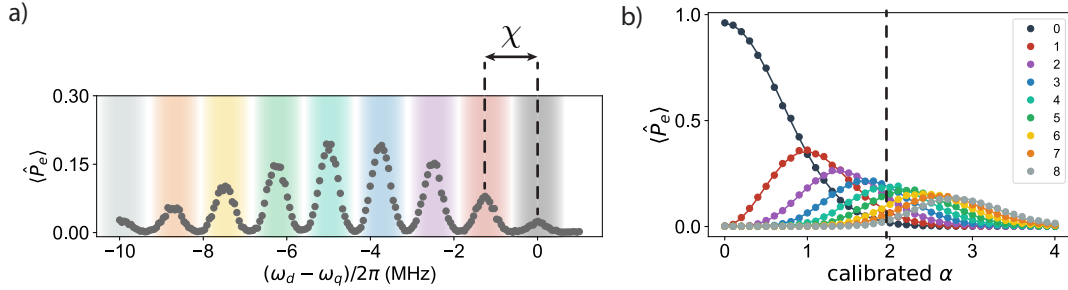
Figure 3.10 | **Single cavity calibrations.** (a) By displacing the cavity to a coherent state $|\alpha\rangle$ with a large spread in photon numbers, spectroscopy on the transmon using selective π-pulses can reveal number splitting [Schuster et al. 2007]. (b) By scanning the amplitude of a displacement pulse on the cavity and measuring photon number probabilities of the cavity (via sitting on the peaks in (a)), one can calibrate a unit displacement $\alpha = 1$. Dashed line indicates the approximate displacement used in (a).

pulses, cavity displacements can also be made either selective or unselective, now with respect to the transmon states following the same arguments. A calibrated displacement operation is thus the first Gaussian operation in our toolbox, and is also used for performing Wigner tomography as described in section 3.1.3.

3.3.2.3 Optimal control pulses

Going beyond the simple resonant pulses of the previous section, one can ask: what operations can be performed in general on the cavity mode in the dispersive regime? Initial work formulated [Krastanov et al. 2015] and demonstrated [Heeres et al. 2015] that concatenating different number selective π-pulses on the transmon with unselective cavity displacements was enough to generate arbitrary operations on a cavity state. Such a construction, however, is not optimal in the sequence depth as the maximum photon number increases, though it does have a nice property that lends itself to a fault-tolerant implementation [Reinhold et al. 2020]. Alternatively, the transmon and cavity can be driven simultaneously via numerically optimized pulses to enact arbitrary operations on the system's joint Hilbert space [Heeres et al. 2017]. Crucial to this technique is precise knowledge of a system's Hamiltonian as well as a method to efficiently compute the gradient of a target cost function, both of which can be satisfied for this problem. The benefit of using these numerically optimized pulses is that operations can typically be implemented in a dura-

tion $\tau_{\text{pulse}} \sim (1/\chi)$, which is beneficial for beating decoherence compared to the previous scheme. We note the further possibility of beating this empirical speed limit by using large displacements as described in [Eickbusch et al. 2021].

3.3.3 Parametric processes in circuit QED

In the previous section, we saw how near resonant drives can implement simple, yet distinct, operations on our system. From the point of view of the interaction Hamiltonian Eq. (3.39), the Kerr nonlinearities χ_{cq} and χ_{tt} set different energy scales to which the drive strength ϵ should be compared. In fact, all operations activated by driving the system in any way must utilize the Kerr nonlinearity. In this section, we consider two qualitatively different regimes of this that enables a wider range of operations: four-wave mixing via off-resonant drives (section 3.3.3.1) and interactions via a strongly driven Rabi qubit (section 3.3.3.2).

3.3.3.1 Enacting bosonic operations via four-wave mixing

In this section, we highlight a general technique that has been used extensively in bosonic circuit QED platforms to engineer a wide range of interactions. At its essence is invoking the mixing capabilties of the Josephson nonlinearity by driving the system off-resonantly in ways that satisfies new resonance conditions. Its power comes from the ability to turn interactions on and off quickly *in-situ* via microwave drives and the flexibility afforded by choosing various drive frequencies and strengths. Perhaps the most widely used application of this method in the context of quantum state transfer [Pfaff et al. 2017; Axline et al. 2018; Burkhart et al. 2021; Zhou et al. 2021] and multi-qubit operations [Gao et al. 2018; Gao et al. 2019] between bosonic qubits is the beamsplitter operation as introduced in section 3.1.2. As such, both the mathematical details of this process and practical implementation considerations have been extensively described in a number of recent theses [Gao 2018; Axline 2018; Burkhart 2020]. This technique is not restricted to the beamsplitter, and can be applied to enact any interaction Hamiltonian involving a number of creation and annihilation operators that is at least one less than the order of nonlinearity used to invoke

Interaction term $\hat{H}_{\text{int}}$	Resonance Condition	Operation
$g\hat{a}^\dagger\hat{b} + g^*\hat{a}\hat{b}^\dagger$	$\omega_b - \omega_a = \omega_2 - \omega_1$	Beamsplitter
$g\hat{a}^2 + g^*\hat{a}^{\dagger 2}$	$2\omega_a = \omega_1 + \omega_2$	Single-mode squeezing
$g\hat{a}\hat{b} + g^*\hat{a}^\dagger\hat{b}^\dagger$	$\omega_a + \omega_b = \omega_1 + \omega_2$	Two-mode squeezing

Table 3.1 | List of four-wave mixing Gaussian operations. Note that enacting all of these operations also require that $\omega_{1/2} \neq \omega_{a/b}$ to avoid the interaction being dominated by a displacement. The operations will also be qualitatively different if one or both of the modes has a decay rate that is comparable or larger than the interaction strength.

them. In the case of using the 4th order Kerr nonlinearity, this translates to a family of interactions that are bilinear or trilinear in the creation and annihilation operators. This generality and additional examples are well documented in [Reinhold 2019]. We also note that this technique extends powerfully when the 3rd order nonlinearity can be activated as well [Frattini 2021].

To qualitatively summarize how these four-wave mixing operations are enacted, we consider a general static circuit QED Hamiltonian Eq. (3.35) and add microwave drives:

$$\hat{H} = \sum_i \hbar\omega_i \hat{a}_i^\dagger \hat{a}_i - \frac{E_J}{4!}\left(\sum_i \varphi_i(\hat{a}_i + \hat{a}_i^\dagger)\right)^4 + \sum_j \sum_i 2\hbar\epsilon_{ji}\cos(\omega_{ji}t + \theta_{ji})(\hat{a}_i + \hat{a}_i^\dagger) \quad (3.41)$$

where we can in principle have more than one drive $\{j\}$ on each mode $\{i\}$. The goal here is to choose $\{\omega_{ji}\}$ such that in the frame of the drives, we are left with a desired effective static interaction Hamiltonian. Intuitively, a series of resonance conditions will need to be satisfied via expansion of the nonlinearity, while a large number of terms will be rotating and may be dropped under the RWA. We tabulate the three bilinear Gaussian operations and list the resonance conditions in Table (3.1). We expand on single-mode squeezing and the beamsplitter further in section 4.3.2 and provide a detailed derivation for single-mode squeezing in Appendix B.

3.3.3.2 Interactions between an oscillator and a Rabi qubit

The four-wave mixing operations of the previous section involve direct hybridization of the system's undriven eigenstates under the 4th order nonlinearity, mediated by external drives, in order to make a target process resonant. There exists another class of operations
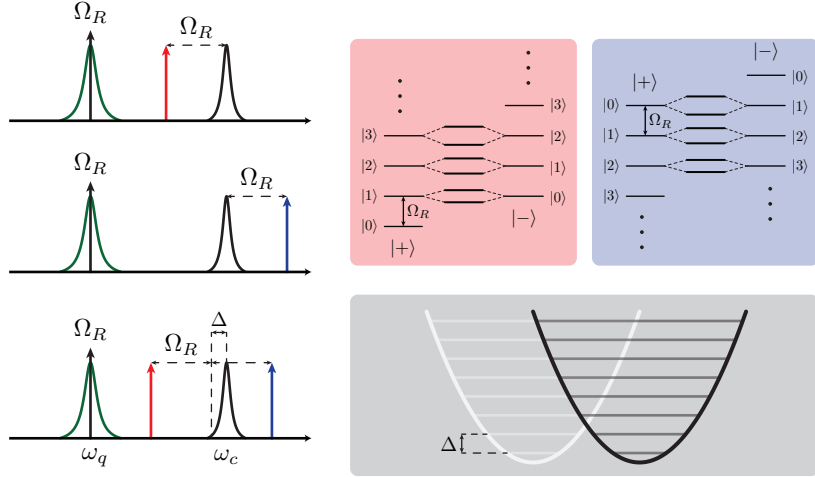
Figure 3.11 | **Sideband interactions between a Rabi qubit and cavity.** Driving a qubit on resonance with strength Ω_R defines the Rabi qubit Hamiltonian $\hat{H}_R/\hbar = -\frac{\Omega_R}{2}\hat{\sigma}_x$. Applying sideband drives on the cavity at frequencies $\omega_c \mp \Omega_R$ results in $\hat{H}_{\text{sb}}/\hbar = \pm\Omega_R\hat{c}^\dagger\hat{c}$ in the frame of the drives. Under the cross-Kerr interaction, this gives rise to resonances that couple $|+, n+1\rangle \leftrightarrow |-, n\rangle$ (red sideband) or $|+, n\rangle \leftrightarrow |-, n+1\rangle$ (blue sideband). Enacting these interactions simultaneously leads to a conditional displacement interaction, where the effective cavity energy can be tuned via detuning the average of the sideband frequencies from the cavity resonance.

that drives the cross-Kerr interaction between a qubit and an oscillator in a qualitatively different manner by leveraging a strong Rabi drive on the qubit. We describe this technique in generality and highlight the various applications it has found in quantum control and measurement in circuit QED, including for the experiment in Chapter 5.

We begin with the idealized Hamiltonian of a qubit coupled to a cavity under a dispersive interaction (Eq. 3.24) in the presence of a resonant drive on the qubit:

$$\hat{H}/\hbar = \frac{\omega_q}{2}\hat{\sigma}_z + \omega_c\hat{c}^\dagger\hat{c} + \frac{\chi}{2}\hat{\sigma}_z\hat{c}^\dagger\hat{c} + 2\Omega_R\cos(\omega_q t)\hat{\sigma}_x \tag{3.42}$$

By going into the rotating frame of the qubit and cavity $\hat{U} = e^{i(\frac{\omega_q}{2}\hat{\sigma}_z + \omega_c\hat{c}^\dagger\hat{c})t}$, we are left with:

$$\hat{H}/\hbar = -\frac{\Omega_R}{2}\hat{\sigma}_x + \frac{\chi}{2}\hat{\sigma}_z\hat{c}^\dagger\hat{c} \tag{3.43}$$

We can then go into the Rabi frame via $\hat{U} = e^{-i\frac{\Omega_R}{2}\hat{\sigma}_x t}$:

$$\hat{H}/\hbar = \frac{\chi}{2}\hat{c}^\dagger\hat{c}(\hat{\sigma}_x^+ e^{i\Omega_R t} + \hat{\sigma}_x^- e^{-i\Omega_R t}) \tag{3.44}$$

where $\hat{\sigma}_x^\pm = |\mp\rangle\langle\pm|$. At this point, there are no effective slow dynamics of the system as the qubit is simply being driven at a rate Ω_R. We can, however, now drive the cavity in order to transform $\hat{c}^\dagger\hat{c}$ in the above equation to make various processes resonant (Fig. 3.11). By applying a blue or red detuned sideband drive on the cavity of the form $\hat{H}_d^{\mathrm{b/r}}/\hbar = 2\epsilon\cos[(\omega_c \pm \Omega_R)t](\hat{c} + \hat{c}^\dagger)$ and going into the frame of the drive, we arrive at the effective interaction Hamiltonians:

$$\hat{H}_{\mathrm{red}}/\hbar \approx g(\hat{c}^\dagger\hat{\sigma}_x^- + \hat{c}\hat{\sigma}_x^+) \tag{3.45}$$

$$\hat{H}_{\mathrm{blue}}/\hbar \approx g(\hat{c}^\dagger\hat{\sigma}_x^+ + \hat{c}\hat{\sigma}_x^-) \tag{3.46}$$

where $g = \frac{\chi\xi}{2}$ and $\xi = \frac{\epsilon}{\Omega_R}$. Importantly, we've performed the RWA by discarding terms that rotate at $\pm\Omega_R$. We see that the red-detuned sideband enacts an exchange interaction between a photon in the cavity and an excitation in the driven qubit, whereas the blue-detuned sideband creates and annihilates excitations in pairs. This idea was first leveraged in the case where the cavity decay rate κ was larger than the effective interaction strength g, resulting in stabilization of either the driven ground or excited states $|\pm\rangle$ [Murch et al. 2012]. These dynamics have also been qualitatively demonstrated in the $g > \kappa$ regime, albeit using flux modulation rather than capacitive driving, in [Lu et al. 2017]. By further detuning the red sideband drive in the regime where an effective frequency $\Delta_c \gg g$, one can perform another dispersive Jaynes-Cummings type transformation to generate a dispersive interaction with $\hat{\sigma}_x$ rather than $\hat{\sigma}_z$ [Vool et al. 2016].

Driving both the red and blue sidebands simultaneously in the presence of the Rabi drive can constructively interfere to generate a conditional displacement interaction [Hacohen-Gourgy et al. 2016]. One can see this by adding Eqs. (3.46) and (3.45) together:

$$\hat{H}_{\mathrm{cd}}/\hbar = \hat{H}_{\mathrm{red}}/\hbar + \hat{H}_{\mathrm{blue}}/\hbar = g(\hat{c} + \hat{c}^\dagger)(\hat{\sigma}_x^+ + \hat{\sigma}_x^-) = g(\hat{c} + \hat{c}^\dagger)\hat{\sigma}_z \tag{3.47}$$

53

where we see that the conditional displacement is conditioned on a Pauli operator that lies on the equator of the Rabi qubit Bloch sphere whose poles are the eigenstates of $\hat{\sigma}_x$. Furthermore, we will see later that the phase of the sidebands can make this be any Pauli operator whose eigenstates lie in the $y - z$ plane. We will revisit this in more detail for our implementation in Chapter 5, though we will have to make some modifications to satisfy further experimental requirements.

Finally, we note that invoking a Rabi qubit has found great utility in performing noise spectroscopy at intermediate frequencies $\sim \Omega_R$, offering a powerful way to measure noise power spectral densities of a superconducting circuit's environment as inspired by NMR techniques [Geva, Kosloff, and Skinner 1995; Ithier et al. 2005; Yan 2013].

3.3.4 Extracting information from multilevel bosonic systems

Every quantum simulation protocol will have system observables of interest which an experimental implementation must be able to efficiently measure. For bosonic quantum simulation, the full density matrix may have support among multiple energy levels for each mode. Given an architecture where each bosonic mode is dispersively coupled to a qubit, how should we think about a general measurement process? We already saw in section 3.1.3 that being able to perform displacement operations and parity measurements enables reconstruction of the density matrix of a quantum harmonic oscillator via the Wigner function. While performing full state tomography is certainly a useful diagnostic and visualization tool, often times one is not interested in all of the information in the full density matrix as a system is scaled up[3]. In this section, we discuss how to generally think about the measurement of multilevel systems and highlight two examples that showcase how the extended Hilbert space can be leveraged in expanded ways.

We begin by reviewing the fundamental concepts behind quantum measurements from the positive-operator-value-measure (POVM) formalism [Nielsen and Chuang 2002]. For a given measurement scheme, we can construct a set of operators $\{\hat{E}_i\}$ known as the POVM elements that describe the possible measurement outcomes obeying $\sum_i \hat{E}_i = 1$ with cor-

---

3. We wouldn't be able to store all that information anyway as it scales exponentially with system size.
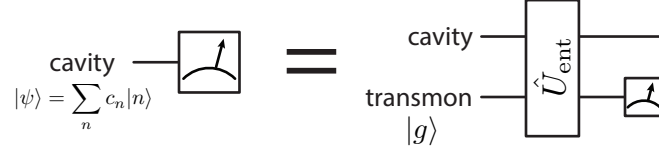
Figure 3.12 | **Measuring the cavity state using a transmon.** Measurement of some observable on the cavity Hilbert space amounts to entangling the cavity state with a transmon via $\hat{U}_{\mathrm{ent}}$ and subsequently measuring the transmon.

responding probabilities of each outcome given by $p_i = \mathrm{Tr}(\hat{\rho}\hat{E}_i)$. In the case of projective measurements, the POVM elements are equivalent to measurement operators $\hat{M}_i$ that describe how a general state is projected after a given measurement outcome. In the example of a simple qubit measured in the $\hat{\sigma}_z$ computational basis $|0\rangle_L = |g\rangle$, $|1\rangle_L = |e\rangle$, the measurement operators are simply $\hat{M}_0 = |g\rangle\langle g|$ and $\hat{M}_1 = |e\rangle\langle e|$. These measurements have the property of being quantum non-demolition (QND) if they also commute with the interaction Hamiltonian at all times during the measurement $[\hat{M}_i, \hat{H}(t)] = 0\,\forall\, i$. This means that if an initial measurement projects the system into one of the two eigenstates, all subsequent measurements will return the same result with certainty. For the dispersive Hamiltonian in circuit QED, measurements of the transmon via the readout resonator are QND since $\hat{H}_{\mathrm{int}}(t)/\hbar = -\chi\hat{a}_q^\dagger\hat{a}_q\hat{a}_r^\dagger\hat{a}_r + \varepsilon(t)(\hat{a}_r + \hat{a}_r^\dagger)$ commutes with the measurement operators $\hat{M}_0 = |g\rangle\langle g|$ and $\hat{M}_1 = |e\rangle\langle e|$.

The extension to multilevel systems is relatively straightforward. In theory, one can come up with a complete set of POVM elements that describes a set of possible measurement outcomes. In practice, we consider POVM elements associated with practical measurement schemes available to the system. In the case of a cavity dispersively coupled to a transmon qubit, measuring an operator on the cavity Hilbert space amounts to entangling the cavity state with the qubit, followed by a measurement of the qubit (Fig. 3.12). Given that the qubit can only provide one bit of information, we consider POVM elements that partition
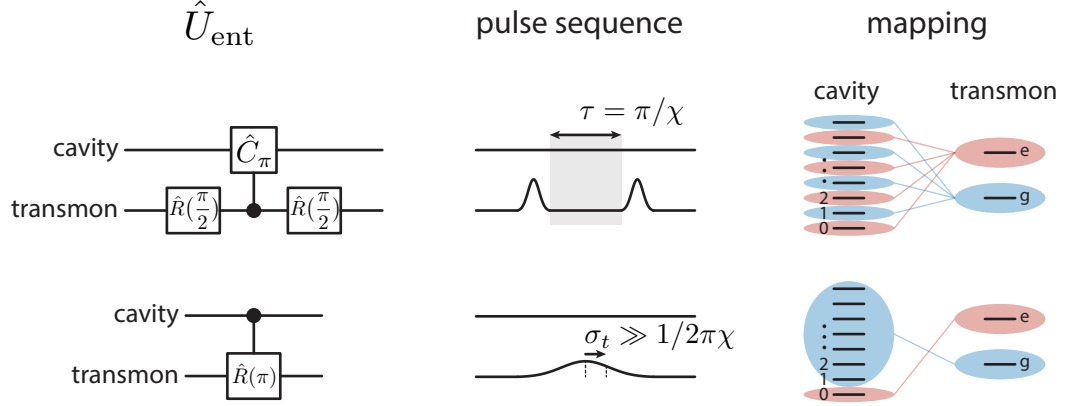
Figure 3.13 | **Measuring observables in the cavity Hilbert space.** Two standard techniques to measure parity (top) and a photon number projector (bottom, in this case $\hat{P}_0 = |0\rangle\langle 0|$) using a dispersive interaction between a cavity and transmon.

the cavity Hilbert space into two distinct subspaces S and $\bar{S}$:

$$\hat{M}_0 = \sum_{|\psi\rangle \in S} |\psi\rangle\langle\psi|$$

$$\hat{M}_1 = \sum_{|\psi\rangle \in \bar{S}} |\psi\rangle\langle\psi| = 1 - \hat{M}_0$$

(3.48)

One of the most ubiquitous but also natural tools available to our dispersive circuit QED system is enacting a measurement of the photon number parity $\hat{\Pi} = e^{i\pi\hat{a}^\dagger\hat{a}}$. The two eigenspaces correspond to even and odd photon numbers, thus the parity operator can be expressed as $\hat{\Pi} = \hat{P}_{\text{even}} - \hat{P}_{\text{odd}}$, where the projectors $\hat{P}_{\text{even/odd}} = \sum_{n\in\text{even/odd}} |n\rangle\langle n|$. The dispersive coupling naturally generates a π-phase on odd cavity photon number states after an interaction time $\tau = \pi/\chi$ with a qubit in an equal superposition state, which can be used to enact a π rotation of the transmon conditioned on the photon number parity via additional $\pi/2$ rotations (Fig. 3.13). From the perspective of our previous discussion, performing a parity measurement this way enacts the POVM elements $\{\hat{P}_{\text{even}}, \hat{P}_{\text{odd}}\}$.

The other natural tool afforded to use by the dispersive interaction is the number-selective π-pulse, as introduced previously in section 3.3.2. Here, we can now view this protocol as implementing the POVM elements $\{\hat{M}_g = \hat{1} - |n\rangle\langle n|, \hat{M}_e = |n\rangle\langle n|\}$ assuming a calibrated pulse spectrally centered on $\omega_c - n\chi + (n^2 - n)\chi'$. We note that multiple se-

lective pulses can be played simultaneously to expand the number of photon number states mapped, which we will utilize in section 3.3.4.1.

For the rest of this section, we demonstrate how our architecture can be used to both drastically improve the measurement fidelity of a qubit encoded in a multilevel bosonic mode (section 3.3.4.1) as well as extract multiple bits of information in a single measurement to directly measure the photon number (3.3.4.2). We'll use the language that these techniques fundamentally rely on repeating individual QND *readouts* to synthesize a single overall *measurement*.

3.3.4.1 The Boson Buffer

Here we describe the "Boson Buffer", a term coined by Salvatore Elder to describe a theoretical proposal [Hann et al. 2018] to improve the measurement fidelity of a bosonic qubit by leveraging the multilevel nature of the Hilbert space, which we were able to implement experimentally to achieve the highest measurement fidelity known to date in a superconducting system [Elder et al. 2020]. We elect to only highlight core concepts that exemplify how we can extract information from bosonic modes.

A continuous QND measurement, such as dispersive readout of a transmon, can be thought of as integrating a noisy signal in time that encodes qubit state information. Averaging and integrating many copies of such signals associated with the two qubit states will produce histograms that can be used to set a threshold for identifying, on a given instance, whether a single measurement trajectory is classified to be in one state or another. The overlap between the two distributions is a source of infidelity, as it corresponds to the likelihood that a signal will be misclassified. The measurement fidelity can be defined as:

$$\mathcal{F} = 1 - P(\text{"0"}|\,|1\rangle) - P(\text{"1"}|\,|0\rangle) \tag{3.49}$$

where $P(\text{"}i\text{"}|\,|j\rangle)$ is the probability of assigning an outcome "i" after measuring a state initially known to be $|j\rangle$. Note that from an experimental perspective, this says that the measurement fidelity can only be as good as the preparation fidelity.

To exponentially suppress this error, one in principle just needs to increase the measure-

ment time τ_m to increase the separation between the distributions. The main issue with measuring for longer times is that the finite relaxation time T_1 of a qubit will cause transitions from the excited state to the ground state [Gambetta et al. 2007] (where we assume there is no heating rate of the qubit $\Gamma_\uparrow = 0$). As such, the excited state distribution will have a tail that appears in the region associated with the ground state, leading to misclassification. Thus, the infidelity *solely due to decay* for short measurement times scales linearly as $1 - \mathcal{F} \sim 1 - \tau_m/T_1$, given that only a single decay event needs to happen to mix the computational basis states.

One might also think that a way around this is to measure more strongly such that the signal-to-noise ratio (SNR) will be larger for a given dt of the measurement. The issue with this, unfortunately, is that one typically sees that the relaxation time of the qubit increases with measurement strength, which may actually lead to a decrease in the measurement fidelity [Sank et al. 2016]. The origin of this effect is not fully understood and is a central challenge for the community moving forward, as every quantum error correction relies on fast, faithful measurements. In fact, this phenomena motivates a practical definition of QND-ness: how much does a measurement *increase* the decay rate of a system?

The same concept can be applied to our previous discussion of measuring a high-Q cavity using the transmon, where the readout interval is now discrete instead of continuous. If the cavity never transitions between eigenstates, then individual readouts with symmetric infidelity δ can be repeated and the infidelity of the overall measurement is exponentially suppressed in the number of readouts N via a majority voting scheme. By including error due to the cavity decay rate $\kappa_\downarrow$, the infidelity for distinguishing between Fock states $|0\rangle$ and $|1\rangle$ can be approximated as:

$$1 - \mathcal{F}_{01} \approx 2 \begin{pmatrix} N \\ \lceil N/2 \rceil \end{pmatrix} \delta^{\lceil N/2 \rceil} + \lceil N/2 \rceil \kappa_\downarrow \tau_m \tag{3.50}$$

where τ_m is the time for a single readout (including the mapping) and we are assuming that $\{N\delta, N\kappa_\downarrow\tau_m\} \ll 1$. This is in direct analogy with measuring the ground and excited state of a transmon, where one is typically limited by a single decay event. The approach taken
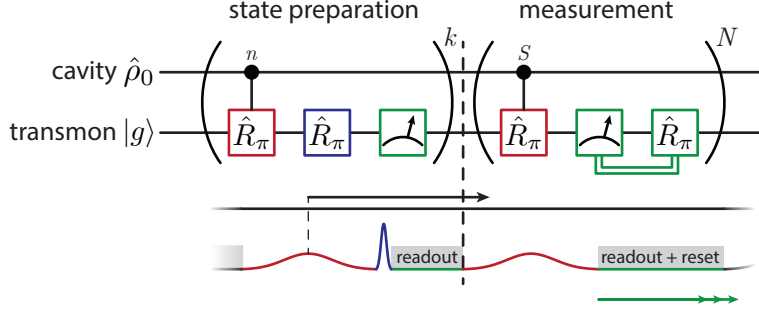
Figure 3.14 | **Quantum circuit and pulse sequence for the Boson Buffer.** An initial cavity state $\hat{\rho}_0$ that has a nontrivial overlap with a target Fock state $|n\rangle$ is "filtered" through a series of k check pre-measurements involving a selective and unselective π-pulse. Only cases where the transmon's pre-measurement record is all "g" are kept. The infidelity of the cavity state will ultimately be set by decay of the cavity beginning from the second half of the pulse to the beginning of the actual measurement (black arrow). The measurement itself involves roughly the same sequence, except the transmon is dynamically reset to its ground state on every round (which can take a variable amount of time).

by the Boson Buffer is to increase the distance[4] in Hilbert space between the qubit states by encoding the excited state in a higher photon number Fock state $|1\rangle_L = |L\rangle$. By leveraging the fact that photons decay one at a time, increasing the distance between the codewords in the Fock basis decreases the infidelity bound *exponentially* in the code distance:

$$1 - \mathcal{F}_{0L} \approx 2 \binom{N}{\lceil N/2 \rceil} \delta^{\lceil N/2 \rceil} + (\lceil N/2 \rceil \kappa_\downarrow \tau_m)^L \tag{3.51}$$

An overview of the experimental sequence is shown in Fig. 3.14. The goal is to encode a qubit in two Fock states of a cavity $\{|0\rangle_L = |0\rangle, |1\rangle_L = |L\rangle\}$ and quantify the measurement fidelity via

$$\mathcal{F} = 1 - P(S \,|\, |1\rangle_L) - P(\bar{S} \,|\, |0\rangle_L) \tag{3.52}$$

where S and $\bar{S}$ should be optimally chosen to balance the infidelity contributions in a way that minimizes the total infidelity. As one can see, there are striking similarities between the state preparation and measurement units.

The purpose of the state preparation scheme is to initialize a Fock state $|n\rangle$ with the

---

4. We note that "distance" here is defined with respect to the form of the dissipation which only connects neighboring Fock states.

highest possible fidelity. This is a requirement in the sense that the measurement fidelity can only be as good as the preparation fidelity. Each individual round in the state preparation circuit implements the POVM elements $\hat{M}_0 = |n\rangle\langle n|$ and $\hat{M}_0 = |\bar{n}\rangle\langle\bar{n}|$, though there will be errors due to transmon decoherence and readout infidelity. By repeating this multiple time and post-selecting on sequences where the measurement outcomes were all "0", we suppress these errors exponentially in the number of rounds. Thus, the remaining infidelity is completely determined by decay of the cavity state during the duration of the final check measurement.

While the state preparation is specific to the target Fock state being prepared by conditioning the transmon rotations on $|n\rangle$, the measurement itself will be conditioned on the choice of S for distinguishing both qubit states. We further dynamically reset the transmon to its ground state after every round in order to suppress errors due to relaxation. By taking a majority vote of individual readouts, the infidelity due to measurement errors is exponentially suppressed in the rounds. The optimal number of measurements using majority voting will be determined by when the infidelity reaches the limit set by relaxation, which is overall exponentially suppressed in the distance. Instead, one can use an optimal maximum-likelihood estimator (MLE) that takes into account the expected relaxation at long times.

In our experimental implementation, we choose a Fock code where $|0\rangle_L = |0\rangle$ and $|1\rangle_L = |5\rangle$ and show the results for a majority voting scheme (Fig. 3.15). We choose the subspace S to be spanned by $\{|0\rangle, |1\rangle\}$ in order to offer protection against a single heating event, which translates to the mapping consisting of simultaneous selective π-pulses on the $n = \{0, 1\}$ peaks of the cavity. The results track closely with the expected predictions, but only upon post-selecting on events where the transmon was successfully reset to its ground state within 5 attempts. While the reset success rate should ideally also be exponential in the number of rounds, we observe a secondary timescale corresponding to the transmon being "stuck" in a higher excited state. A fair measurement, of course, should not rely on post-selection since that exponentially reduces the success rate of a measurement outcome in the number of qubits in an algorithm, though we only throw out 0.2% of the data. Finally, this scheme can be applied to logical measurements of bosonic error correcting codes that

60
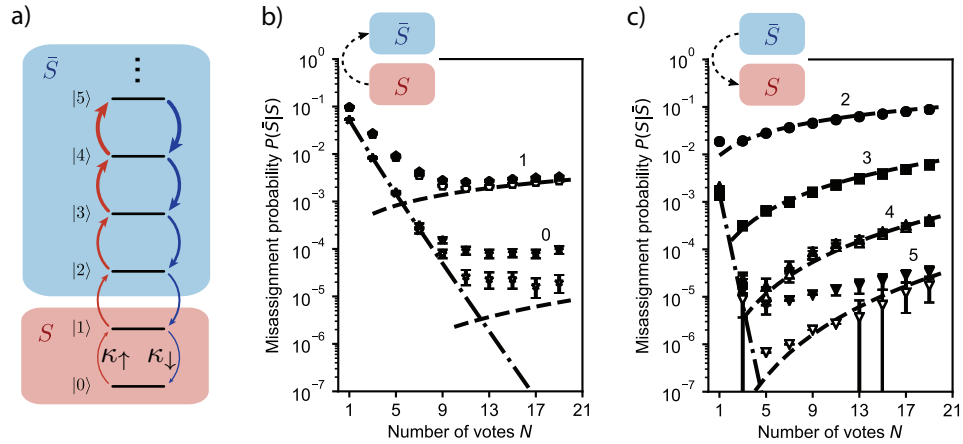
Figure 3.15 | The Boson Buffer. (a) Mapping sequence used to optimally distinguish $|0\rangle$ and $|5\rangle$, chosen to balance heating and decay rates. (b & c) Probability that a state prepared in S is identified to be in $\bar{S}$, and vice-versa in (c). Dashed-dotted lines represent exponential suppression of individual readout infidelity in the number of readout rounds, whereas the dashed line estimates the infidelity bound due to heating (b) and decay (c). Solid markers are data points, and hollow markers refer to data points post-selected on the transmon being reset properly in between rounds. Adapted from [Elder et al. 2020].

have disjoint photon number support such as the binomial codes [Michael et al. 2016]. For complete details of the protocol and experiment, we again refer the reader to [Hann et al. 2018; Elder et al. 2020].

3.3.4.2 A single-shot number-resolved photodetector

In the previous section, we saw how repeating the same QND readout of the cavity enabled a dramatic improvement of the measurement fidelity of a single bit of information. Here, we consider how performing QND readouts of different operators in a single measurement instance allows one to extract more than one bit of information such as the photon number. Such a detector has a wide range of applications for linear optical protocols, and we were motivated to develop a version for our circuit QED system in order to perform the experiment in Chapter 4 in a scalable way. Here, we describe the theory behind such a detector, and refer the reader to details of the experimental implementation in section 4.3.4.2.

As we saw previously, the transmon can be used to measure a binary-valued operator on a dispersively coupled cavity. The selective π-pulses in section 3.3.2 are an example
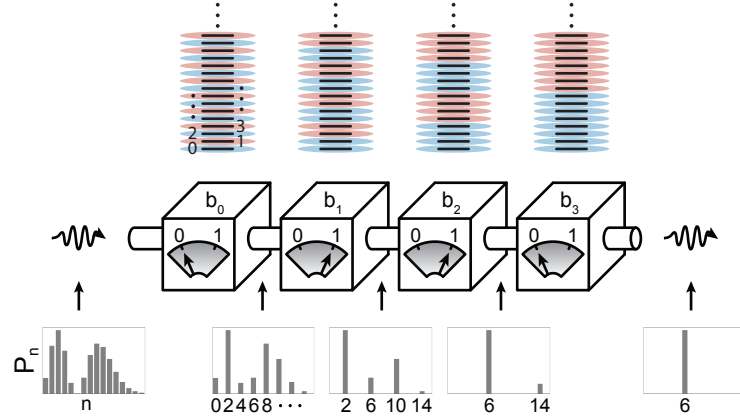
Figure 3.16 | **A number-resolved photodetector.** Top: qubit mapping for each generalized parity operator. Bottom: sequential QND readouts of the first four generalized parity operators can resolve up to 15 photons. Each measurement projects the cavity state into the eigenspace of the operator being measured, ultimately projecting out a single Fock state with its corresponding probability. In the schematic, a sequence sampling the 6 photon component ($|6\rangle = |0110\rangle$) from a displaced Fock state is shown. The state is first probabilistically measured to be in the $b_0 = 0$ (even parity) subspace, thus projecting out only even photon numbers. The next measurement further projects this state into the $b_1 = 1$ subspace, and so on, until the measurement converges on a single photon number.

of this as they effectively implement the following measurement operators on the cavity Hilbert space: $\hat{M}_0 = |\bar{n}\rangle\langle\bar{n}|$ and $\hat{M}_1 = |n\rangle\langle n|$. If a transmon initially in its ground state is successfully flipped to the excited state, it implies that the cavity indeed had n photons which performs the mapping:

$$|g\rangle \otimes \sum_m c_m |m\rangle \rightarrow |g\rangle \otimes \sum_{m \neq n} c_m |m\rangle + c_n |e\rangle \otimes |n\rangle \tag{3.53}$$

A subsequent measurement of the transmon will then collapse the above superposition into a definite subspace of the cavity. One sees from this simple example, however, that the relative amplitudes in the remaining subspace of $\hat{M}_g$ are left undisturbed up to a renormalization. This means that there is still more information to extract further if one so desired.

Our strategy for measuring the number of photons for a given cavity state is to represent the photon number via its binary decomposition $|n\rangle = \left|\Pi_{k=k_{\max}}^{k=0} b_k\right\rangle$, where $n = \sum_{k=0}^{k_{\max}} 2^k b_k$ and $\{b_k\} \in \{0, 1\}$, and then to sequentially measure each bit b_k on a given run of the experiment. This amounts to identifying a set of parity operators $\hat{P}_k$ in the cavity Hilbert space whose eigenvalues $\lambda_{k,\pm} = \pm 1$ correspond to $b_k = \{0, 1\}$, respectively, with the following

matrix elements ij:

$$(\hat{P}_k)_{ij} = \begin{cases} 0 & \text{if } i \neq j \\ 1 - 2\left(\lfloor \frac{i}{2^k} \rfloor \pmod 2 \right) & \text{if } i = j \end{cases} \quad v \qquad (3.54)$$

where $\lfloor \cdot \rfloor$ denotes the floor function. By sequentially performing measurements of the first k bits, one can resolve up to $n \bmod 2^{k_{\max}}$ different Fock states. If the state is a-priori known to have support only within the Hilbert space up to $2^{k_{\max}} - 1$ photons, then this sequence projects the cavity into a definite photon number.

Chapter 4

Multiphoton sampling of molecular vibronic spectra

In section 2.1.4, we described how to model vibronic spectra involving two electronic states. We introduced Franck-Condon factors as wave-function overlaps that encoded information regarding the structural relationship between the nuclear configurations of each electronic state. In this chapter, we describe our implementation of a quantum algorithm for estimating Franck-Condon factors in associated photoelectron spectra [Wang et al. 2020].

The algorithm, originally developed in [Huh et al. 2015], considered how to connect a known computationally challenging but artificial task of boson sampling [Aaronson and Arkhipov 2011] and connect it to a problem of practical relevance. Despite being originally developed for a linear optical platform, the algorithm is general and can be implemented in any bosonic quantum simulator with access to the requisite capabilities. As such, demonstrations on both linear optical devices [Clements et al. 2018; Paesani et al. 2019] and a single trapped-ion [Shen et al. 2018] have been shown. Fully integrating all the capabilities with high fidelity in a scalable manner, however, had still been elusive. Our experiment definitively achieved this using a superconducting circuit QED architecture.

4.1 A boson sampling algorithm for estimating Franck-Condon factors

In this section, we introduce the algorithm from a physical perspective. We begin with a Hamiltonian Eq. (2.23) that assumes adiabatic separation between two electronic states $\{|g\rangle, |e\rangle\}$ and apply the harmonic approximation to all $N_{\text{vib}} = 3N_n - (5)6$ vibrational degrees of freedom of a (linear) nonlinear molecule:

$$\mathcal{H}/\hbar = |g\rangle \langle g| \otimes \sum_{i=1}^{N_{\text{vib}}} \omega_i^g \hat{a}_i^\dagger \hat{a}_i + |e\rangle \langle e| \otimes \sum_{i=1}^{N_{\text{vib}}} \omega_i^e \hat{b}_i^\dagger \hat{b}_i \tag{4.1}$$

where $\{\hat{a}_i^{(\dagger)}\}$ and $\{\hat{b}_i^{(\dagger)}\}$ are the creation and annihilation operators for the vibrational modes of the pre-transition and post-transition electronic states, respectively. As Eq. 2.27 suggests, the Franck-Condon factors are equivalent to the wave-function overlap between an initial vibrational state and the complete set of final vibrational eigenstates. The central idea, then, is to use a quantum simulator to directly perform a unitary transformation of the initial state into the basis of final states, and then sample the number distribution.

We can think about the transformation first in real space, first formulated by Duschinsky [Duschinsky 1937]:

$$\mathbf{Q}'' = U\mathbf{Q}'' + \mathbf{d} \tag{4.2}$$

where $\mathbf{Q}'$ and $\mathbf{Q}''$ are mass-weighted normal coordinates of the pre-transition and post-transition molecular configurations, respectively. U is the Duschinsky rotation matrix, which describes the degree to which the normal modes mix in one basis with respect to another, and $\mathbf{d}$ is a shift vector that describe the relative shift of the equilibrium configurations. The Duschinsky transformation Eq. 4.2 can be translated into a canonical transformation on the creation and annihilation operators as formulated by Doktorov and co-workers [Doktorov, Malkin, and Man'Ko 1977]:

$$\hat{\mathbf{b}} = \hat{U}_{\text{Dok}} \hat{\mathbf{a}} \hat{U}_{\text{Dok}}^\dagger \tag{4.3}$$

$$\hat{U}_{\text{Dok}} = \hat{\boldsymbol{D}}(\boldsymbol{\alpha}) \hat{\boldsymbol{S}}^\dagger(\boldsymbol{\zeta}') \hat{\boldsymbol{R}}(U) \hat{\boldsymbol{S}}(\boldsymbol{\zeta}) \tag{4.4}$$
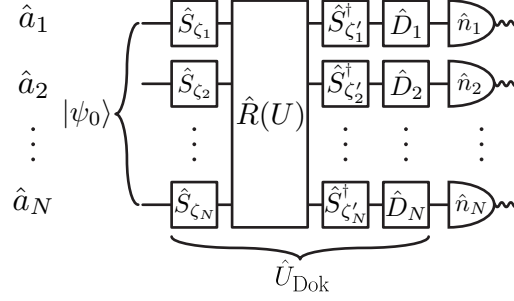
Figure 4.1 | **Boson sampling algorithm for Franck-Condon factors.** An initial state multi-mode bosonic state $|\psi_0\rangle$ across N modes is transformed under $\hat{U}_{\mathrm{Dok}}$ to produce a post-transition state, which is then sampled in the number basis across all modes to produce a spectrum of Franck-Condon factors.

where

$$\hat{\boldsymbol{D}}(\boldsymbol{\alpha}) = \hat{D}(\alpha_1) \otimes \hat{D}(\alpha_2) \otimes ... \otimes \hat{D}(\alpha_N) \tag{4.5}$$

$$\hat{\boldsymbol{S}}^{(\dagger)}(\boldsymbol{\zeta}^{(\prime)}) = \hat{S}^{(\dagger)}(\zeta_1^{(\prime)}) \otimes \hat{S}^{(\dagger)}(\zeta_2^{(\prime)}) \otimes ... \otimes \hat{S}^{(\dagger)}(\zeta_N^{(\prime)}) \tag{4.6}$$

correspond to a tensor product of single-mode displacement and squeezing operations across all N modes, respectively. $\hat{\boldsymbol{R}}(U)$ is an N-mode rotation operator corresponding to the $N \times N$ Duschinksky rotation matrix U which can be decomposed into a product of two-mode rotation operations [Reck et al. 1994].

The algorithm (Fig. 4.1) thus consists of preparing an initial state $|\psi_0\rangle$ corresponding to a pre-transition vibrational state, enacting $\hat{U}_{\mathrm{Dok}}$ to transform it into the basis of post-transition vibrational eigenstates, and then sampling the number distribution to obtain the FCFs. We further note that Eq. 4.4 is not unique: one can re-order the operations to facilitate ease of implementation based on the native capabilities of the platform used [Huh et al. 2015].

At this point we comment on a central feature of our computational task. If $\hat{\boldsymbol{R}}(U)$ is, or can be very well approximated as, block-diagonal, then we are able to essentially break the problem into smaller sub-problems, as the block-diagonal subspaces do not interact with each other. This has implications for the computational cost of solving a given problem, which we elaborate on in section 4.4.1.

4.1.1 Obtaining Doktorov parameters from molecular parameters

Implementing the Doktorov transformation requires knowledge about how each harmonic potential energy surface is parameterized both individually and with respect to each other, which requires classical electronic structure calculations. These calculations provide the vibrational frequencies in the pre-transition and post-transition bases, Duschinsky rotation matrix, and shift vector.

The vibrational frequencies $\{\tilde{\nu}_i^{(')}\}$ enter into the Doktorov transformation as arguments for the squeezing and anti-squeezing operations: $\zeta_i^{(')} = \ln\left(\sqrt{\tilde{\nu}_i^{(')}}\right)$. At first glance, this appears incorrect given that a logarithm is being taken of a number with units. However, by looking at an alternative form of how the creation and annihilation operators are transformed [Malmqvist and Forsberg 1998]:

$$\hat{\mathbf{a}}'^{\dagger} = \frac{1}{2}(L - (L^T)^{-1})\hat{\mathbf{a}} + \frac{1}{2}(L + (L^T)^{-1})\hat{\mathbf{a}}^{\dagger} + \vec{\alpha} \tag{4.7}$$

where

$$L = \Omega' U \Omega^{-1}$$

$$\Omega = \begin{pmatrix} \sqrt{\tilde{\nu}_1} & & 0 \\ & \ddots & \\ 0 & & \sqrt{\tilde{\nu}_N} \end{pmatrix} \quad \Omega' = \begin{pmatrix} \sqrt{\tilde{\nu}'_1} & & 0 \\ & \ddots & \\ 0 & & \sqrt{\tilde{\nu}'_N} \end{pmatrix} \tag{4.8}$$

one can see how the structure of L allows for a free scaling parameter η which leaves L invariant, namely:

$$\tilde{\Omega}^{(')} = \Omega^{(')}/\eta$$

$$L(\Omega, \Omega') = L(\tilde{\Omega}, \tilde{\Omega}')$$

Thus an optimization may be performed, as done in [Shen et al. 2018], that minimizes the total amount of squeezing while leaving the unitary invariant. This is desirable as less squeezing corresponds to shorter gate times in the simulation, which reduces the overall

error rate.

The Duschinsky rotation matrix U generates the N-mode rotation operator $\hat{\mathbf{R}}(U)$. For an architecture with linear connectivity that has access to nearest-neighbor two-mode rotations, this requires a decomposition of U, and thus $\hat{\mathbf{R}}$, into nearest-neighbor rotations. $\hat{\mathbf{R}}(U)$ becomes a product of two mode rotations parametrized by $\{\theta_k\}$ and $\{i_k, j_k\}$, a sequence of angles and rotation axes derived from the decomposition of $U = \prod_k R_{i_k,j_k}(\theta_k)$. We can then write:

$$\hat{\mathbf{R}}(U) = \prod_k \exp\big(\theta_k(\hat{a}_{i_k}\hat{a}_{j_k}^{\dagger} - \hat{a}_{i_k}^{\dagger}\hat{a}_{j_k})\big) \tag{4.9}$$

The decomposition of U is analogous to generalizing Euler angles to SO(N); any rotation in $\mathbf{R}^N$ can be written as a product of rotations in a plane $R_{i_k,j_k}(\theta_k)$, known as Givens rotations. Following an algorithm similar to that in [Reck et al. 1994; Cybenko 2001], but simplified to real orthogonal matrices, produces a decomposition of U as a product of nearest-neighbor rotations.

Finally, the dimensionless displacement strengths $\{\alpha_i\}$ are directly related to the elements $\{d_i\}$ of the shift vector:

$$\alpha_i = \sqrt{\frac{\omega_i^{(')}}{2\hbar}} d_i \tag{4.10}$$

4.2 Experimental design and setup

Here, we set the stage for our experiment. As previously described, the requirements for implementing the FC algorithm are individual state preparation and measurement of each bosonic mode and a complete set of Gaussian operations across all bosonic modes, where the building block for a N-mode rotation operation can be simply a two-mode rotation. Looking at our bosonic circuit QED architecture, we can envision a linear array of cavity modes that are connected via nearest-neighbor coupler transmons and each couple to individual control modules with an ancilla transmon and readout resonator (Fig. 4.2). For this experiment, we realize a minimal foundation of such an architecture with two cavity modes, two control modules, and one coupler transmon as first introduced in section 3.3.

The FC algorithm can be treated as a standard quantum algorithm decomposed into
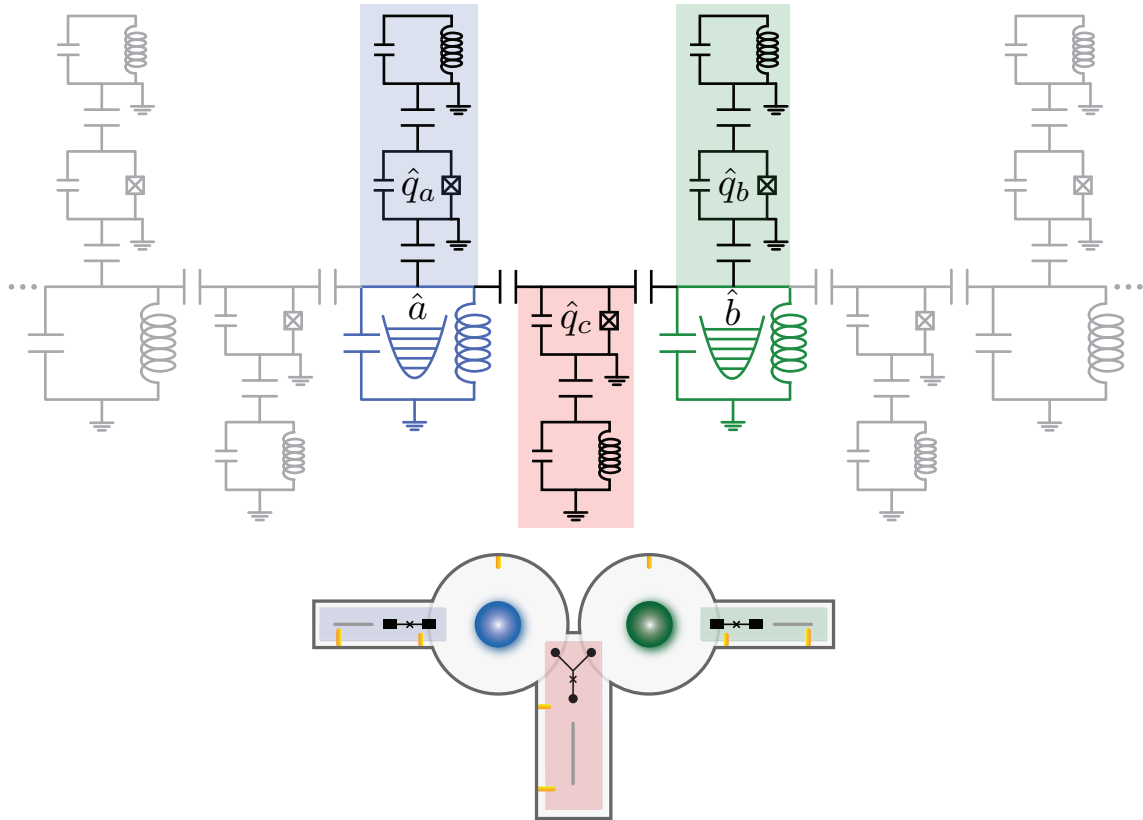
Figure 4.2 │ Circuit QED architecture for generalized boson sampling algorithms. Top: 1D array of cavity modes with nearest-neighbor coupler transmons and individual control modules for state preparation and measurement. Bottom: Depiction of the two cavity circuit QED device used in this experiment.

bosonic "gates" to enact a desired unitary transformation. In this sense, the appropriate metric to optimize is simply the fidelity of each component of the algorithm, including the measurement. From a design perspective, this translates to enacting faithful operations while minimizing unwanted interactions and decoherence. Fortunately, the relatively long lifetimes of the cavity modes allows us to enact only rather modest interaction strengths.

Perhaps the most central challenge, as we will see in the next section, is orchestrating and compiling the various interactions such that the algorithm is fully programmed. That is to say, we should be able to simulate different molecules simply by changing the input controls as determined by classical computations. We fulfill this requirement, and as such, claim that we have implemented a programmable bosonic simulator for the FC algorithm.

to ADC

to ADC

to ADC (ref)   to ADC

300 K

4 K

20 mK

RF generator   -xx dB attenuator

mixer   low pass filter

amplifier   eccosorb filter

RF switch   circulator

bandstop filter   isolator

-xx dB directional coupler

ancilla B   Bob   Alice   ancilla A

coupler

cryoperm shield

X = ZX60-153LN-S+
A = ZVA-183-S+
E = ZVE-3W-83+
H = HEMT
Q = MITEQ
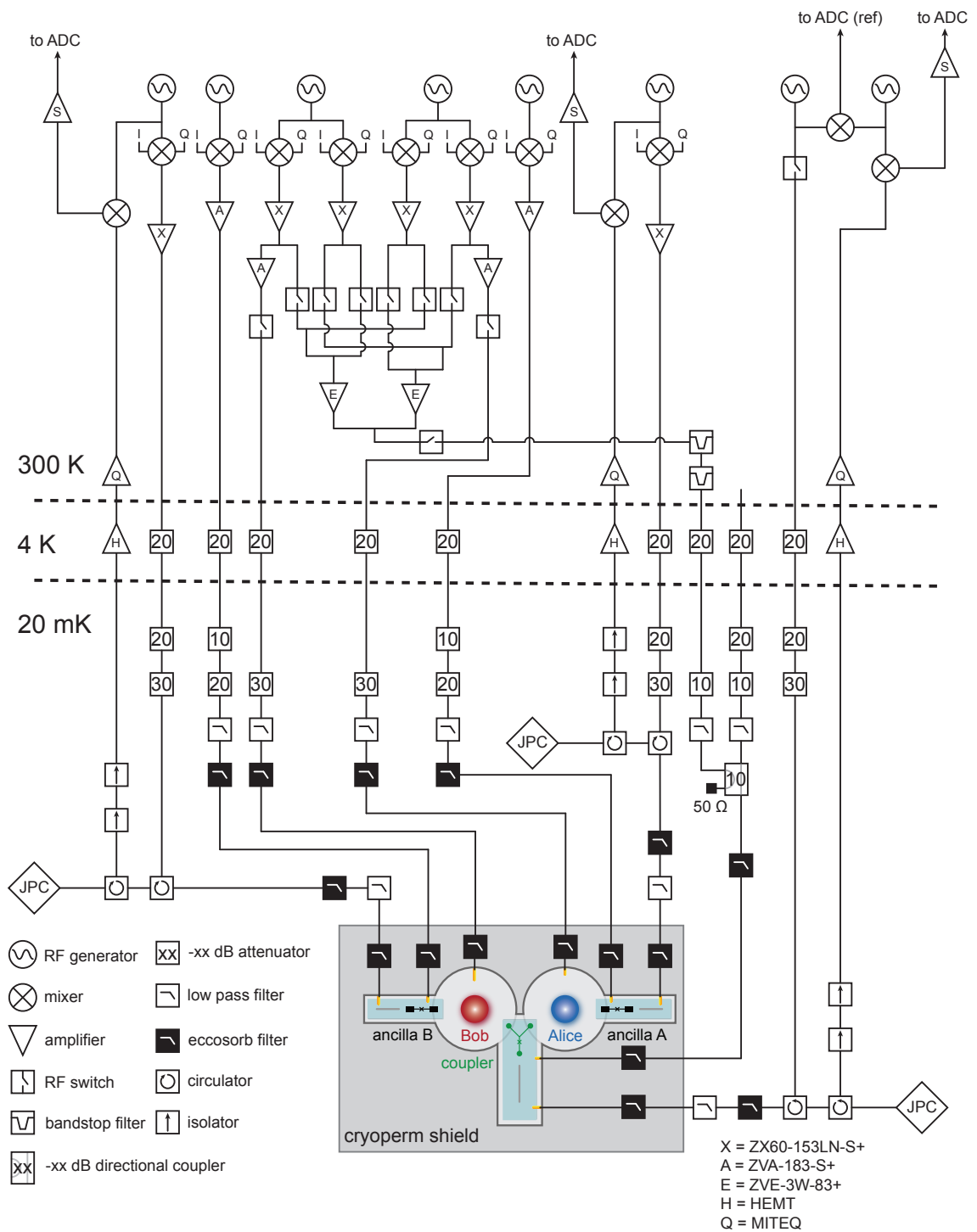
Figure 4.3 │ **Experimental wiring diagram for the Franck-Condon experiment.**

4.2.1 Experimental controls

The wiring diagram for our experiment is shown in Fig. 4.3. The device itself is mounted in a Cryoperm® shield anchored to the base of a dilution refrigerator operating at $\sim 20\,\mathrm{mK}$.

An in-depth description of the control hardware and software used is given in [Reinhold 2019], but we highlight the key concepts here. The controller consists of four Innovative Integration X6-1000M boards housed in a VPXI-ePC system that synchronizes and orchestrates the inputs/output control signals. Each board provides digital-to-analog converters (DACs) that produce the pulses and analog-to-digital converters (ADCs) that record and digitize readout signals. The DACs and ADCs are mediated by a Xilinx Virtex 6 SX475T field-programmable-gate-array (FPGA) that defines the logic determining how control and feedback sequences may be programmed. All pulses are generated by the DACs at an intermediate frequency $|\omega_{\mathrm{IF}}|/2\pi < \sim 130\,\mathrm{MHz}$ with amplitude and phase control in a mode of operation with 2 ns resolution. These pulses are upconverted to our mode frequencies $\omega_{\mathrm{RF}}/2\pi \sim 4-10\,\mathrm{GHz}$ via single sideband modulation of a local oscillator (LO) via Marki IQ mixers and subsequently amplified by an appropriate amount before entering the cryostat. RF switches are often used to gate pulses and avoid potential loops in the control chain.

A central feature of our control chain to highlight is how the various drive tones are generated. Two local oscillators that produce tones at $\omega_c - \delta$, where $\delta/2\pi = 95\,\mathrm{MHz}$ and $c \in \{a, b\}$, are each split before being mixed via two IQ pairs which produce either the resonant drives sent directly to the cavity ports ($\omega_{\mathrm{IF}}/2\pi = 95\,\mathrm{MHz}$) or the pump tones which are combined, amplified, and sent to the coupler port. RF switches enable only a single pair of tones to be played at a time and notch filters help suppress noise at the cavity frequencies. Importantly, all these tones are phase-locked with respect to each other.

Finally, we use Josephson parametric converters (JPCs) [Bergeal et al. 2010] as a quantum-limited amplifier for faciliating high-fidelity qubit readout. Microwave lines for delivering the pump tones are not shown in the wiring diagram.

System quantity	Parameter	Value
Coupler frequency	$\omega_c/2\pi$	5947 MHz
Coupler anharmonicity	$\alpha_c/2\pi$	70.5 MHz
Coupler relaxation	T_1^c	25 μs
Alice frequency	$\omega_a/2\pi$	5467 MHz
Alice linewidth	$\kappa_a/2\pi$	0.6 kHz
Bob frequency	$\omega_b/2\pi$	6548 MHz
Bob linewidth	$\kappa_b/2\pi$	0.48 kHz
Alice - Coupler coupling	$\chi_{ac}/2\pi$	466 kHz
Bob - Coupler coupling	$\chi_{bc}/2\pi$	263 kHz
Ancilla A frequency	$\omega_{qa}/2\pi$	4605 MHz
Ancilla A relaxation	T_1^{qa}	55 μs
Ancilla A decoherence	T_2^{qa}	2.5 μs
Alice - Ancilla A coupling	$\chi_{a,qa}/2\pi$	748 kHz
Ancilla B frequency	$\omega_{qb}/2\pi$	4929 MHz
Ancilla B relaxation	T_1^{qb}	74 μs
Ancilla B decoherence	T_2^{qb}	23 μs
Bob - Ancilla B coupling	$\chi_{b,qb}/2\pi$	1240 kHz

Table 4.1 | List of system parameters for the Franck-Condon experiment.

4.3   Experimental implementation

In this section, we describe the details of our experimental implementation. The static system parameters is given in Table 4.1. Fig. 4.4 provides a translation between the high level quantum circuit for the two-mode FC algorithm and a more detailed version for our circuit QED system.

4.3.1   State preparation

The initial state for the FC algorithm represents the initial vibrational state of a molecule prior to an electronic transition. At $T = 0\,\mathrm{K}$, this will be the ground state which is simply the vacuum state across all modes. We will also consider spectra starting from vibrational excited states, necessitating the preparation of Fock states. This can also be used to model emission spectra where emitted photons are filtered by frequency, revealing lines that end in a distinct vibrational excited state of an electronic ground state. We use optimal control pulses described in section 3.3.2.3 to initialize Fock states and then purify the fidelity by performing a series of check measurements as was done in section 3.3.4.1 [Elder et al.
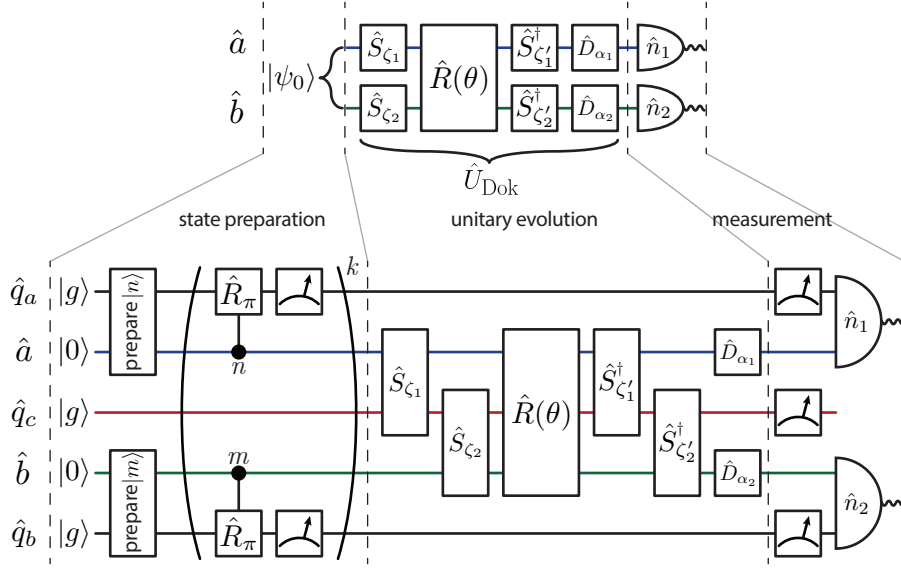
Figure 4.4 | **Experimental circuit diagram for the Franck-Condon experiment.** Top: Abstract quantum circuit for implementing the FC algorithm on two modes. Bottom: Detailed quantum circuit for our experimental implementation. We do not explicitly perform any preparation operations in the case where we aim to prepare a vacuum state $|0\rangle$. The measurement schemes are expanded on further in section 4.3.4.

2020].

4.3.2 Calibrating Gaussian operations

Here we discuss calibration of the Gaussian operations in the Doktorov transformation. We already covered how to calibrate a displacement operation in section 3.3.2.2, where one scans the amplitude of a resonant pulse. We implement the other two Gaussian operations, single-mode squeezing and two-mode beamsplitter, via four-wave mixing as introduced in section 3.3.3.1. These bilinear operations require two "pump" drives that satisfy the appropriate resonance conditions. We can formulate this very generally in the case where both pumps are applied to a transmon mode $\hat{t}$ that is coupled to a cavity $\hat{a}$:

$$\hat{H}/\hbar = \omega_t \hat{t}^\dagger \hat{t} + \omega_a \hat{a}^\dagger \hat{a} - \frac{E_J}{4!}\left(\varphi_t(\hat{t} + \hat{t}^\dagger) + \varphi_a(\hat{a} + \hat{a}^\dagger)\right)^4 + \sum_{i=1}^{2} 2\varepsilon_i \cos(\omega_i t + \varphi_i)(\hat{t} + \hat{t}^\dagger) \quad (4.11)$$

In the case of single-mode squeezing, the resonance condition for the two pumps is $\omega_{1/2} = \omega_a \mp \delta$. By performing a series of rotating frame and displacement transformations
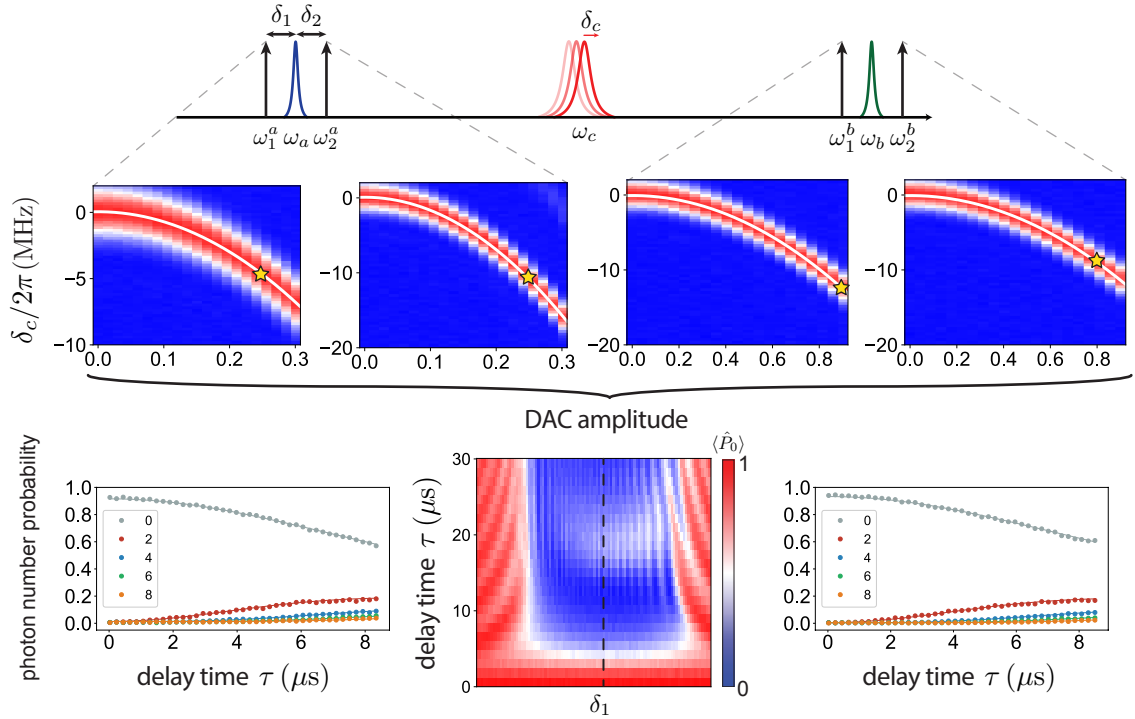
Figure 4.5 | Experimentally calibrating single-mode squeezing. Stark shift measurements on the coupler transmon as a function of individual pumps detuned $\delta_2 = \delta_1 = 2\pi \times 15\,\text{MHz}$ from ω_a and $35\,\text{MHz}$ from ω_b. Solid lines are a fit to a quadratic function. A representative 2D scan (middle, bottom) of the lower pump frequency and delay time while keeping the upper pump frequency fixed and measuring vacuum population in the cavity after starting in $|0\rangle$. Additional features after $\tau > 10\,\mu\text{s}$ are due to self-Kerr interactions, but can be neglected for low to moderate amounts of squeezing. Parking roughly at the center of the resonance for amplitudes labeled in the yellow stars and measuring photon number populations as a function of time reveals characteristic squeezing evolution with only even photon numbers being populated. Fitting the populations to Eq. 4.13 gives a calibration of $g_{\text{sq}} = 2\pi \times 9.55\,\text{kHz}$.

and discarding rapidly rotating terms (see Appendix B), we arrive at the following effective Hamiltonian:

$$\hat{H}_{\text{sq}}/\hbar = |\xi_1|^2(2\chi_{tt}\hat{t}^\dagger\hat{t} + \chi_{ta}\hat{a}^\dagger\hat{a}) + |\xi_2|^2(2\chi_{aa}\hat{a}^\dagger\hat{a} + \chi_{at}\hat{t}^\dagger\hat{t}) + g_{\text{sq}}(e^{i\theta_{\text{sq}}}\hat{a}^2 + e^{-i\theta_{\text{sq}}}\hat{a}^{\dagger 2}) \quad (4.12)$$

where the first two terms correspond to Stark shifts and the final term is our desired squeezing term, where $g_{\text{sq}} = E_J\varphi_t^2\varphi_a^2|\xi_1||\xi_2|$. Here, $\xi_{1/2} = \varepsilon_{1/2}/(\omega_{1/2} - \omega_t)$ is the dimensionless amplitude induced in the transmon mode from the drives. From this, we can see that information regarding the Stark shifts from the individual pumps informs us as to how large

of an interaction strength we can get when we play both pumps simultaneously. Thus, the calibration approach is to first measure the Stark shift on the transmon mode as a function of each pump at a frequency that we roughly expect to operate the interaction. We choose to measure the transmon mode given that the anharmonicity $\chi_{tt}/2\pi \sim 70\,\mathrm{MHz}$ is the largest energy scale of the system and thus we can easily resolve the Stark shift spectroscopically. Next, we can play both pumps simultaneously and find a resonance condition that includes all of the Stark shifts. Finally, we can perform time-domain measurements of the photon number populations which should follow

$$P(2l) = \frac{(2l)!}{2^{2l}(l!)^2} \frac{\tanh^{2l}(2g_{\mathrm{sq}}\tau)}{\cosh(2g_{\mathrm{sq}}\tau)} \tag{4.13}$$

to extract g_{sq} and correspondingly calibrate a unit time of squeezing. This process is summarized in Fig. 4.5 for both cavities.

We note that in our system, each cavity is coupled to two transmons — thus, we can choose to drive either transmon via their respective coupling ports to use their respective nonlinearity to activate the squeezing operation. The optimal choice depends on many things encompassed in the full impedance as seen from either port. In practice, we choose to activate squeezing of both cavities by driving the coupler transmon.

Next, we perform a similar process for the beamsplitter operation (Fig. 4.6), but now we need to consider two cavity modes a and b:

$$\begin{aligned}
\hat{H}/\hbar &= \omega_t \hat{t}^\dagger \hat{t} + \omega_a \hat{a}^\dagger \hat{a} + \omega_b \hat{b}^\dagger \hat{b} - \frac{E_J}{4!}\big(\varphi_t(\hat{t}+\hat{t}^\dagger) + \varphi_a(\hat{a}+\hat{a}^\dagger) + \varphi_b(\hat{b}+\hat{b}^\dagger)\big)^4 \\
&\quad + \sum_{i=1}^{2} 2\varepsilon_i \cos(\omega_i t + \varphi_i)(\hat{t}+\hat{t}^\dagger)
\end{aligned} \tag{4.14}$$

Now, we choose the pump frequencies to satisfy $\omega_2 - \omega_1 = \omega_b - \omega_a$, which ultimately gives us [Pfaff et al. 2017; Gao 2018]:

$$\begin{aligned}
\hat{H}_{\mathrm{bs}}/\hbar &= |\xi_1|^2(2\chi_{tt}\hat{t}^\dagger\hat{t} + \chi_{ta}\hat{a}^\dagger\hat{a} + \chi_{tb}\hat{b}^\dagger\hat{b}) + |\xi_2|^2(2\chi_{tt}\hat{t}^\dagger\hat{t} + \chi_{at}\hat{a}^\dagger\hat{a} + \chi_{bt}\hat{b}^\dagger\hat{b}) \\
&\quad + g_{\mathrm{bs}}(e^{i\theta_{\mathrm{bs}}}\hat{a}^\dagger\hat{b} + e^{-i\theta_{\mathrm{bs}}}\hat{a}\hat{b}^\dagger)
\end{aligned} \tag{4.15}$$

We can model decoherence under the beamsplitter operation in a single-photon sub-
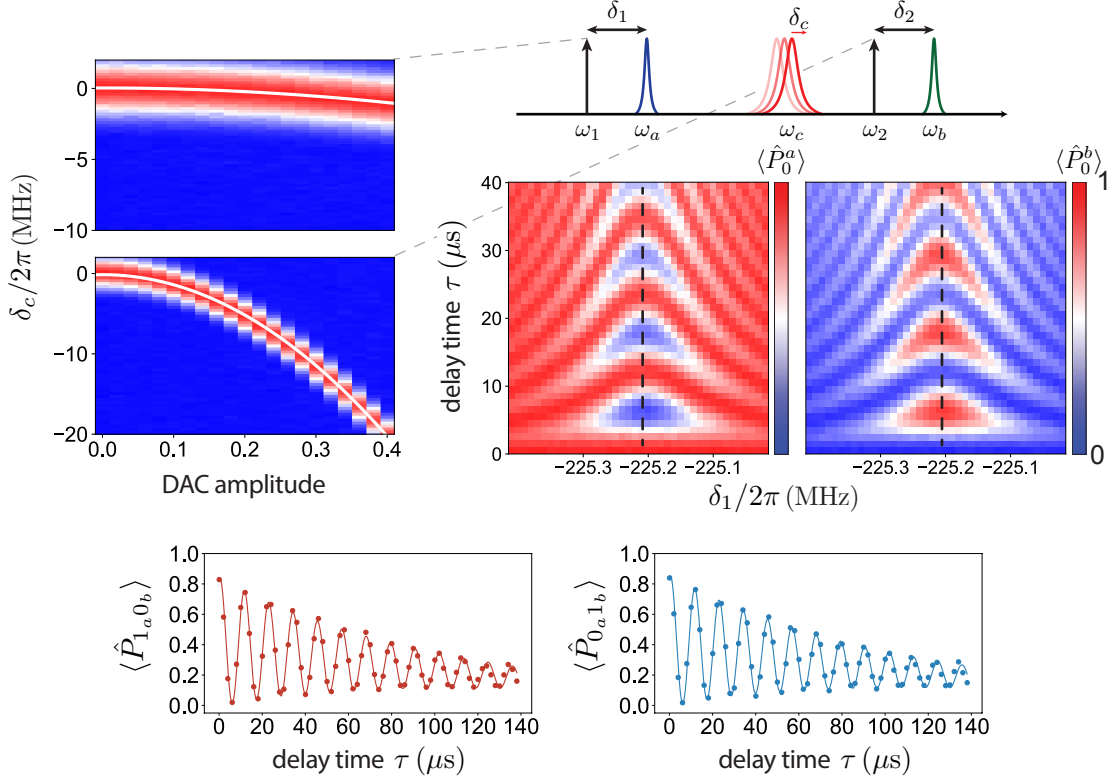
Figure 4.6 | Experimentally calibrating the beamsplitter. Stark shift measurements on the coupler transmon ω_c as a function of individual pumps detuned $\delta_2 = \delta_1 = 2\pi \times 225\,\text{MHz}$ from each cavity resonance. Solid lines are a fit to a quadratic function. A 2D scan of the lower pump frequency and delay time while keeping the upper pump fixed at $\delta_2 = 2\pi \times 225\,\text{MHz}$ and simultaneously measuring vacuum population in both cavities for an initial state $|0\rangle_a \otimes |1\rangle_b$. The bottom panel shows a linecut of the data at the resonance condition for initial states $|1\rangle_a \otimes |0\rangle_b$ (left) and $|0\rangle_a \otimes |1\rangle_b$ (right), fit to Eq. 4.16. From this, we extract $g_{\text{bs}} = 2\pi \times 44\,\text{kHz}$.

space as occuring from the contributions of an average cavity decay rate $\bar{\kappa} = (\kappa_a + \kappa_b)/2$ and a dephasing rate $\kappa_{\text{ph}}^{\text{bs}}$ arising from fluctuations in the resonance condition:

$$P_{10/01} = \frac{1}{2}\exp\big(-\bar{\kappa}(t - t_0)\big)\big(1 + \exp(-\kappa_{\text{ph}}^{\text{bs}}(t - t_0)/2)\cos(2g_{\text{bs}}(t - t_0))\big) \tag{4.16}$$

which is very useful for interrogating the contributions to the infidelity from decay and dephasing independently.

We have shown our approach to calibrating all of the Gaussian operations we need for implementing $\hat{U}_{\text{Dok}}$. How faithfully can we rely on these calibrations? In other words, is there any systematic bias that we should worry about? On one hand, our choice of
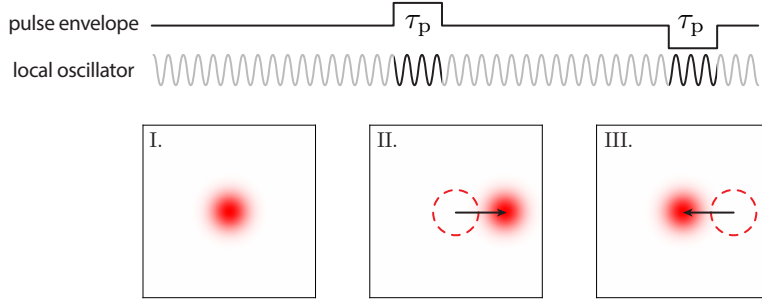
Figure 4.7 | Frame tracking: a single displacement. We consider a simple pulse sequence where the frequency of a local oscillator is tuned exactly on resonance with a cavity mode. A displacement pulse with duration τ_p displaces an initial vacuum state to a coherent state $|\alpha\rangle$. In the frame of the drive, $\hat{H} = 0$ when the drive is off, so the coherent state is stationary. A subsequent pulse with negative amplitude using the same local oscillator that displaces the coherent state back to the vacuum will do so for any arbitrary time after the initial pulse because the clock of the local oscillator keeps track of the phase. If the second pulse is performed using a separate local oscillator that is not synced to the primary one, the displacement phase will be random for every run of the experiment.

fitting photon number populations to an ideal distribution in the case of the displacement and single-mode squeezing neglects any decay during the operation itself is already an approximation that relies on $\kappa\tau_\mathrm{pulse} \ll 1$, where κ is the cavity decay rate. Furthermore, we probe photon number populations via selective π-pulses which means that our cavity states will undergo a finite amount of decay during the measurement, following closely the discussion of state preparation in section 3.3.4.1. This further biases our calibrations because we will be measuring the photon number distribution of a slightly smaller coherent or squeezed state compared to that immediately following the pulse. Again, this can largely be neglected if $\kappa\tau_\mathrm{meas} \ll 1$, but it is worth keeping in mind as one requires even higher fidelity operations in the future. A more faithful approach would be to fit the data to a full numerical simulation of the master equation. In practice, the bias is roughly on the order of $\mathcal{O}(\kappa\tau_\mathrm{meas})$ for $\kappa\tau_\mathrm{meas} \ll 1$.

4.3.3 Concatenating parametric processes: frame tracking

The target implementation of $\hat{U}_\mathrm{Dok}$ has a well defined phase relationship between the constituent operations. That is, the set of Doktorov parameters $\{\zeta_1, \zeta_2, \theta, \zeta_1', \zeta_2', \alpha_1, \alpha_2\}$ define a
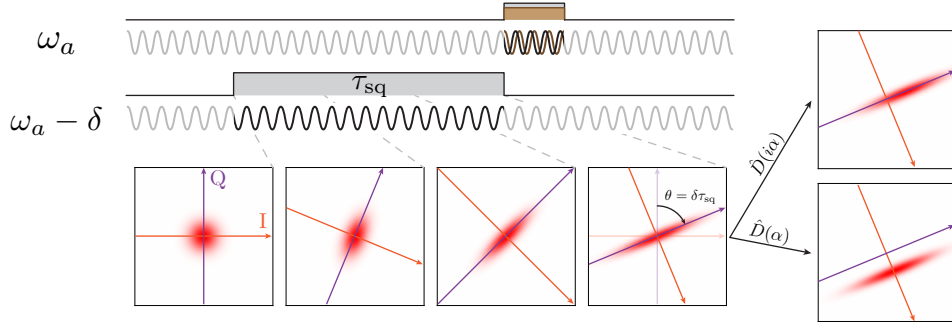
Figure 4.8 | Frame tracking: squeezing and displacement. We consider a scenario with two relevant frames: one at ω_a which is both the cavity frame and the drive frame, and one at $\omega_a - \delta$ which is the effective drive frame of the squeezing operation. The same microwave generator produces both signals and the pulse generation phases are synchronized. Enacting a squeezing operation along the in-quadrature axis ($\theta_{sq} = 0$) will create a squeezed state that is rotated in the frame of ω_a. Performing a subsequent displacement operation using the drive frame thus requires a phase $\theta_{disp} = \delta\tau_{sq}$ in addition to the desired phase of the operation, which requires I-Q control. In this example, we illustrate enacting the ideal operations $\hat{U} = \hat{D}(\alpha)\hat{S}(\zeta)$ or $\hat{D}(i\alpha)\hat{S}(\zeta)$ where $\alpha = \zeta = 1$.

unique $\hat{U}_{\mathrm{Dok}}$ and changing the phase of any of the parameters will result in implementing a different unitary. Fortunately, we have full phase control for all of our Gaussian operations based on the appropriate phase of combination of phases of our pumps. Unfortunately, the pump-induced Stark shifts become a real nuisance here as they cause additional operation-dependent phase space rotations of both cavity states. To understand the difficulty of properly accounting for the Stark shifts, we first take a moment to describe the basic relationship between drive phases and cavity phases.

Fig. 4.7 highlights the simplest case of a resonant drive on a cavity mode, where the microwave generator that creates the pulses serves as a clock for the entire sequence. While the phase of an initial displacement for every run of an experiment will be random, the phase relationship between the phase of an initial pulse and every subsequent pulse is fixed. Thus, the cavity phase is defined by the phase of the first operation.

To illustrate and expand on this concept for multiple operations, we consider concatenating a squeezing operation with a displacement (Fig. 4.8). We first assume that we have calibrated a squeezing operation and adjusted the pump frequencies such that there is no
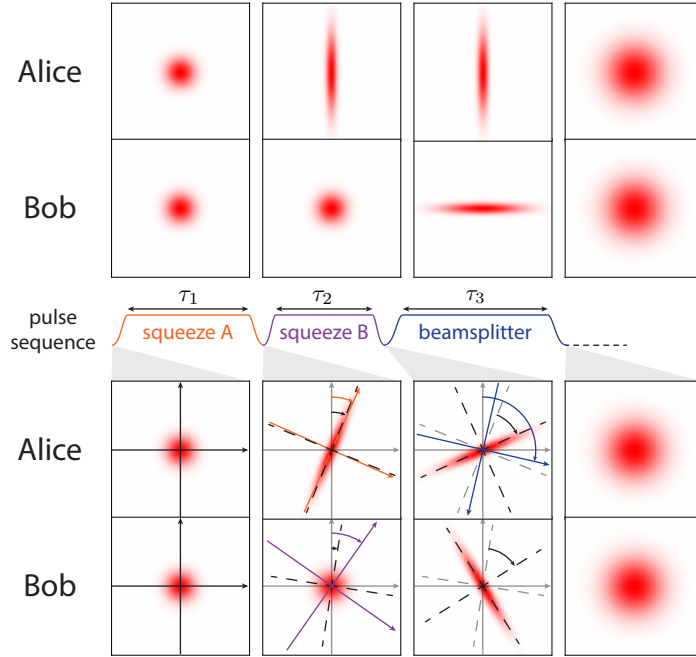
Figure 4.9 | Frame tracking: two modes. Top: ideal state evolution under the first three operations in $\hat{U}_{\mathrm{Dok}}$: $\left(\hat{U} = \hat{R}(\theta = \pi/4)\hat{S}_2(\zeta_2 = -1)\hat{S}_1(\zeta_1 = 1)\right)$ as shown via reduced Wigner functions of Alice and Bob. Here, the beamsplitter acting on two orthogonal squeezed states produces an entangled two-mode squeezed state, which loses all features when looking at individual cavity Wigner functions. Bottom: state evolution in the frame of the bare cavities. Dashed axes refer to the cavity phase, whereas the solid axes depict the frame of the operation. Initially, all operation frames can be taken to be aligned in the $x - y$ plane. The operation frames advance based on the total time elapsed since $t = 0$. The cavity phases advance based on the Stark shift on each mode, which slightly differ from the operation frames due to finite ramp times. The beamsplitter frame is that of the difference between the Stark shifts of both cavities.

Stark shift in the frame of the drive:

$$\hat{H}_{\mathrm{sq}}/\hbar = g_{\mathrm{sq}}(e^{i\theta_{\mathrm{sq}}}\hat{a}^2 + e^{-i\theta_{\mathrm{sq}}}\hat{a}^{\dagger 2}) \tag{4.17}$$

but there is a Stark shift δ with respect to the static cavity frame at ω_a. Enacting a squeezing operation thus puts a phase on the cavity state relative to its static frame that depends on the Stark shift and elapsed time. A subsequent displacement operation thus needs to know this accumulated phase in order to displace along the appropriate axis.

Now we can see how this problem gets rather complicated for multiple operations on multiple modes. Each operation will have its own frame as defined by the drive frequencies

	squeeze A	squeeze B	beamsplitter
Alice	42.6	45.5	260
Bob	21.4	47.3	36.6

Table 4.2 | **Pump-induced cavity Stark shifts.** All rates are in kHz. The operation frame rate is equivalent to the Stark shift on each respective cavity for squeezing, whereas it is the difference of the Stark shifts for the beamsplitter.

and will induce *different* Stark shifts on *all* the modes of the system. In order to implement different target Doktorov transformations without having to perform any recalibrations, we need to determine all of these rates and compile our pulse sequences to automatically take care of the frame tracking. A visual aid for implementing a portion of the two-mode Doktorov transformation is provided in Fig. 4.9. Compactly, the proper phase to apply for the kth operation with respect to the bare cavity frames is:

$$\varphi_k = \varphi_{\text{desired}} + \eta_k \left(\delta_{\text{op}} T - \sum_{j<k} (\delta_j \tau_j + \varphi_j^{\text{ofs}}) \right) \tag{4.18}$$

where $\eta_k = 1(2)$ for a beamsplitter (squeezing) operation and we in practice apply this phase to one of the sidebands. Here, T is the *total* time elapsed since the beginning of the entire sequence and δ_{op} is the frequency difference between the operation frame and bare cavity frame. The sum $\{j\}$ is over all previously applied operations where δ_j is the relevant cavity phase acquired during each operation lasting for time τ_j (excluding the ramp time) and φ_j^{ofs} is an offset phase acquired during the ramp time. The complete set of rates is given in Table 4.2. Finally, φ_{desired} is determined by the appropriate phase to translate $\hat{U} = e^{-i\hat{H}_k \tau_k / \hbar}$ into either $\hat{S}(\zeta)$ or $\hat{R}(\theta)$.

4.3.4 Detection schemes

After we have successfully created the state $\hat{U}_{\text{Dok}} |\psi_0\rangle$, the task is now to sample from the joint photon number distribution. Before implementing any measurement techniques, we first measure the state of all three transmons and discard any instances where any of the transmons are measured to be in their excited state (Fig 4.4). This serves two purposes. First, a heating event of any of the three transmons to their excited state during $\hat{U}_{\text{Dok}}$ will lead to an error, since the dispersive interaction shifts the resonance frequency of the cavity
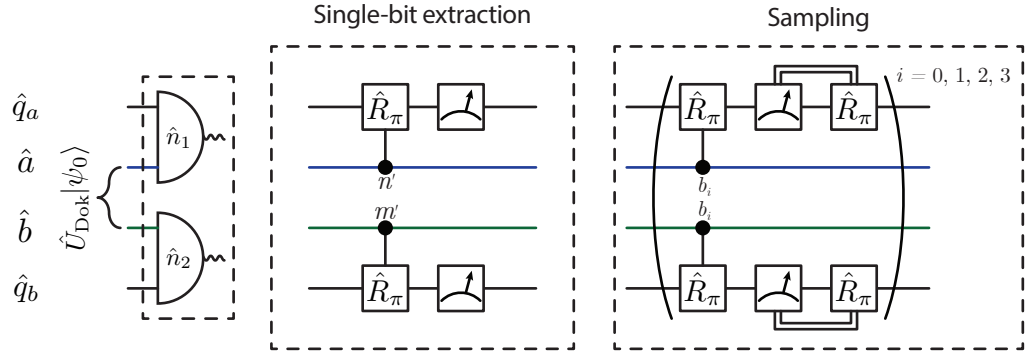
Figure 4.10 | Detection schemes. We consider two methods to measure the photon number distribution across both cavity modes. *Single-bit extraction*: On a single run of the experiment, simultaneous selective π pulses are performed on the ancilla transmons conditioned on the state $|n', m'\rangle$ in the cavities. *Multiphoton sampling*: On a single run of the experiment, sequential QND measurements are performed simultaneously on each cavity to extract a sample from the joint photon number distribution.

and thus dephases a pumped operation. Second, we are able to eliminate errors in the measurement protocol since they will rely on the ancilla transmons starting in their ground state. While this technique is not scalable, it provides a useful diagnostic to ensure that our simulator works as expected when known errors are suppressed.

We describe two detection schemes: *single-bit extraction*, which samples from one state in the joint Hilbert space per run of the experiment and extracts a single bit of information, and *multiphoton sampling,* which directly obtains a sample from the joint photon number distribution per run of the experiment. The former is not scalable as it requires querying an exponentially growing Hilbert space, whereas the latter completely collapses this cost into an $\mathcal{O}(1)$ measurement.

4.3.4.1   Single-bit extraction: selective pulses

We first introduced the selective π-pulse in section 3.3.2.2 as a transmon rotation conditioned on there being a certain number of photons n in the cavity. In section 3.3.4, we expanded on this by viewing a selective π-pulse as implementing the POVM elements $\{\hat{M}_g = \hat{1} - |n\rangle\langle n|, \hat{M}_e = |n\rangle\langle n|\}$ on the cavity Hilbert space. Here, we generalize this for an arbitrary number of cavity modes N and consider simultaneous but individual measurements of each cavity via selective π-pulses conditioned on photon numbers $\{n', m', ...\}$

across all modes. The resulting POVM elements on the cavity can be written as $\{\hat{M}_{\bar{\mathbf{e}}} = \hat{\mathbf{1}} - |n', m', ...\rangle \langle n', m', ...|, \hat{M}_{\mathbf{e}} = |n', m', ...\rangle \langle n', m', ...|\}$ where we have correlated all the individual measurement outcomes. For our experiment where $N = 2$, the pulses perform the following mapping:

$$\sum_{i,j} c_{ij} |i, j\rangle \otimes |g, g\rangle \rightarrow \sum_{i \neq n', j \neq m'} c_{ij} |i, j\rangle \otimes |g, g\rangle$$
$$+ \sum_{i \neq n'} c_{im'} |i, m'\rangle \otimes |g, e\rangle + \sum_{j \neq m'} c_{n'j} |n', j\rangle \otimes |e, g\rangle$$
$$+ c_{n'm'} |n', m'\rangle \otimes |e, e\rangle \tag{4.19}$$

where we are ultimately trying to measure $\{|c_{n',m'}|^2\}$.

As we mentioned previously, extracting FCFs using the single-bit extraction scheme is not scalable[1]. The bosonic Hilbert space grows exponentially as $n_{\max}^N$, where $n_{\max}$ is the maximum number of Fock states considered for each mode. Nevertheless, the single-bit extraction technique is useful for benchmarking the performance of our simulator. In fact, we can go one step further and perform a form of error mitigation on the final distribution that accounts for measurement imperfections. Specifically, decay and heating events during selective π-pulses and readout errors result in a systematic bias in the final estimate of the photon number population.

For the case of a single ancilla transmon coupled to a cavity, these effects result in a reduction of contrast for a Rabi experiment when both the ancilla and the cavity are prepared in their ground state (recall Fig. 3.9). When using this pulse to infer cavity photon number populations, we assume that there is no photon number dependence to either the Rabi or decoherence rates of the ancilla. Under this model, we can relate the measured probabilities $\vec{Q}$ to the true probabilities $\vec{P}$ via:

$$\vec{P} = \frac{\vec{Q} - f}{t - f} \tag{4.20}$$

---

1. We do note that since individual selective pulses are QND, there is still information left over in the cavity state for further interrogation with additional selective pulses, for instance as described in [Peropadre et al. 2016].

where f and t are the probabilities of assigning the ancilla measurement to the excited state when it is prepared in the ground and excited states, respectively. Thus, inferring the true probabilities from the measured probabilities is a relatively straightforward task.

For two modes, however, the problem becomes more complicated as a measurement of a joint probability relies on shot-by-shot correlations of the individual ancilla outcomes. Thus, false positive counts due to heating and readout errors lead to misassignment in a nonlinear fashion. We can again write what a given joint measured probability Q_{nm} is in terms of the true distribution P_{nm}:

$$Q_{nm} = t_A t_B P_{nm} + t_A f_B P_{n\bar{m}} + f_A t_B P_{\bar{n}m} + f_A f_B P_{\bar{n}\bar{m}} \tag{4.21}$$

This equation may be solved for P_{nm} by noting that:

$$P_{\bar{n}m} = \sum_k (1 - \delta_{nk}) P_{km}$$

$$P_{n\bar{m}} = \sum_l (1 - \delta_{lm}) P_{nl}$$

$$P_{\bar{n}\bar{m}} = 1 - P_{nm} \tag{4.22}$$

It is worth noting that this requires Q_{nm} to be a square matrix, which translates to measuring both n' and m' up to a pre-specified $n_{\max}$.

4.3.4.2 Multiphoton sampling: implementing a number-resolved photodetector

We described the theory behind implementing a QND number-resolved detector of a cavity using a dispersively coupled ancilla qubit in section 3.3.4.2. To recap, we rely on performing sequential QND readouts of generalized parity operators that, when concatenated, implement cavity POVM elements that are single Fock states (modulo $n_{\max}$).

As we saw previously in section 3.3.4, the dispersive interaction lends itself to a natural way to measure the parity operator, whose eigenvalues are equivalent to the least significant bit in the binary decomposition. In principle, the dispersive interaction can be used further to iteratively measure the next significant bit by keeping track of the result of the first bit and
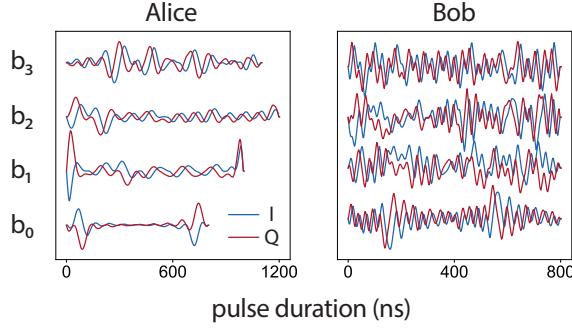
Figure 4.11 | **Optimal control pulses for binary measurement.** Only drives on the transmon are necessary for mapping the generalized parity operators in Eq. 3.54 onto the state of the transmon. For Alice, the pulse shape for measuring the parity resembles that of a standard parity measurement given that the pulse time $\tau_p = 800$ ns is approximately the parity time $\pi/\chi_a \approx 666$ ns. For Bob, the parity time is actually much shorter $\pi/\chi_b \approx 400$ ns, suggesting that the pulses could have been further shortened and may explain the more erratic shapes.

waiting an appropriate fraction of π/χ [Dassonneville et al. 2020]. This approach, while conceptually simple, has a few drawbacks. First, higher-order terms in the Hamiltonian such as χ' result in errors under this approach for larger photon number distributions. Second, the errors for the scheme are not independent and are correlated from bit to bit, potentially complicated any error mitigation techniques.

An alternative approach is to use optimal control pulses as introduced in section 3.3.2.3 to measure each bit *independently* while resetting the transmon in between rounds (Fig. 4.10). This has the nice feature in that only drives on the transmon are necessary, thus aiding in the QND-ness with respect to the cavity state. Furthermore, resetting the transmon between rounds enables a Hidden Markov Model approach to mitigating errors [Curtis et al. 2021]. The pulses generated and used for multiphoton sampling in this experiment is shown in Fig. 4.11.

4.3.5 Franck-Condon factors of photoelectron spectra

Here, we present results on integrating all of the previously described components to implement sampling of Franck-Condon factors for various photoelectron processes. Our simulator has two cavity modes, which limits us to simulating molecules that have two vibrational modes that actively couple during an electronic transition. For this reason, we

Molecular photoelectron process	$\tilde{\nu}_{\text{stretch}}$ (cm^{-1})	$\tilde{\nu}_{\text{bend}}$ (cm^{-1})	$\tilde{\nu}'_{\text{stretch}}$ (cm^{-1})	$\tilde{\nu}'_{\text{bend}}$ (cm^{-1})	θ (deg)	$\mathbf{K}$ $(a_0\sqrt{m_e})$
$\text{H}_2\text{O} \xrightarrow{h\nu} \text{H}_2\text{O}^+(\tilde{B}^2\text{B}_2) + e^-$	3830.91	1649.27	2619.09	1602.85	-0.16598	$(5.05, 49.47)$
$\text{O}_3^- \xrightarrow{h\nu} \text{O}_3 + e^-$	1031.10	582.58	1147.04	713.39	-0.0417	$(27.36, 14.33)$
$\text{NO}_2^- \xrightarrow{h\nu} \text{NO}_2 + e^-$	1297.27	783.55	2633.34	796.94	2.40146	$(35.67, -38.01)$
$\text{SO}_2 \xrightarrow{h\nu} \text{SO}_2^+ + e^-$	1136.38	506.27	1056.79	396.11	0.19012	$(-8.86, -58.34)$

Table 4.3 | Theoretically optimized molecular parameters. Vibrational frequencies for the symmetric-stretching and bending modes of each molecule in pre-($\tilde{\nu}$) and post-transition ($\tilde{\nu}'$) states are provided in wavenumbers (cm^{-1}), which is related to angular frequency ω via $\tilde{\nu} = \omega/2\pi c$, where c is the speed of light. The rotation angle corresponding to the Duschinsky rotation matrix is defined in Eq. 4.24. The shift vector $\mathbf{K} = (k_1, k_2)$ is provided in mass weighted normal coordinates (where a_0 is the Bohr radius and m_e is the electron mass) and reflects the relative displacement of equilibrium geometries between the two molecular configurations.

consider photoionization and photodetachment processes of symmetric triatomic molecules that maintain C_{2v} symmetry in both electronic states of interest. As such, the asymmetric stretching mode remains decoupled throughout the transition and we only need to consider the transformation between the symmetric stretching and bending modes.

Molecular parameters, which are then translated to Doktorov parameters, are obtained via classical electronic structure calculations. For this, we employ the commercial (G16 rev. A.03) version of the GAUSSIAN quantum-chemical suite [Frisch et al. 2016] to obtain optimized equilibrium geometries with imposed C_{2v} symmetry constraints for the triatomics that we consider for our experiment. This provides the normal-mode vibrational frequencies, Duschinsky rotation matrices, and shift vectors, which are compiled in Table 4.3. All analyses relied on the CCSD(T) coupled-cluster paradigm, which includes single and double excitations along with non-iterative correction for triples. We used Dunning's correlation-consistent basis sets [Dunning Jr 1989; Kendall, Dunning Jr, and Harrison 1992; Woon and Dunning Jr 1993] of triple-ζ quality augmented by supplementary diffuse functions (aug-cc-pVTZ $\equiv$ apVTZ) were deployed for all targeted molecules except water, where a larger doubly augmented, quadruple-ζ basis was employed (daug-cc-pVQZ $\equiv$ dapVQZ). These basis sets are very complete for the simple molecules considered here and result in very accurate calculations as described in section 2.2.1. These calculations obtain the electronic ground state for all species, with the exception of the $(\tilde{B}^2\text{B}_2)$ excited state of the water

	$H_2O \xrightarrow{h\nu}$ $H_2O^+(\tilde{B}^2B_2) + e^-$	$O_3^- \xrightarrow{h\nu}$ $O_3 + e^-$	$NO_2^- \xrightarrow{h\nu}$ $NO_2 + e^-$	$SO_2 \xrightarrow{h\nu}$ $SO_2^+ + e^-$
ζ_1	0.262	0.104	0.035	0.242
ζ_2	-0.160	-0.181	-0.217	-0.162
θ	-0.166	-0.042	2.402	0.19
ζ_1'	0.072	0.157	0.389	0.206
ζ_2'	-0.174	-0.080	-0.208	-0.285
α_1	-1.0162	-1.4278	0.0546	-0.1140
α_2	-2.8977	-0.5311	-2.2207	1.7713
η	47.6381	28.9364	34.7639	26.4676

Table 4.4 | Converting molecular parameters to dimensionless Doktorov parameters. All values are truncated to the precision that the operations are able to be implemented experimentally.

cation.

One technicality to mention is that the Duschinsky rotation matrices and associated shift vectors provided by GAUSSIAN are defined via:

$$\mathbf{Q}' = \mathbf{J}\mathbf{Q}'' + \mathbf{K} \tag{4.23}$$

where $\mathbf{Q}'$ and $\mathbf{Q}''$ are mass-weighted normal coordinates of the pre- and post-transition molecular configurations, respectively. Because our simulation considers the transformation from a vibrational state in the pre-transition configuration to the post-transition configuration, we must redefine the Duschinsky rotation matrices and associated shift vectors accordingly:

$$U = \begin{pmatrix} \cos\theta & -\sin\theta \\ \sin\theta & \cos\theta \end{pmatrix} = \mathbf{J}^T \tag{4.24}$$

$$\mathbf{d} = -\mathbf{J}^T\mathbf{K} \tag{4.25}$$

The final list of Doktorov parameters used in our experiment is given in Table 4.4.

The results for two of the photoelectron processes are shown in Fig. 4.12. Additional data for the other processes listed in Table 4.3 can be found in the Supplementary Infor-
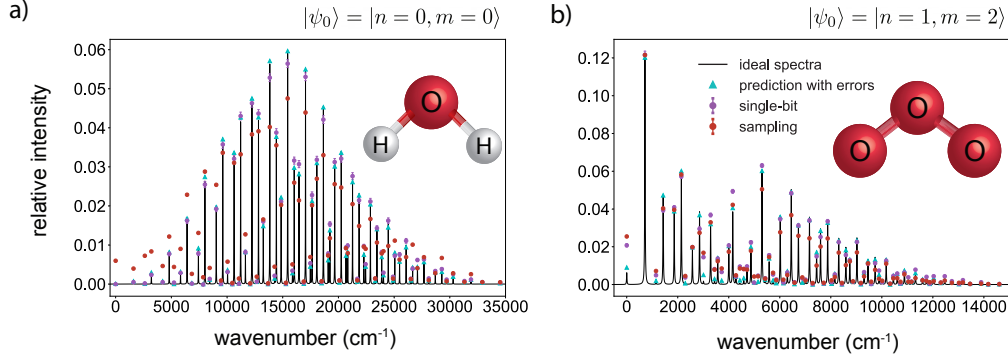
Figure 4.12 | **Experimentally measured Franck-Condon factors.** Highlighted are (a) photoionization of water to the $(\tilde{B}^2B_2)$ excited state of the cation $H_2O \xrightarrow{h\nu} H_2O^+(\tilde{B}^2B_2)$ + e^- starting in the vacuum (vibrationless, $n = 0$, $m = 0$) state and (b) the photode-tachment of the ozone anion to the ground state of the neutral species $O_3^- \xrightarrow{h\nu} O_3 + e^-$ starting from a vibrational eigenstate possessing one quantum of symmetric-stretching and two quanta of bending excitation ($n = 1$, $m = 2$). The abscissa scale corresponds to vi-brational term values (energies in cm^{-1}) within the final (post-transition) electronic PES calculated from the harmonic frequencies for symmetric-stretching and bending degrees of freedom: $\tilde{\nu} = n'\tilde{\nu}'_{\text{stretch}} + m'\tilde{\nu}'_{\text{bend}}$. Solid lines depict theoretical FCFs, artificially broadened with Lorentzian profiles (10 cm^{-1} FWHM). Circles represent experimental data using the *single-bit extraction* (purple) and *multiphoton sampling* (red) measurement schemes; statis-tical error bars for the latter measurement are not visible on this scale. Systematic errors associated with transmon decoherence during the selective π pulses are corrected for as described in section 4.3.4.1. Additional errors are present in the sampled values, owing to decoherence effects during the binary decomposition measurement chain. Cyan triangles refer to expected FCFs under errors due to photon loss and self-Kerr of the cavities.

mation of [Wang et al. 2020]. For the single-bit extraction measurement, the probability distribution and associated standard errors are obtained via:

$$q^{\text{meas}}_{n',m'} = \frac{n^{ee}_{n',m'}}{N^{\text{runs}}_{n',m'}} \tag{4.26}$$

$$\sigma_{n',m'} = \sqrt{\frac{q^{\text{meas}}_{n',m'}(1 - q^{\text{meas}}_{n',m'})}{N^{\text{runs}}_{n',m'}}} \tag{4.27}$$

where $n^{ee}_{n',m'}$ is the number of counts where both ancillas are measured in their excited state, indicating a measure for population in $|n', m'\rangle$, and $N^{\text{runs}}_{n',m'}$ is the total number of runs of the experiment for probing $|n', m'\rangle$. The number of runs varies slightly among different final states due to varying post-selection probabilities. The correction protocol outlined in section 4.3.4.1 is then applied to $q^{\text{meas}}_{n',m'}$ to retrieve a new probability distribution $p^{\text{meas}}_{n',m'}$.

The standard error $\sigma_{n',m'}$ is truncated to one significant digit and $p_{n',m'}^{\mathrm{meas}}$ is then rounded to the precision set by $\sigma_{n',m'}$. The data reported is $p_{n',m'}^{\mathrm{meas}} \pm \sigma_{n',m'}$ only for probabilities with significant support relative to the precision of the experiment ($p_{n',m'}^{\mathrm{ideal}} \geq 10^{-4}$).

The same method (sans the correction protocol) is applied to the data for the sampling measurement, except there the probabilities and standard error are given by:

$$p_{n',m'}^{\mathrm{meas}} = \frac{n_{n',m'}}{N_{\mathrm{runs}}} \tag{4.28}$$

$$\sigma_{n',m'} = \sqrt{\frac{q_{n',m'}^{\mathrm{meas}}(1 - p_{n',m'}^{\mathrm{meas}})}{N_{\mathrm{runs}}}} \tag{4.29}$$

where $n_{n',m'}$ is the number of times the joint photon number $|n',m'\rangle$ is sampled from the total number of runs of the experiment N_{runs}.

A figure of merit for quantifying the quality of the quantum simulation is the distance $D = \frac{1}{2} \sum_{i=0}^{n_{\max}} \sum_{j=0}^{n_{\max}} |p_{ij}^{\mathrm{meas}} - p_{ij}^{\mathrm{ideal}}|$ between the measured probabilities $\{p_{ij}^{\mathrm{meas}}\}$ and the ideal distribution $\{p_{ij}^{\mathrm{ideal}}\}$. The distances for the two simulated processes are $D = 0.049$ (H_2O) and 0.105 (O_3) for the single-bit extraction scheme and $D = 0.152$ (H_2O) and 0.148 (O_3) for the sampling scheme. The sampling distance will ultimately be the relevant figure of merit for evaluating the practical performance of this approach as it is scaled up. The other relevant metric is run time. As previously discussed in section 4.3.4.1 the single-bit extraction scheme requires a factor of $n_{\max}^N$ more runs compared to the sampling scheme for a desired statistical error. Our experiment operates at an effective repetition rate of roughly $\sim$300 Hz, thus requiring $\sim$7 hours versus $\sim$100 seconds of data acquisition, respectively, for $\sim 3 \times 10^4$ samples of the photoionization of water.

Furthemore, these distance metrics are accompanied with a success probability due to post-selection of transmon heating events, which are 95% and 93% for the aforementioned simulations. The heating events are dominated by the coupler transmon; the dynamics of a driven Josephson element for engineered bilinear operations presents a multi-dimensional optimization problem that seeks to maximize the desired interaction rates while minimizing induced decoherence and dissipation rates [Zhang et al. 2019].

The errors that are undetected by post-selection include cavity self-Kerr, photon loss,

Cavity	Operation	$K/2\pi$ (kHz)	T_1 (μs)
Alice	native	1.8	280
	squeezing	2	200
	beamsplitter	30	170
Bob	native	3.2	320
	squeezing	1.9	280
	beamsplitter	5	170

Table 4.5 | **Estimated self-Kerr and T_1 values.** The beamsplitter decay rates are extracted from the fit performed in the calibration of the operation in Fig. 4.6 assuming that $\kappa_A^{\mathrm{BS}} = \kappa_B^{\mathrm{BS}} = \bar{\kappa}$.

and imperfect state preparation. We measure the self-Kerr and decay rates of each cavity *in the presence* of each operation and compile the results in Table 4.5. We use these values to perform a full time-domain master equation simulation of our implementation to estimate what fidelity we should expect in the absence of additional calibration and systematic errors. The total infidelity depends on the molecular process; each corresponding Doktorov transformation will have different squeezing and rotation parameters thus leading to varying lengths of the pumped operations. Simulations of shorter length circuits will therefore have lower error rates. Additionally, errors due to self-Kerr interactions of the cavities are larger for higher photon number states.

4.4 Resource requirements and scalability

4.4.1 Classical methods

To properly contextualize the efficiency of the FC algorithm, it is useful to consider state-of-the-art computational methods for calculating Franck-Condon factors using classical computers. A pervasive and representative approach is one that utilizes generating functions to compute a single Franck-Condon overlap integral $\langle n_1, n_2, ..., n_N | \psi_0 \rangle$ in terms of other integrals with fewer occupations $\{\langle n_1 - i_1, n_2 - i_2, ..., n_N - i_N | \psi_0 \rangle\}$. This can be compactly represented through a recursion relation [Sharp and Rosenstock 1964; Ruhoff 1994] which means that the total number of necessary integrals to compute a Franck-Condon factor with

a total number of quanta $M = \sum_{i=1}^{N} n_i$ over N modes is [Dierksen and Grimme 2005]:

$$\binom{N + M - 1}{M} \tag{4.30}$$

Therefore, the formal task of obtaining the full Franck-Condon profile, which by itself contains an exponential number of entries corresponding to the size of the Hilbert space $n_{\max}^N$, can be seen to be at least exponentially challenging.

In practice, however, electronic spectra of many polyatomic molecules initially cooled to near their rovibronic ground states typically exhibit vibronic progressions confined to a small region in the vibrational Hilbert space. This stems primarily from two effects. First, a single electronic transition in large molecules typically does not induce large shifts of the equilibrium coordinates for *a significant fraction* of all the normal modes, which keeps $n_{\max}$ for most modes relatively low. Second, following symmetry considerations, there typically is structure in the Duschinsky rotation matrix which allows it to be approximated as block-diagonal [Dierksen and Grimme 2005]. This is significant because each block-diagonal subspace can be treated independently as they do not couple to the remaining vibrational degrees of freedom of the molecule. This effectively reduces the dimensionality of the problem from N to several sub-problems with dimensionality of each block. In the limit where no mode-mixing occurs, i.e. $U = \mathbf{1}$, the full multimode Franck-Condon integrals can be easily and efficiently computed via the product of all single-mode Franck-Condon integrals.

Consequently, classical methods can implement convergence criteria that can provide a trade-off between accuracy and computational resources [Barone, Bloino, and Biczysko 2009]. In cases where the Duschinsky rotation matrix can not be well approximated as block-diagonal, however, recursive methods inevitably need to explore the entire Hilbert space and therefore become intractable for large system sizes. The advantage of using a quantum simulator that samples from the full distribution would then be to quickly identify the relevant FCFs with large weights, for which a classical computation can then be done for the specific FCFs of interest. Thus, the utility of the quantum simulator for obtaining

Franck-Condon factors in large polyatomic molecules will depend on the configurational details for each electronic transition on a case-by-case basis. Finally, we highlight a recently developed classical algorithm for computing molecular vibronic spectra for Gaussian input states via Fourier transforms, further suggesting a separation between Gaussian and non-Gaussian boson sampling when it comes to computational complexity [Oh et al. 2022].

4.4.2 Comparing a bosonic vs. qubit processor

The central advantages of simulating the transformation of a bosonic Hamiltonian using a bosonic system lie in both the native encoding and the efficient decomposition of the Doktorov transformation into Gaussian operations. Alternatively, one can estimate Franck-Condon factors using a qubit-based algorithm [Sawaya and Huh 2019], which needs a corresponding boson-to-qubit mapping. This requires encoding the Hilbert space of size $n_{\max}^N$ onto $n_q = N\log_2(n_{\max})$ qubits. The choice of $n_{\max}$ is dependent on the initial state as well as the magnitude of the displacement and squeezing; both operations can produce states with large photon numbers. Using quantum signal processing [Low and Chuang 2017], the approximate number of gates n_g then needed to implement $\hat{U}_{\mathrm{Dok}}$ using a universal qubit gate set to within an error ε is $n_g = O(N^2 n_{\max}^2 \log^3(1/\varepsilon))$. For our experiment with $N = 2$ modes, taking $n_{\max} = 16$ and desiring an error $\varepsilon = 5 \times 10^{-2}$, this translates to $n_q = 8$ qubits and $n_g = O(10^3)$ gates. The coherence requirements for performing such a computation this way is thus relatively demanding and exceeds the capabilities of current technologies, where we do not yet have fault tolerant quantum processors. By comparison, our native bosonic simulator containing N modes simply requires $2N$ squeezing operations, N displacement operations, and a maximum of $N(N-1)/2$ beamsplitter operations in a linear array of nearest-neighbor coupled modes. This translates to a total of $O(N^2)$ operations and a corresponding circuit depth of $O(N)$ when non-overlapping beamsplitters are applied simultaneously. An advantage of the qubit-based algorithms, however, is the ability to systematically incorporate anharmonicities in the PES, a task which still needs to be theoretically investigated for the bosonic implementation.

4.4.3 Scalability and error budget

As shown in Fig. 4.2, a linear array of bosonic memories with nearest neighbor coupling is sufficient for scaling to larger system sizes. In our architecture of fixed frequency cavity modes, the bilinear Gaussian operations are enacted via robust frequency converting four-wave mixing processes that can use pump frequency tuning to obviate the need for any in-situ frequency tuning of the resonators.

As the hardware is scaled up, the fidelity of the individual operations will determine the fidelity of the overall simulation. Though different photoelectron processes will have different errors, we can consider a simplified model for quantifying performance with system size. We associate a success probability for each operation $\{\rho_i\}$ where the index i encompasses state preparation (SP), displacements (D), squeezing (SQ), beamsplitters (BS), and measurements (M). For simplicity we assume a uniform probability for each operation across all modes. We then specify a target success probability threshold ρ_{th} that reflects the accuracy of the full simulation. The number of modes that can be accurately simulated for a given ρ_{th}, therefore, can be determined by:

$$\rho_{\mathrm{SP}}^{N}\rho_{\mathrm{SQ}}^{2N}\rho_{\mathrm{D}}^{N}\rho_{\mathrm{BS}}^{N(N-1)/2}\rho_{\mathrm{M}}^{N} > \rho_{th} \tag{4.31}$$

Each of these probabilities can be taken to be the average fidelity of each operation across a representative set of Doktorov transformations. Taking the expected bounds on the error rates of the operations due to photon loss in our experiment, while assuming a measurement error rate of 10^{-2} and targeting $\rho_{th} = 0.5$, we get $N \approx 5$. Modest improvements in cavity lifetimes and further circuit optimization for engineering the bilinear interactions [Zhang et al. 2019] can reduce the error rate of the squeezing and beamsplitter operations to 10^{-3}, which increases the number of modes to $N \approx 25$. Beyond this, further reduction of the error rates or implementing bosonic error correction protocols that preserve bosonic statistics at the logical level [Noh, Girvin, and Jiang 2020] will be required for maintaining performance with increasing system size.

Chapter 5

Dissipative quantum dynamics through an engineered conical intersection

Our implementation of the FC algorithm in Chapter 4 was nice in the sense that we were able to both leverage the hardware efficiency of our bosonic simulator and develop a novel detection scheme that enabled the scalable implementation of a quantum simulation task with practical relevance. The FC algorithm, however, has limited quantitative application for realistic systems given that it considers unitary vibrational dynamics under the harmonic and adiabatic Born-Oppenheimer approximations. Modeling more realistic molecular dynamics requires incorporating additional capabilities that go beyond these simplifying assumptions. Motivated by this, we draw inspiration from a prominent photochemical reaction in nature — the *cis-trans* isomerization reaction in rhodopsin — which is central to vision. We develop a simple model for studying this reaction and experimentally incorporate two features that account for more realistic dynamics: strong electron-nuclei coupling where the Born-Oppenheimer approximation breaks down and ro-vibrational dissipation [Wang et al. 2022].

5.1 A simple model of a photochemical reaction that enables vision

Rhodopsin is a complex which consists of a primary opsin protein and a cofactor called retinal. Retinal ($C_{20}H_{28}O$, a form of vitamin A) is the chromophore of rhodopsin, meaning that it is the portion of the molecule responsible for absorbing visible light and, among other consequences, determines what color a molecule is.

The dynamics of retinal after absorbing light forms the basis for vision. There are two relevant isomers of retinal, which refers to different forms of a molecule that retain the same chemical composition but are structurally distinct: *11-cis* (referring to a rotation of a double carbon bond of the 11th carbon atom) and *all-trans*. Upon absorbing light, retinal undergoes an isomerization reaction from the ground reactant 11-cis towards the all-trans product (Fig. 5.1). The potential energy landscape of the two relevant electronic states contain a *conical intersection* (CI) where the two surfaces cross. Thus, an initial wave-packet that gets excited to the upper potential energy surface is able to rapidly progress through the conical intersection and towards the *all-trans* product within approximately 200 fs. The quantum yield of this reaction, which roughly quantifies the probability that the wave-packet arrives at the product configuration, is remarkably high ($\sim$60%) [Polli et al. 2010].

We can put on a physicist's hat and construct a simple model that captures the qualitative features of this reaction. At the heart of this system is the conical intersection, which is defined as a degeneracy of a two-dimensional electronic subspace with a crossing that occurs as a function of at minimum two internuclear coordinates [Teller 1937]. Following the considerations of section 2.1.3, this degeneracy suggests that an adiabatic electronic basis is not well suited for treating the system. Instead, we use a diabatic basis of two electronic states $\{|\psi_1\rangle, |\psi_2\rangle\}$ coupled to two generalized rovibrational modes $\{\hat{a}, \hat{b}\}$ under a linear vibronic coupling (LVC) model as a first order expansion of Eq. 2.22:

$$\hat{H}_{\text{LVC}}/\hbar = \Delta_a \hat{a}^\dagger \hat{a} + \Delta_b \hat{b}^\dagger \hat{b} + g_x \hat{\sigma}_x(\hat{a} + \hat{a}^\dagger) + g_y \hat{\sigma}_y(\hat{b} + \hat{b}^\dagger) \tag{5.1}$$
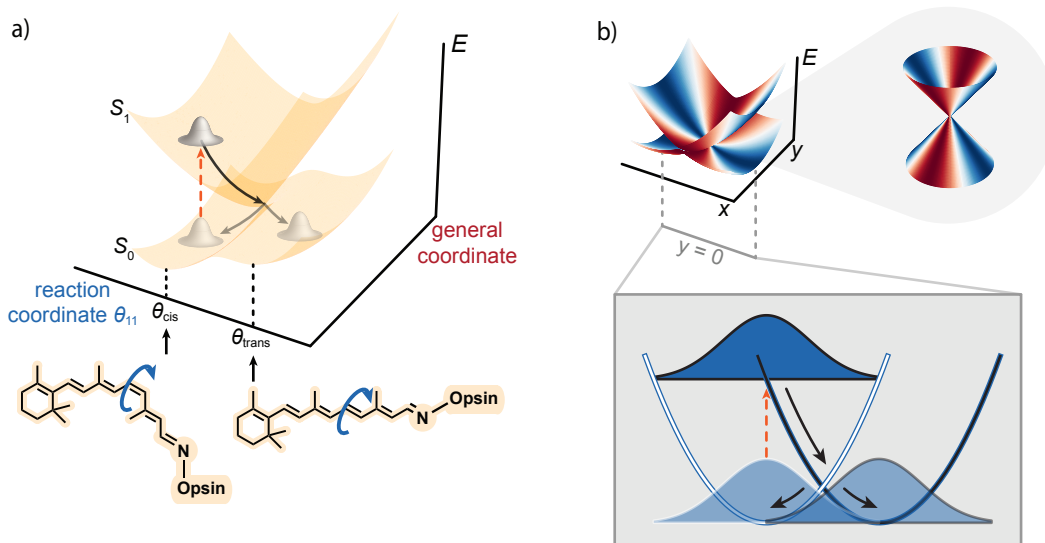
Figure 5.1 | **Modeling the *cis-trans* isomerization reaction in rhodopsin.** a) A ground state wave-packet becomes optically excited (dashed orange arrow) onto the upper potential energy surface S_1 in the Franck-Condon region. It rapidly evolves towards a conical intersection (CI), where it proceeds to branch either back to its reactant 11-cis configuration or towards the all-trans product. b) Semiclassical potential energy surfaces for an electronic qubit coupled via a CI to two harmonic confining potentials. The color depicts the quantization axis of the qubit based on the location in the $x - y$ plane (blue $\leftrightarrow \hat{\sigma}_x$ and red $\leftrightarrow \hat{\sigma}_y$). The reactive coordinate x supports macroscopically distinct reactant and product ground states (linecut, bottom) associated with a two-dimensional electronic subspace $\{|\psi_1\rangle$ (white), $|\psi_2\rangle$ (black) $\}$.

where we choose to define $\hat{\sigma}_x = |\psi_1\rangle\langle\psi_1| - |\psi_2\rangle\langle\psi_2|$ as the operator that represents the electronic basis. Our model contains first-order intra- and inter-state couplings g_x and g_y, respectively, as well as generalized rovibrational frequencies Δ_a and Δ_b. The modes $\hat{a}$ and $\hat{b}$ are commonly referred to as tuning and coupling modes, respectively, as the coordinate $\hat{x} \propto \hat{a} + \hat{a}^\dagger$ "tunes" the electronic energy between $|\psi_1\rangle$ and $|\psi_2\rangle$ (Fig. 1b) and $\hat{y} \propto \hat{b} + \hat{b}^\dagger$ mediates coupling between the two electronic states via $\hat{\sigma}_y = |\psi_1\rangle\langle\psi_2| + |\psi_2\rangle\langle\psi_1|$. We note that in our interest of modeling chemical reactions, we will call the position of the tuning mode the "reactive coordinate", though we emphasize the generalized nature of these coordinates in this basis (i.e., one may need to perform a corresponding adiabatic-to-diabatic transformation). Such a model has historical origins in the well known Jahn-Teller effect which was originally thought to necessarily be rooted in molecular symmetries, but since has been extended to larger polyatomic molecules with conical intersections that are

not necessarily symmetry-induced [Domcke and Yarkony 2012]. In general, the parameters of this model may either be empirically fit to reproduce experimental data [Schneider and Domcke 1988] or obtained from *ab-initio* calculations such as for the extensively studied pyrazine [Seidner et al. 1992], the latter of which is challenging for larger polyatomic molecules.

Finally, we can incorporate dissipation into our model to reflect both rovibrational damping of the nuclear motion and spontaneous emission of an electronic excitation. The complete scope of our model can thus be captured by the following master equation:

$$\dot{\rho} = -\frac{i}{\hbar}[\hat{H}_{\text{LVC}}, \hat{\rho}] + \kappa_a \mathcal{D}[\hat{a}]\hat{\rho} + \kappa_b \mathcal{D}[\hat{b}]\hat{\rho} + \frac{\gamma_y}{2} \mathcal{D}[\hat{\sigma}_y]\hat{\rho} \tag{5.2}$$

where we have assumed white noise dissipators[1]. The influence of various forms of rovibrational damping on conical intersection dynamics has been theoretically and computationally investigated for a number of model systems [Kühl and Domcke 2002; Duan and Thorwart 2016; Schile and Limmer 2019].

5.2 Experimental design

In this section, we present an overview of our experimental design. Unlike the FC algorithm, we do not have a prescribed protocol to follow with regards to either a decomposition of a target unitary into discrete operations or a pre-specified measurement scheme. Rather, we are performing more of an analog quantum simulation by continuously enacting a target Hamiltonian $\hat{H}_{\text{LVC}}$ in the presence of dissipation.

Moreover, we began with a rather vaguely defined problem: how do excited wave-packets, like the ones produced in rhodopsin after light is absorbed, propagate through a complicated energy landscape that contains a conical intersection? We were able to construct a minimal model to try and simplify things, but even our simple model has seven parameters $(\Delta_a, \Delta_b, g_x, g_y, \kappa_a, \kappa_b, \gamma_y)$! The parameter space is certainly very large, so how

---

1. This is a simplifying assumption, as molecular environments in the condensed phase are typically very structured. Furthermore, here we are modeling both spontaneous relaxation and heating of the electronic state via $\mathcal{D}[\hat{\sigma}_y]$.

can we approach breaking the problem down and synthesizing interesting regimes to study? This is all not to even mention experimental constraints. Can we even faithfully enact our model Hamiltonian in the regimes that we care about? What kind of measurements can we perform that are of interest to the problem? Answering these questions constituted a significant portion of this research effort, and the answers are not so simple to explain because they are intimately intertwined between what we want to study and what we are able to engineer. What ultimately became an experimental reality did so in an extremely nonlinear fashion, as research tends to be. Nevertheless, we present here an attempt to provide some sort of logical flow to our design process, even if we didn't actually take such a smooth path.

5.2.1 Regime of interest of the model

Our target parameter regime of choice is one that closely follows what we expect for a realistic photochemical reaction. A hallmark of nonadiabatic reactions involving conical intersections is that they are ultrafast, mediated by both the intersection as well as vibrational damping. This suggests that a reaction is "completed" before the characteristic timescale of spontaneous emission of an electronic excitation. Thus, we want to work in a regime where the intrinsic electronic decoherence set by γ_y is much smaller than all of the other energy scales.

Next, in order to consider distinct reactant and product configurations along the reactive coordinate, we want the two ground states of our model to be macroscopically distinct. This translates to having $\alpha_g = g_x/\Delta \geq 1$ for the conditional displacement interaction on $\hat{a}$. We do not have such a requirement on the coupling mode $\hat{b}$. What we would like to have on both the nuclear modes, however, is dissipation that is much stronger than the intrinsic electronic decoherence $\{\kappa_a, \kappa_b\} > \gamma_y$ to study wave-packet localization. Notably, the presence of dissipation changes the previous macroscopic distinction requirement to $\alpha_g = g_x/\sqrt{\Delta_a^2 + \kappa_a^2/4} \geq 1$.

At this stage, we turn to what we can reasonably expect to engineer with our experimental hardware. This begins with a chosen strategy for enacting the interaction Hamiltonian $\hat{H}_{\text{LVC}}$. While there isn't necessarily one way to do this in a circuit QED system, we elect to

follow an approach taken in [Hacohen-Gourgy et al. 2016] and expand on it to satisfy our specific requirements.

5.2.2 Engineering the conical intersection

Upon inspection of Eq. 5.1, one notices that it consists of simultaneous conditional displacement interactions between two orthogonal axes of a single qubit with two different cavity modes. In section 3.3.3.2, we briefly described how combining a strong drive on a qubit with two sideband drives on a cavity can transform a cross-Kerr interaction into a conditional displacement. It turns out that this approach can be extended straightforwardly to multiple conditional displacements.

Deciding on the hardware and drive scheme to implement our desired interaction Hamiltonian leads to our first set of subtleties that we need to address. The analysis in section 3.3.3.2 for enacting the conditional displacement considered driving a true qubit. By deciding to use a transmon, which is an anharmonic oscillator, we need to revisit the analysis to understand what new conditions or constraints might arise. Specifically, by modifying

$$\hat{H}/\hbar : \omega_c \hat{c}^\dagger \hat{c} + \frac{\omega_q}{2}\hat{\sigma}_z + \frac{\chi}{2}\hat{c}^\dagger \hat{c}\hat{\sigma}_z \rightarrow \omega_c \hat{c}^\dagger \hat{c} + \omega_q \hat{q}^\dagger \hat{q} - \frac{\alpha_q}{2}\hat{q}^\dagger \hat{q}^\dagger \hat{q}\hat{q} - \chi \hat{c}^\dagger \hat{c}\hat{q}^\dagger \hat{q} \quad (5.3)$$

where now we designate α_q as the transmon anharmonicity, can we still arrive at a conditional displacement? A detailed account is provided in Appendix B, but we summarize the findings here. We are still able to engineer our desired interaction Hamiltonian:

$$\hat{H}_{\text{cd}}/\hbar = \Delta_c \hat{c}^\dagger \hat{c} - g(\cos(\varphi_\delta)\hat{\sigma}_x + \sin(\varphi_\delta)\hat{\sigma}_y)(\hat{c} + \hat{c}^\dagger) \quad (5.4)$$

where the qubit is defined as the lowest two energy eigenstates of the driven transmon $\{|\tilde{g}\rangle, |\tilde{e}\rangle\}$ with control over the conditional Pauli operator via the differential phase of the sidebands φ_δ. Moreover, we can also still enact multiple conditional displacements simultaneously, though the resonance conditions will be modified a bit due to Stark shifts. This enables us to indeed enact $\hat{H}_{\text{LVC}}$ as defined in Eq. 5.1. Furthermore, we need to incorporate a static detuning on our Rabi drive to eliminate the presence of additional undesired res-
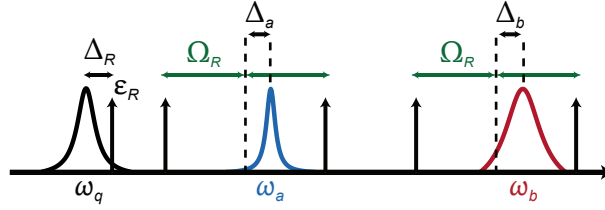
Figure 5.2 | **A modified drive configuration for conditional displacements.** To be compared with Fig. 3.11. The Rabi drive is now detuned, but still generates a Rabi qubit with energy $\Omega_R \approx \sqrt{\varepsilon_R^2 + \Delta_R^2}$.

onant terms, necessitating an adiabatic preparation of our conditional displacement eigenstates (Fig. 5.2). This, however, introduces a new issue which we are fortunately able to address in section 5.4.4.

To summarize, we are able to continuously engineer our desired interaction Hamiltonian, but with a few modifications compared to a standard implementation of these types of interactions involving Rabi qubits. We combine the findings of this section and the previous section to present a final hierarchy of energy scales for our experimental implementation.

5.2.3 Hierarchy of energy scales

We first highlight the boundaries of our energy hierarchy with respect to experimental requirements:

- We want the intrinsic decoherence of the elctronic qubit γ_y to be as small as possible. In our implementation, this is equivalent to the driven decoherence rate of our Rabi qubit $\Gamma_{2\rho} = \frac{1}{T_{2\rho}}$.

- The Rabi frequency Ω_R needs to be as large as possible in order to satisfy the RWA leading to Eq. 5.4, but cannot approach roughly half of the transmon anharmonicity α_q as that will activate additional resonant terms in the effective Hamiltonian.

Next, we decide to experimentally focus on the case where κ_a is also very small, i.e., the reactive coordinate does not experience significant damping. While this does not correspond to a realistic reaction, it enables a simpler analysis by effectively eliminating a parameter in the problem. It also eases the requirement on having a large enough g_x to
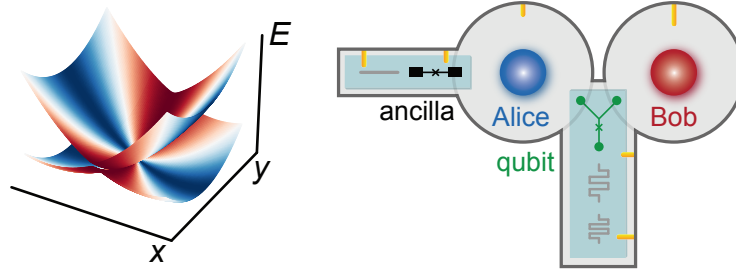
Figure 5.3 | **Mapping between our model Hamiltonian and our quantum simulator.**
Alice (blue) represents the tuning mode that defines the reactive coordinate, Bob (red) represents the coupling mode which will serve as a bath, and a transmon (green) will represent the electronic qubit. An additional ancilla module couples to Alice for state preparation and measurement.

enforce our macroscopically distinct reactive ground states. Thus, our final experimental energy hierarchy looks like:

$$\{\kappa_a, \Gamma_{2\rho}\} \ll \{g_x, g_y, \Delta_a, \Delta_b, \kappa_b\} \ll \Omega_R < \alpha_q \tag{5.5}$$

Through our experiment, we will further resolve the competition between the central energy scales.

5.3   Hardware overview

In section 5.2.2, we saw how a transmon qubit that is cross-Kerr coupled to two cavities is amenable to enacting our desired interaction Hamiltonian. Fig. 5.3 provides a concrete mapping between our desired model and the modes of our quantum simulator. There are two qualitative differences between the operating regime for this experiment and the one used for the FC experiment in Chapter 4. First, the transmon that couples to both cavities will now explicitly be a part of the system as the electronic degree of freedom, whereas before its only purpose was to facilitate four-wave mixing operations among the two cavities. This translates to using a transmon with a larger anharmonicity α_q. Second, the cavities will now intentionally be overcoupled to their respective transmission lines to effect a desired decay rate. In practice, we only do this for the coupling mode Bob, as discussed in section 5.2.3.
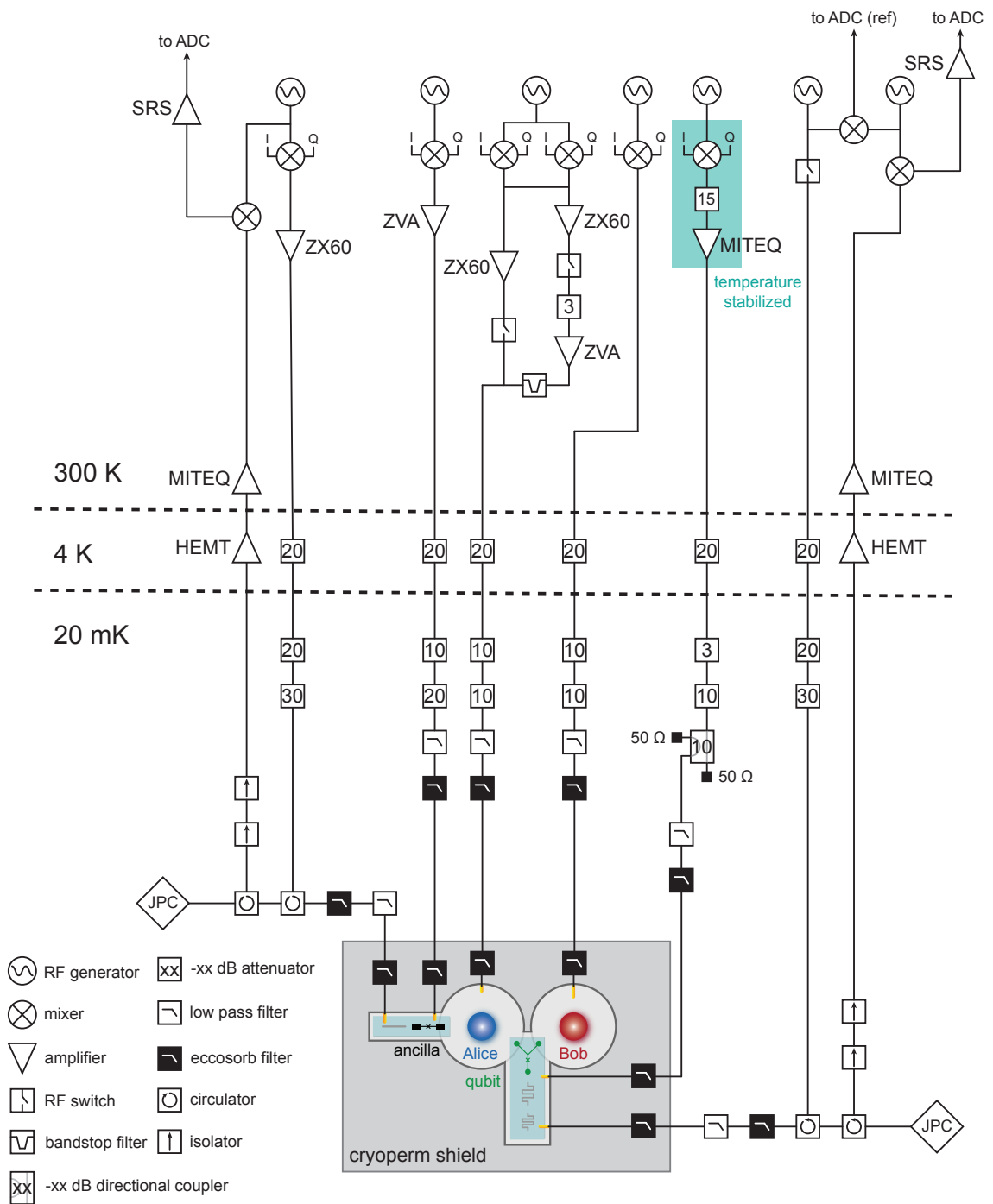
Figure 5.4 │ **Experimental wiring diagram for the conical intersection experiment.**

101

System quantity	Parameter	Value
Transmon frequency	$\omega_q/2\pi$	4850 MHz
Transmon anharmonicity	$\alpha_q/2\pi$	244 MHz
Transmon relaxation	T_1^q	80 μs
Transmon decoherence	T_2^q	7 μs
Alice frequency	$\omega_a/2\pi$	5436 MHz
Alice linewidth	$\kappa_a/2\pi$	0.23 kHz
Bob frequency	$\omega_b/2\pi$	6506 MHz
Bob linewidth	$\kappa_b/2\pi$	320 kHz
Alice - Transmon coupling	$\chi_{aq}/2\pi$	295 kHz
Bob - Transmon coupling	$\chi_{bq}/2\pi$	210 kHz
Ancilla frequency	$\omega_{qa}/2\pi$	4509 MHz
Ancilla relaxation	T_1^{qa}	60 μs
Ancilla decoherence	T_2^{qa}	10 μs
Alice - Ancilla coupling	$\chi_{a,qa}/2\pi$	845 kHz

Table 5.1 | List of system parameters for the conical intersection experiment.

A wiring diagram for this experiment in shown in Fig. 5.4. The primary feature to note is that we actively stabilize the local air temperature around the microwave components along the control line for the Rabi drive. This will be critical to ensuring that we can perform our experiment by mitigating drfits in the Rabi frequency over time caused by temperature-dependent variations in the gain of our amplification chain. We provide a detailed account of this process in Appendix C.

5.4 Experimental implementation

In this section, we describe the details of our experimental implementation. The static system parameters is given in Table 5.1.

5.4.1 Frame tracking the Rabi qubit

Our two electronic states are encoded by a driven transmon whose effective frequency Ω_R is defined by the amplitude ε_R and static detuning Δ_R of the Rabi drive (Fig. 5.2). In the rotating frame of the drive, we define the Rabi qubit Hamiltonian to have the form $\hat{H}_d = \frac{\Omega_R}{2}\hat{\sigma}_z$
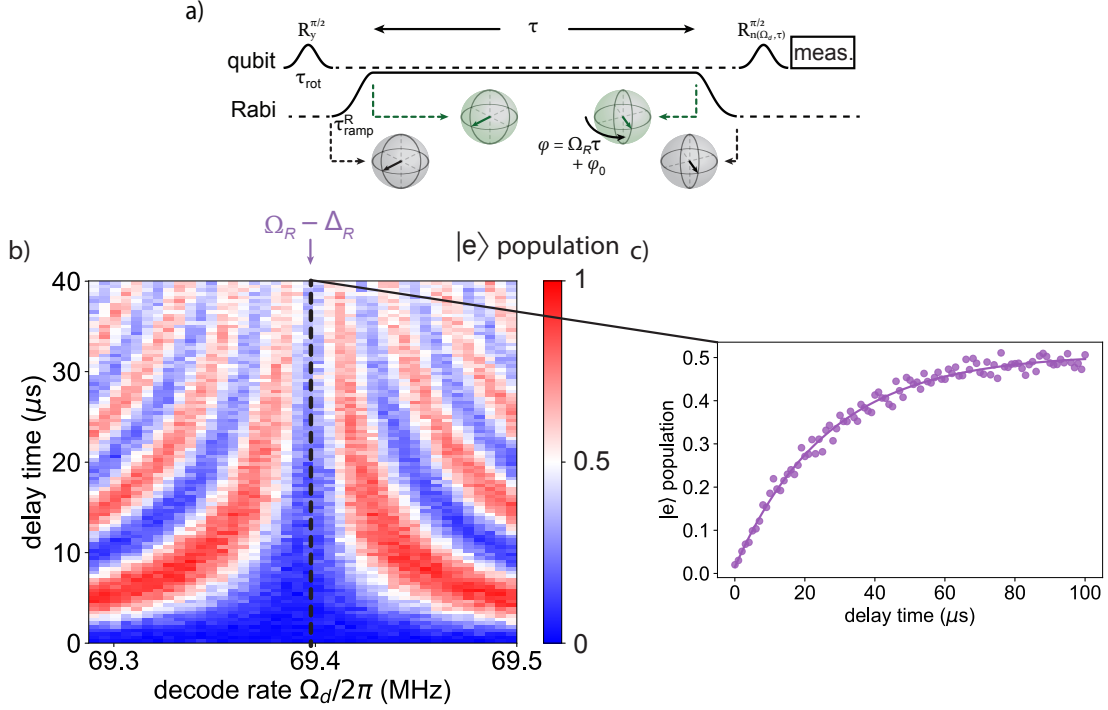
Figure 5.5 | State tomography and decoherence of transverse Bloch vectors. a) A Ramsey-style pulse sequence is used to calibrate the decode rate. The final $\pi/2$ rotation has a phase that depends on both the delay time τ and the programmed decode rate Ω_d. b) The 2D plot reveals an optimal decode rate which is inferred to be equal to the true Rabi frequency offset by the static detuning $\Omega_R - \Delta_R$. c) The decode rate can then be fixed to the optimal value to extract a driven decoherence time $T_{2\rho} \approx 27$ μs via fitting to an exponential decay function (solid line).

when expressed in the driven eigenbasis spanned by $\{|\tilde{g}\rangle, |\tilde{e}\rangle\}$ that adiabatically connects to the undriven transmon eigenstates $\{|g\rangle, |e\rangle\}$. The conditional displacement interactions that we will engineer in our experiment are conditioned on Pauli operators whose eigenstates lie on the equator of the *driven* Bloch sphere (i.e., $\hat{\sigma}_x$ and $\hat{\sigma}_y$), and thus will precess around the equator at a rate Ω_R (Fig. 5.5). We choose this convention because we prefer the eigenstates of $\hat{\sigma}_z$ to be stationary in the frame of the drive. From the perspective of the model molecular system, however, eigenstates of $\hat{\sigma}_x$ are the electronic states of interest. We initialize these eigenstates $\{|\pm\rangle\}$ of $\hat{\sigma}_x$ in the driven frame by first preparing the corresponding states of the undriven transmon via a standard $\pi/2$ rotation and then adiabatically ramping on the Rabi drive $\tau_{\text{ramp}}^R \gg 1/\Delta_R$. In order to properly track the dynamics of any such state, we need to precisely know the Rabi frequency Ω_R so that we can decode along the appropriate axis onto our measurement basis. By calibrating this rate, we are able to

continuously measure $\langle \hat{\sigma}_x \rangle$ as a function of time. This is then equivalent to a measurement of the electronic populations, which is a key observable of interest for our simulations.

Experimentally, $\langle \hat{\sigma}_x \rangle$ will decay over time due to both intrinsic relaxation of the transmon in the driven frame $T_{1\rho}$ and amplitude noise in the Rabi drive which contributes to dephasing $T_{\varphi\rho}$ in the driven frame. Combined, these two generate a driven decoherence rate $\Gamma_{2\rho} = \Gamma_{1\rho} + \Gamma_{\varphi\rho}/2$ [Gustavsson et al. 2012], which corresponds to a symmetric spontaneous emission and excitation rate of the two electronic states. Realistic systems are dominated by spontaneous emission, suggesting that engineering a mechanism where this symmetry is broken would be an interesting capability to acquire. Nevertheless, following our chosen target regime as described in section 5.2.3, this rate dictates how large the other interaction strengths of our problem need to be. As shown in Fig. 5.5, we are able to achieve $\Gamma_{2\rho}/2\pi \approx 6\,\text{kHz}$. We were only able to achieve this by using an extremely low noise amplifier combined with active temperature stabilization as discussed in Appendix C. Otherwise, we use the same set of controls as described in section 4.2.1.

5.4.2 Calibrating individual sidebands

In our modified scheme where we incorporate a static detuning on the Rabi drive, the sideband interactions have the form:

$$\hat{H}_{\text{red}}/\hbar = g\hat{c}\hat{\sigma}_z^- + g^*\hat{c}^\dagger\hat{\sigma}_z^+ \tag{5.6}$$

$$\hat{H}_{\text{blue}}/\hbar = g\hat{c}\hat{\sigma}_z^+ + g^*\hat{c}^\dagger\hat{\sigma}_z^- \tag{5.7}$$

which one will note is the opposite designation as compared to Eqs. 3.45 and 3.46. This is because in the frame of the Rabi drive, the resulting spectrum has negative energies and thus the state that adiabatically connects to the excited undriven transmon state $|e\rangle \leftrightarrow |\tilde{e}\rangle$ has energy $-\Omega_R$ with respect to $|g\rangle \leftrightarrow |\tilde{g}\rangle$ Here we define $\hat{\sigma}_z^+ = |\tilde{e}\rangle\langle\tilde{g}|$ and $\hat{\sigma}_z^- = |\tilde{g}\rangle\langle\tilde{e}|$ as the raising and lowering operators of the Rabi qubit eigenstates that adiabatically connect to the ground and first excited state of the transmon. For our system, we have $\hat{c} \in \{\hat{a}, \hat{b}\}$. The qualitative behavior of each individual sideband interacting with the Rabi qubit will be different given that we are operating in the regime where $g > \kappa_a$ and $g \leq \kappa_b$. The former
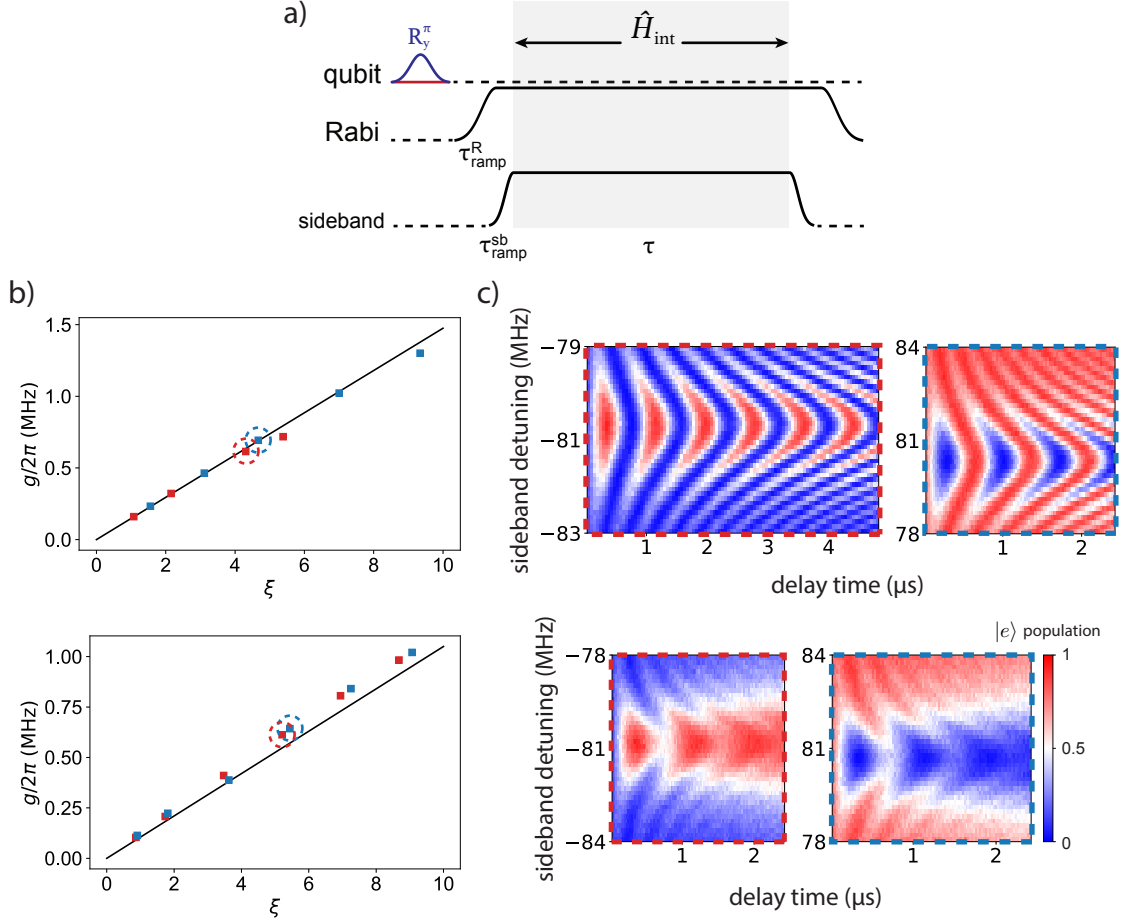
Figure 5.6 | Calibrating individual exchange interactions. a) Pulse sequence for enacting $\hat{H}_{\text{int}} \in \{\hat{H}_{\text{red}}, \hat{H}_{\text{blue}}\}$. The qubit is prepared in the ground state for the red sideband and in the excited state for the blue sideband. b) Interaction strength for each sideband as a function of a dimensionless displacement amplitude of the cavity for Alice (top) and Bob (bottom). Solid line represents expectation based on χ. c) Raw data of qubit populations for individual calibrations labeled in (b). The sideband detunings are referenced to the cavity frequencies, showing that we are operating at Rabi frequencies $\Omega_R/2\pi \approx 80$ MHz.

will result in either creating and annihilating two excitations simultaneously $|\tilde{g}, 0\rangle \leftrightarrow |\tilde{e}, 1\rangle$ (red sideband) or a coherent exchange between an excitation in the driven qubit and a photon in the cavity $|\tilde{e}, 0\rangle \leftrightarrow |\tilde{g}, 1\rangle$ (blue sideband) [Lu et al. 2017]. The latter will stabilize the qubit in either the driven excited state $|\tilde{e}\rangle$ (red sideband) or the driven ground state $|\tilde{g}\rangle$ (blue sideband) [Murch et al. 2012]. To emphasize the connection between our convention and the standard resonant Rabi qubit case, note that $|\tilde{g}\rangle$ strongly resembles $\frac{1}{\sqrt{2}}(|g\rangle + |e\rangle)$ and $|\tilde{e}\rangle$ strongly resembles $\frac{1}{\sqrt{2}}(|g\rangle - |e\rangle)$ in the lab frame.

In order to calibrate the interaction strengths, we will operate in the restricted two-

dimensional subspace of the joint Hilbert space of the cavity and qubit as described above. This allows us to simplify our analysis and replace the qubit raising and lowering operators $\hat{\sigma}_x^{\pm}$ with general bosonic creation and annihilation operators $\hat{d}^{(\dagger)}$. We then follow the treatment in [Pfaff et al. 2017; Grimm et al. 2020] and capture the full range of dynamics by solving the equations of motion for $\hat{d}$ under $\hat{H}_{\mathrm{blue}}$ and incorporating a cavity damping rate κ. We also include a static detuning term $\delta\hat{c}^{\dagger}\hat{c}$ to capture the effect of sweeping the pump frequency that enables the interaction. The resulting field has the form:

$$\hat{d}(t) = \frac{\hat{d}(0)}{\Omega} e^{-\frac{\kappa_{\mathrm{eff}} t}{4}} \left(\Omega \cosh\left(\frac{\Omega t}{4}\right) + \kappa_{\mathrm{eff}} \sinh\left(\frac{\Omega t}{4}\right) \right) \tag{5.8}$$

where $\Omega = \sqrt{\kappa_{\mathrm{eff}}^2 - (4g)^2}$ and $\kappa_{\mathrm{eff}} = \kappa + 2i\delta$.

For each interaction, we prepare our system in either $|\tilde{g}, 0\rangle$ (red sidebands) or $|\tilde{e}, 0\rangle$ (blue sidebands) by ramping the Rabi drive on undriven states $|g, 0\rangle$ and $|e, 0\rangle$, respectively. We then scan the frequency of the cavity sideband and the delay time for a given pump amplitude. By measuring the qubit population, we extract $\langle \hat{d}^{\dagger}(t)\hat{d}(t)\rangle$ and can fit the resulting data using Eq. (5.8) (Fig. 5.6). For the exchange interaction under the blue sideband, we have $\langle \hat{d}^{\dagger}(0)\hat{d}(0)\rangle_{\mathrm{blue}} = 1$ for the qubit initially in its excited state, giving us an expression for $\langle \hat{d}^{\dagger}(t)\hat{d}(t)\rangle_{\mathrm{blue}}$. For the red sideband, the features are qualitatively identical, with the exception that the qubit starts out in the ground state, giving us $\langle \hat{d}^{\dagger}(t)\hat{d}(t)\rangle_{\mathrm{red}} = 1 - \langle \hat{d}^{\dagger}(t)\hat{d}(t)\rangle_{\mathrm{blue}}$. Notably, this assumes that the effective interaction strength g is independent of the pump detuning δ, which is strictly not true but should be a very good approximation in our regime given that the scale of the chevron features, set by g, is much smaller than the absolute detuning from the cavity resonance $\sim\Omega_R$. We allow for an overall amplitude, global offset, and time offset in our fit, leaving g and κ to be the only free parameters. In the case of Bob, we first perform this fit for a range of interaction strengths $g \approx \kappa_b$ and extract a decay rate $\kappa_b/2\pi \approx 320$ kHz. For the remainder of the calibrations where $g < \kappa_b$, we fix this quantity and let the interaction strength g be the only free parameter to be fitted.

106
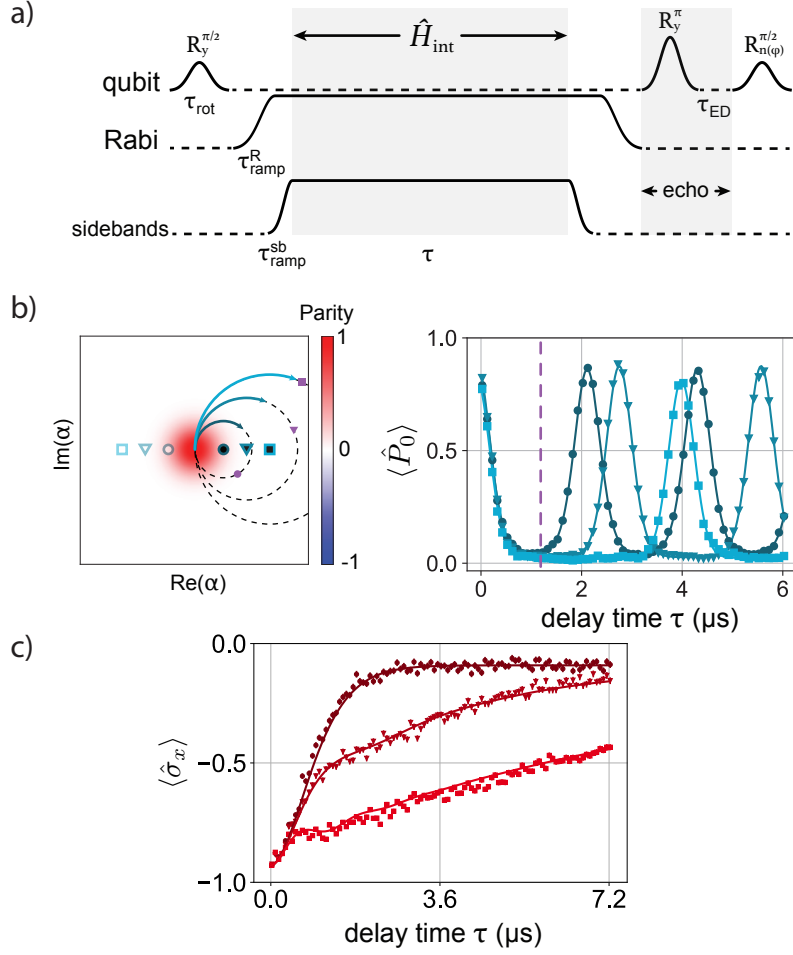
Figure 5.7 | Calibrating conditional displacements. a) Pulse sequence for conditional displacement calibrations, where $\hat{H}_{\text{int}} = \{\hat{H}_a, \hat{H}_b\}$. The qubit is prepared in a superposition state that adiabatically connects to $|+\rangle$ in the driven basis. An echo sequence eliminates residual entanglement during the ramp-off time (see section 5.4.4). b) Coherent state revivals of vacuum under a conditional displacement in Alice. Fitting the vacuum population according to Eq. 5.11 allows us to extract $g_x/2\pi = 450$ kHz and $\Delta_a/2\pi = 457$ kHz (circles), 355 kHz (triangles), and 246 kHz (squares). c) Measurement-induced dephasing of $|-\rangle$ under a conditional displacement interaction combined with Bob's dissipation.

5.4.3 Calibrating conditional displacements

The combination of simultaneous red and blue cavity sidebands enacts a conditional displacement interaction. This requires that two conditions are fulfilled: 1) the strength of both individual sideband interactions are equal and 2) the frequency difference between the two sidebands equals twice the Rabi frequency. If these two conditions are met, then we can model the interaction using Eq. 5.4. The two conditional displacements on Alice

and Bob are:

$$\hat{H}_a/\hbar = \Delta_a \hat{a}^\dagger \hat{a} + g_x \hat{\sigma}_x(\hat{a} + \hat{a}^\dagger) \tag{5.9}$$

$$\hat{H}_b/\hbar = \Delta_b \hat{b}^\dagger \hat{b} + g_y \hat{\sigma}_y(\hat{b} + \hat{b}^\dagger). \tag{5.10}$$

where we have designated the desired phases.

In practice, the presence of each sideband will Stark shift both the transmon and cavity modes. Thus, to capture the dominant effect of all of these Stark shifts (which influences the resonance condition), we perform individual sideband calibrations with the opposite sideband on but detuned by an amount larger than the interaction strength we are using (i.e. by an additional 2 MHz in our experiments). We scan the pump amplitudes and match the individual sideband strengths before bringing both sidebands into resonance. This relies on the assumption that over a variation of ∼2 MHz, the relative change in the cavity Stark shift, which influences the dimensionless pump strength that determines the interaction strength, is negligible. Finally, we fine tune the difference frequency of the two sidebands while keeping the average value fixed (which fixes Δ_c in Eq. 5.4) in order to account for any change in the Rabi frequency which we are very sensitive to. This sensitivity is revealed by measuring the transverse relaxation time $T_{2\rho}$, and choosing a calibration point where this value is maximized, suggesting that the resonance conditions are fulfilled as best as possible.

Finally, the phase needs to be calibrated appropriately. As discussed in Appendix B, the differential phase of the sidebands relative to the qubit phase determines the Pauli operator of the conditional displacement. The phase of the initial $\pi/2$ rotation on the transmon defines the qubit phase, i.e., defines $\hat{\sigma}_x$. By scanning the differential phase of the sidebands, we adjust the axis of the Pauli operator defining the conditional displacement to be either aligned or orthogonal to the initial state. Thus, we can perform the above calibration and demonstrate various conditional displacements for both Alice and Bob using a fixed interaction strength but varying detunings (Fig. 5.7).

For Alice, where $g_x \gg \kappa_a$, the dynamics of an initial vacuum state $|\alpha_0 = 0\rangle_a$ evolving under Eq. 5.9 depends on the qubit state. If the qubit in $|\mp\rangle$, i.e. an eigenstate of the Pauli operator defining the conditional displacement, the cavity will perform a circular trajectory

in phase space around the location of the respective ground state $\alpha_g = \pm g_x/\Delta_a$. If the qubit is not in an eigenstate, then the qubit and cavity will begin to entangle over time and the cavity state will follow the two trajectories simultaneously. We calibrate the differential phase to ensure that we follow the first scenario, which represents an initial wave-packet in a well-defined electronic eigenstate. This is done by enacting the interaction for roughly half a period $\tau = 1/2\Delta_a$ and scanning both the differential sideband phase and the phase of a displacement with magnitude $2\alpha_g$. The correct differential phase will be the one that keeps the cavity in a coherent state throughout the entire trajectory, and thus can be displaced back to the origin to create a vacuum state.

By measuring the population in $|n = 0\rangle_a$ after the differential phase is calibrated, we are effectively measuring the overlap of a coherent state with itself as it oscillates in time. This justifies the use of a simple model, where the state autocorrelation function is $\langle \beta e^{-i\Delta_a t}|\beta\rangle = e^{|\beta|^2(e^{-i\Delta_a t}-1)}$. The corresponding probability is:

$$P_0 = |\langle \beta e^{-i\Delta_a t}|\beta\rangle|^2 = e^{2|\beta|^2(\cos[\Delta_a t]-1)} \tag{5.11}$$

To make the connection with our model, we choose $\beta = \alpha_g = g_x/\Delta_a$.

We operate the conditional displacement on Bob in the regime where $g_y \leq \kappa_b$. The combination of a conditional displacement interaction with dissipation results in measurement-induced dephasing of the qubit along the axes orthogonal to the one defined by the interaction [Didier, Bourassa, and Blais 2015; Touzard et al. 2019; Touzard 2019]. We calibrate and verify this behavior by preparing $|-\rangle$, tuning the qubit axis of the interaction to be $\hat{\sigma}_y$ by adjusting the relative phase of Bob's sidebands to maximize the dephasing, and measuring the coherence as a function of time for different values of Δ_b. In all of our experiments, we begin with Bob near the vacuum state $|0\rangle_b$.

5.4.4 Echoing the residual cross-Kerr

The adiabatic preparation of our driven qubit eigenstates has two benefits: for a fixed transmon anharmonicity, we can 1) use larger Rabi frequencies while cancelling the residual cross-Kerr and 2) avoid leakage events to higher transmon levels (up to natural heating rates
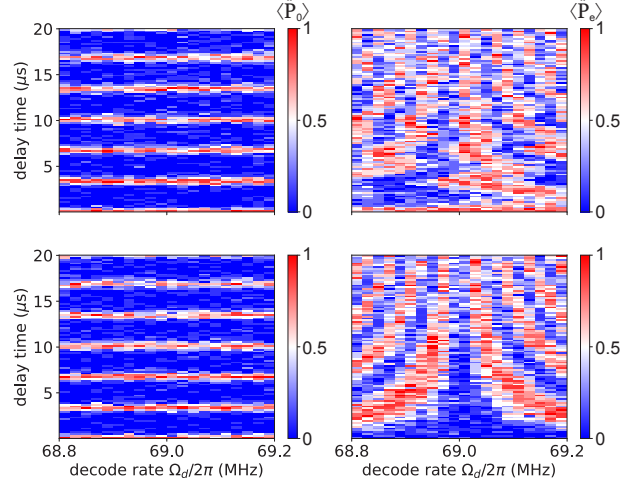
Figure 5.8 | Echoing away residual entanglement. Simultaneous measurement of Alice's vacuum projector via a transmon ancilla (left) and the driven qubit (right) while a conditional displacement interaction is active. The pulse sequence used for this calibration is shown in Fig. 5.7 without (top) and with (bottom) the π rotation and echo delay τ_{ED} and only sidebands on Alice. Time dynamics of Alice's vacuum projector reveals coherent revivals as expected, independent of the decode rate on the Rabi qubit. Scanning the decode rate without the echo sequence results in distortions to the driven Ramsey data that are correlated with the cavity photon distribution. Implementing the echo sequence eliminates this effect, suggesting that the systems remain unentangled at all delay times. Here, we use an optimized value of the delay time $\tau_{\mathrm{ED}} = 144$ ns.

of the dressed eigenstates) associated with a resonant drive. The primary consequence of this approach is the undesired interaction between the qubit and cavity photons during the ramp time of the Rabi drive.

Qualitatively, this undesired interaction stems from ramping between the static interaction Hamiltonian $\hat{H}_{\mathrm{int}}/\hbar = -\chi \hat{c}^\dagger \hat{c} \hat{q}^\dagger \hat{q}$ and the driven Hamiltonian where the cross-Kerr interaction is nulled. Thus, if there are photons in the cavity during either the ramp on or off of the Rabi drive, they will entangle with the superposition states of the qubit that we are manipulating. We can avoid this effect during the ramp on of the Rabi drive by performing our displacement operation after the Rabi drive is fully ramped on, i.e. during the time when the cross-Kerr interaction is nulled. For addressing the entanglement during the ramp off of the Rabi drive, we implement a simple and short echo sequence of the qubit to un-do the interaction. This works because the entanglement is fully determined by χ and the ramp time τ_{ramp}^R and not the cavity photon distribution. This is important as we do not

want a scheme which depends on the cavity state that we are manipulating. Fig. 5.8 shows how implementing this protocol eliminates spurious features that arise from this entanglement when performing a decode calibration experiment when a conditional displacement interaction with Alice is active. In practice, this calibration is only done with respect to photons in Alice. Given that we operate Bob in a regime where $g_y < \kappa_b$, the photon distribution in Bob remains relatively small and thus any residual entanglement effects are negligible.

5.4.5 Correlating qubit dephasing and wave-packet branching

Before enacting the conical intersection, which has nontrivial and highly entangled eigenstates, we perform both conditional displacement interactions simultaneously but coupled to the same qubit axis:

$$\hat{H}_x/\hbar = \Delta_a \hat{a}^\dagger \hat{a} + \Delta_b \hat{b}^\dagger \hat{b} + g_x \hat{\sigma}_x (\hat{a} + \hat{a}^\dagger) + g_y \hat{\sigma}_x (\hat{b} + \hat{b}^\dagger) \tag{5.12}$$

which we can engineer via aligning the phases of Bob's sidebands with respect to those on Alice. In this scenario, the measurement-induced dephasing from the coupling mode should not perturb the dynamics of a reactive wave-packet prepared with an eigenstate of the qubit axis $\hat{\sigma}_x$. Furthermore, we want to prepare reactive wave-packets at different locations to eventually probe the phase space dynamics of the full system.

The cavity phase of the conditional displacement (i.e. the phase which defines the position operator $\hat{x} \propto (\hat{c}e^{i\varphi_\Sigma} + \hat{c}^\dagger e^{-i\varphi_\Sigma})$) is determined by the sum phase of the red and blue sidebands (see Appendix B). Given that we are turning on the conditional displacement interaction suddenly ($\tau_{\text{ramp}}^{\text{sb}} \ll 1/g$), the phase of our initial displacement operation $\hat{\mathcal{D}}(\alpha_0)$ on Alice will determine the location in the driven phase space where the wave-packet begins. Displacements whose phase is aligned to the conditional displacement cavity phase will prepare wave-packets along the position axis, whereas care needs to be taken to prepare wave-packets with various momenta that are located at one of the two ground state positions. Since we are interested in modeling scenarios where a wave-packet arrives on a potential energy surface via optical excitation in a Franck-Condon region, we prepare coherent states with no initial momentum along the reaction coordinate.
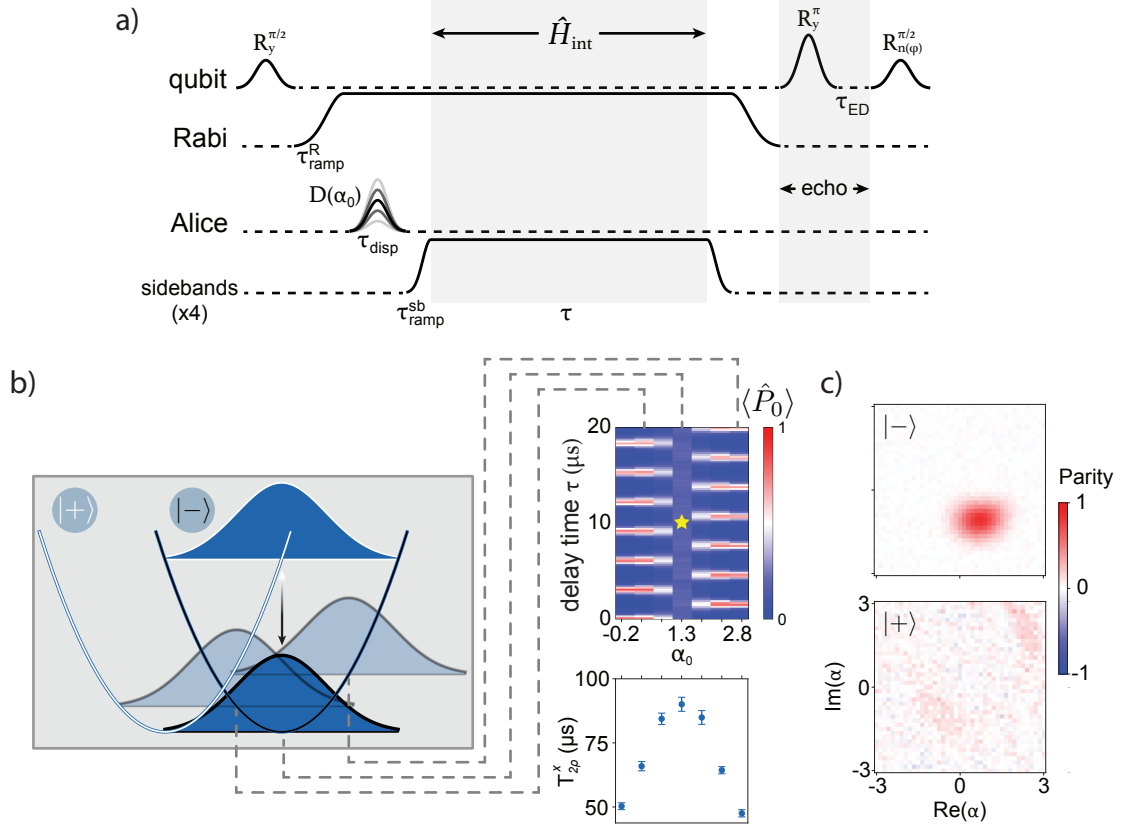
Figure 5.9 | Wave-packet initialization and correlated branching. a) Pulse sequence for simultaneous conditional displacements, where $\hat{H}_{\text{int}} = \{\hat{H}_x, \hat{H}_{\text{IVC}}\}$. b) Depiction of various wave-packets prepared along the reactive coordinate under a conditional displacement interaction with $\hat{\sigma}_x$ of the qubit, as well as a qubit dephasing event on a ground state wave-packet. By preparing the qubit in $|-\rangle$, initializing Alice in various coherent states, and then suddenly turning on the interaction, we observe coherent revivals of the wave-packet by measuring the projection onto vacuum. The parameters here are $g_x/2\pi \approx 410$ kHz and $\Delta_a/2\pi \approx 324$ kHz, giving $\alpha_g = g_x/\Delta_a \approx 1.3$. Simultaneously tracking the qubit in the $\hat{\sigma}_x$ basis reveals driven coherence times $T_{2\rho}^x > 50\mu$s, with some dependence on $\langle \hat{a}^\dagger \hat{a} \rangle$. c) Measured Wigner functions of Alice's state conditioned on the $\hat{\sigma}_x$ measurement outcome being either $|-\rangle$ (top, $P_- = 91\%$) or $|+\rangle$ (bottom, $P_+ = 9\%$) after evolving $|\psi_0\rangle = |-\rangle \otimes |+\alpha_g\rangle_a$ for 10 μs under the interaction (yellow star in b.).

In order to calibrate the displacement phase, we begin with a calibrated conditional displacement where we have extracted g_x and Δ_a, which gives us a value for the ground state amplitude $\alpha_g = g_x/\Delta_a$. Note that this does not rely on any displacement phase since we are starting off in a vacuum state. Next, we scan the phase of an initial displacement of $2\alpha_g$ and turn on the conditional displacement interaction for various delay times. The optimal phase will be the one where we recover revivals that are half a period out of phase from those in Fig. 5.6. This can be interpreted as follows. A vacuum state in the lab

frame $|0\rangle_{\mathrm{lab}}$ looks like a displaced state $|-\alpha_g\rangle_{\mathrm{disp}}$ with respect to the displaced ground state $|\alpha_g\rangle_{\mathrm{lab}} = |0\rangle_{\mathrm{disp}}$, and thus will oscillate around the ground state, reaching $|\alpha_g\rangle_{\mathrm{disp}}$ after half a period. By determining the phase that enables us to prepare $|\alpha_g\rangle_{\mathrm{disp}}$ (which is $|2\alpha_g\rangle_{\mathrm{lab}}$ in the lab frame and will return to the vacuum state $|-\alpha_g\rangle_{\mathrm{disp}}$ after half a period) we can prepare any state along the position axis, including the displaced ground state.

We program our system with calibrated parameters $g_x/2\pi = 410$ kHz, $\Delta_a/2\pi = 324$ kHz, $g_y/2\pi \approx 156$ kHz, and $\Delta_b/2\pi \approx 0$ kHz. From the above consideration, the interaction strengths for Bob's conditional displacement should not influence the dynamics of states in Alice. We note that a photochemical reaction would involve a broadband optical excitation from a ground state to a higher potential energy surface, which in our model would correspond to performing a transition between $\hat{\sigma}_x$ eigenstates. Alternatively, we can directly prepare the wave-packet after the optical transition. We initialize different wave-packets by performing a displacement $\hat{\mathcal{D}}(\alpha_0)$ of varying α_0 with the appropriate phase before the sidebands are activated and observe coherent oscillations around the ground state, probed with measurements of the vacuum projector as before (Fig. 5.9).

The presence of the conditional displacement interactions breaks the decoherence degeneracy between x and y, thus we simultaneously measure the coherence time along the $x-$axis $T_{2\rho}^x$. In our efforts to understand the decoherence that is induced on the full system solely via the coupling mode, $T_{2\rho}^x$ sets the timescale before which we need to execute our desired interactions. Notably, we find that $T_{2\rho}^x$ is weakly dependent on the initial cavity state and peaks for the displaced ground state. This might be explained by the presence of a residual cross-Kerr interaction (section 5.4.4) which slightly modifies the effective qubit energy in time when a non-stationary cavity state is prepared and biases the Ramsey measurement. Furthermore, the fact that the coherence is longer compared to when the conditional displacements are off ($T_{2\rho}$) suggests an additional protection mechanism owing to the energy gap between eigenstates of $\hat{\sigma}_x$. Nevertheless, this weak dependence does not significantly impact our results given that our characteristic dissipation-induced interaction time will be much smaller than the shortest of the measured driven coherence times.
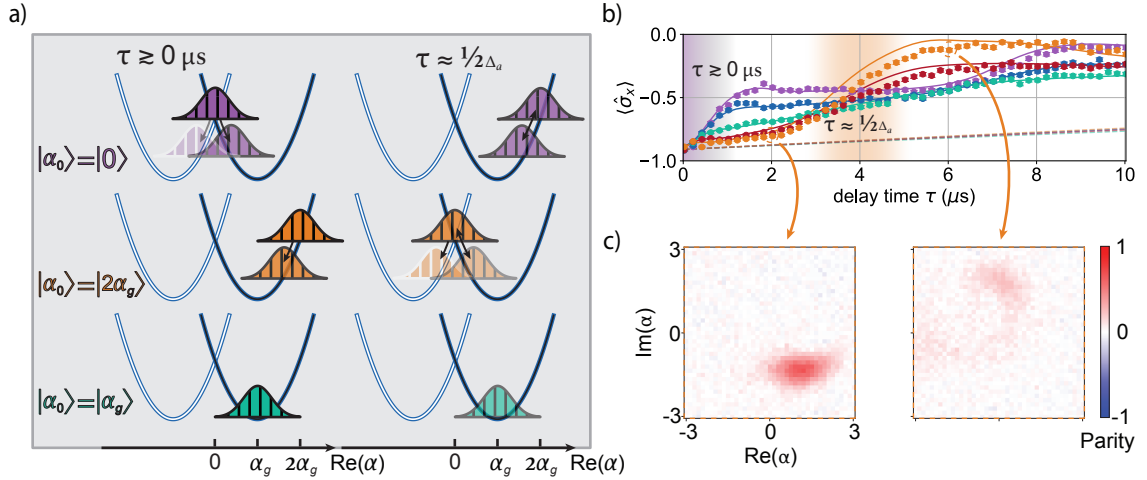
Figure 5.10 | Branching through a conical intersection. a) The system is initialized with the qubit in $|-\rangle$ (black potential energy surface) with three different initial wavepackets $|\alpha_0\rangle_a \approx \{|0\rangle_a$ (purple, top-left), $|2\alpha_g\rangle_a$ (orange, center-left), and $|\alpha_g\rangle_a$ (blue-green, bottom-left)$\}$, where $g_x/2\pi \approx 158.0$ kHz and $\Delta_a/2\pi \approx 125.8$ kHz giving $\alpha_g = g_x/\Delta_a \approx 1.26$. b) Measured expectation value of $\hat{\sigma}_x$ with standard error bars over time for the three different initial states. The purple wave-packet prepared at the CI immediately dephases, whereas the other two dephase more slowly, as they are farther away. After half of an oscillation period $\tau \sim 1/(2\Delta_a)$, the orange wave-packet arrives at the CI and dephases. Solid lines are predictions from a master equation simulation using independently fitted parameters. Dashed lines represent the negligible background decoherence due to $T_{2\rho}^x$ on the timescale of the interaction and dissipation. c) Unconditional Wigner tomography on Alice at $\tau = 2$ μs (left) and 6 μs (right) for preparing $|\alpha_0\rangle_a \approx |2\alpha_g\rangle_a$, revealing a coherent wave-packet before and dephased state after passage through the CI. The distortion of the Wigner function from a Gaussian at $\tau = 2$ μs suggests the presence of a residual self-Kerr nonlinearity in the oscillator.

5.4.6 Wave-packet branching through a conical intersection

The primary task of our experiment is to understand the time dynamics of excited reactive wave-packets, particularly through the CI. With our understanding that qubit dephasing along $\hat{\sigma}_x$ drives wave-packet branching, we prepare the qubit in $|-\rangle$ and directly monitor $\langle\hat{\sigma}_x\rangle$ as a function of time for different initial wave-packet configurations in the tuning mode (Fig. 5.10). Here, we program our system with calibrated parameters $g_x/2\pi = 158.0$ kHz, $\Delta_a/2\pi = 125.8$ kHz, $g_y/2\pi = 115$ kHz, and $\Delta_b/2\pi \approx 0$ kHz. In this instance, we reduce the interaction strengths of the reactive potential surface to get a clear signature of branching over the course of one period of motion, and choose zero detuning on the coupling mode's conditional displacement to achieve the strongest dephasing, representing a very slow in-

tranuclear mode. We observe the hallmark of dynamics through the CI - the qubit dephasing is both highly non-exponential and stronger upon passage of the wave-packet through the intersection. Additionally, we further verify that this behavior indeed correlates with dephasing of the cavity state by taking Wigner functions of an initially displaced wave-packet before and after passage through the CI. In our case, preparation of an excited wave-packet in the Franck-Condon region leads to large photon numbers that enact higher order Rabi frequency shifts that bias our measurement.

5.5 Dissipation analysis

In general, one must solve the full master equation Eq. 5.2 numerically for arbitrary input states, particularly when the value of all the parameters are of the same order. We can, however, qualitatively understand the decoherence behavior to an extent by treating the tuning mode classically. Here, we are left with a simplified Hamiltonian

$$\hat{H}_{\text{Zeno}}/\hbar = E(x)\hat{\sigma}_x + \Delta_b \hat{b}^\dagger \hat{b} + g_y \hat{\sigma}_y(\hat{b} + \hat{b}^\dagger) \tag{5.13}$$

subject to single photon loss on mode $\hat{b}$ at a rate κ_b. The function $E(x)$ can be interpreted as the position dependent energy gap (in frequency units) between qubit states for a conditional displacement interaction. At the CI, i.e., at $x = 0$, this energy gap vanishes and we are left with the environment measuring $\hat{\sigma}_y$ with a measurement strength $\Gamma_{\text{meas}} = g_y^2 \kappa_b / [(\kappa_b/2)^2 + \Delta_b^2]$ in the steady state where $g_y \ll \kappa_b$. Away from the origin, the qubit has a finite energy along an orthogonal axis to that of the measurement and we recover a scenario reminiscent of Zeno dynamics of a driven qubit [Gambetta et al. 2008]. This reduces the effective measurement strength, resulting in slower decoherence and thus reduced branching events. Our experiment may qualitatively be understood from this perspective by choosing a time-dependent trajectory $x(t)$ for an initial Gaussian wave-packet. In our full model, wave-packets in the tuning mode will diffuse in phase space due to the branching, resulting in dynamics that are quantitatively different from the above simplified model.

5.6   Future directions

Where can one go from here? Within the scope of our simple model, there is of course more of the parameter regime to be explored. The addition of κ_a as a tuning knob, particularly in the regime $\kappa_a \sim \kappa_b$, expands the landscape of competing forces in our model and represents a more realistic description of a reaction by defining a quantum yield as the wave-packets localize. It is possible to tune the decay rate of each oscillator *in-situ* via mechanical means in our 3D architecture, which would enable a flexible way to explore the wider range of parameter space in a single cooldown. Moreover, the model can be expanded to include more accurate features such as a fixed electronic energy $E_0 \hat{\sigma}_x$ or potential surface anharmonicities.

Perhaps a more pressing research question, however, is exactly where can this type of dissipative quantum simulation take us? Rather than attempt to use the model we developed as a starting point for adding more complexity, we ought to first contextualize this work against other well studied systems. The combination of interactions between qubits and oscillators and dissipation has formed the basis for a wide range of interesting physics.

In the context of molecular systems, the model we chose resembles that of electron transfer, which has been extensively studied. The role of the environment and dissipation is one of the most influential components in determining reaction rates, and has been considered for instance in [Garg, Onuchic, and Ambegaokar 1985]. Furthermore, [Mostame et al. 2012] outlines a blueprint for simulating exciton transport in photosynthetic complexes using superconducting circuits, where the primary feature is representing a non-Markovian bath using environmental degrees of freedom in the simulator itself.

Even more generally, our model falls under an instance of a generalized spin-boson model which is a ubiquitous model for studying the decoherence of a two-level system coupled to a bath of harmonic oscillators [Thorwart, Paladino, and Grifoni 2004]. We note that efficient classical computational methods based on matrix product states have been developed for studying quantum systems coupled to non-Markovian [Strathearn et al. 2018] and even arbitrary environments [Cygorek et al. 2022], highlighting the persistent advances of classical algorithms.

Chapter 6

Perspectives and Future Directions

In this thesis, we operated a bosonic quantum simulator for two model molecular simulation tasks in very different regimes. Our ability to do this with very high fidelity speaks to the sophistication of the hardware via virtue of its simplicity — we are able to accurately model the system with a simple low energy Hamiltonian within the domain of our control via microwave drives. A theme to keep in mind is the control of higher-order Hamiltonian terms that emerge using this approach as one moves towards manipulating states with larger photon numbers [Zhang et al. 2019; Zhang et al. 2022].

What, then, lies ahead? The promise of analog quantum simulation suggests that we may be able to study systems beyond the scope of classical computation without the need for error correction, provided that the simulator can be accurately controlled on a larger scale. The hardware efficiency of using multilevel bosonic systems is certainly helpful from that perspective. However, we will likely need to demonstrate additional nonlinear control knobs in order to access interesting regimes.

6.1   Molecular anharmonicity

A clear next step to address for molecular dynamics simulations are anharmonicities in the potential energy surface. A brute force approach would be to Taylor expand a real potential energy surface of interest around a local minimum and translate the resulting Hamiltonian into the appropriate creation and annihilation operators of a bosonic simulator. We can take

the concrete example of a Morse potential:

$$V(q) = D(e^{-aq} - 1)^2 \tag{6.1}$$

where we have taken the minimum of the potential to be at $q = 0$. The parameter D determines the depth of the well and a determines the width of the potential. We can re-cast the potential and write the Hamiltonian in the following way:

$$\hat{H}_{\text{morse}} = \hbar\omega\left(\frac{\hat{p}^2}{2} + \frac{1}{2\alpha^2}\left(e^{-\alpha\hat{q}} - \hat{\mathbf{1}}\right)^2\right) \tag{6.2}$$

$$= \hbar\omega\left(\frac{\hat{p}^2}{2} + \frac{1}{2\alpha^2}\left(e^{-2\alpha\hat{q}} - 2e^{-\alpha\hat{q}} + \hat{\mathbf{1}}\right)\right) \tag{6.3}$$

with the dimensionless parameter $\alpha = a\sqrt{\hbar/m\omega}$. In the basis of dimensionless creation and annihilation operators $\hat{q} = \frac{1}{\sqrt{2}}(\hat{a} + \hat{a}^\dagger)$ and $\hat{p} = \frac{i}{\sqrt{2}}(\hat{a}^\dagger - \hat{a})$, we have:

$$\hat{H}_{\text{morse}} = \hbar\omega\left(\frac{\hat{p}^2}{2} + \frac{1}{2\alpha^2}\left(e^{-\sqrt{2}\alpha\hat{a}^\dagger}e^{-\sqrt{2}\alpha\hat{a}}e^{-\alpha^2\hat{\mathbf{1}}} - 2e^{-\alpha\hat{a}^\dagger/\sqrt{2}}e^{-\alpha\hat{a}/\sqrt{2}}e^{-\alpha^2\hat{\mathbf{1}}/4} + \hat{\mathbf{1}}\right)\right) \tag{6.4}$$

We can use the Taylor expansion of an exponential term to quartic order in some small parameter β:

$$e^{\beta\hat{a}^{(\dagger)}} \approx \hat{\mathbf{1}} - \beta\hat{a}^{(\dagger)} + \frac{\beta^2}{2}\hat{a}^{(\dagger)2} - \frac{\beta^3}{6}\hat{a}^{(\dagger)3} + \frac{\beta^4}{24}\hat{a}^{(\dagger)4} + \mathcal{O}(\beta^5) \tag{6.5}$$

and expand the full Hamiltonian to second order in α. Taking care to normal-order all of the operators, we arrive at:

$$\hat{H}_{\text{morse}} \approx \hbar\omega\left(\hat{a}^\dagger\hat{a} - \alpha\hat{V}_1 + \alpha^2\hat{V}_2\right) \tag{6.6}$$
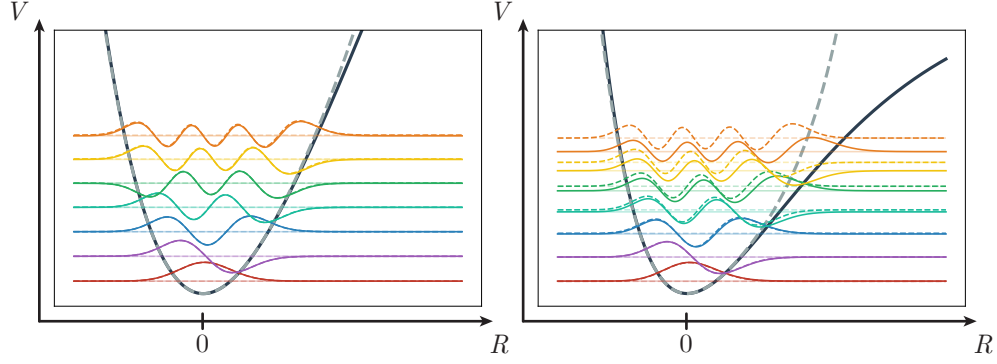
Figure 6.1 | Approximating a Morse potential up to 4th order. Morse potential and exact eigenfunctions for V_{morse} with $\alpha = 0.1$ (left) and 0.2 (right) depicted with solid lines. Dashed lines indicate the corresponding 4th order Taylor expansion.

where

$$
\hat{V}_1 = \left(\sqrt{2} - \frac{1}{\sqrt{2}} \right)(\hat{a} + \hat{a}^\dagger)
$$
$$
+ \left(\sqrt{2} - \frac{1}{\sqrt{2}} \right)(\hat{a}^{\dagger 2}\hat{a} + \hat{a}^\dagger \hat{a}^2)
$$
$$
+ \left(\frac{\sqrt{2}}{3} - \frac{1}{6\sqrt{2}} \right)(\hat{a}^3 + \hat{a}^{\dagger 3})
$$
$$
\hat{V}_2 = \left(2 - \frac{1}{4} \right)(\hat{a}^\dagger \hat{a})
$$
$$
+ \left(1 - \frac{1}{8} \right)(\hat{a}^2 + \hat{a}^{\dagger 2})
$$
$$
+ \left(1 - \frac{1}{8} \right)(\hat{a}^{\dagger 2}\hat{a}^2)
$$
$$
+ \left(\frac{2}{3} - \frac{1}{12} \right)(\hat{a}^{\dagger 3}\hat{a} + \hat{a}^\dagger \hat{a}^3)
$$
$$
+ \left(\frac{1}{6} - \frac{1}{24} \right)(\hat{a}^4 + \hat{a}^{\dagger 4})
$$

We see that the resulting combination of creation and annihilation operators are not so simple, given that it involves all third and fourth order combinations of $\hat{a}$ and $\hat{a}^\dagger$ (even the non-excitation-conserving ones). This is due to the requirement of having only nonlinear potential energy while retaining a quadratic kinetic energy. Engineering these terms simultaneously in the correct proportions is certainly a challenging task, especially as enacting 4th order terms using parametric driving will require the use of a 5th order nonlinearity. Using Trotterization schemes instead would avoid the need to invoke all the terms at once,

though this may lead to larger errors owing to longer sequences. As one can see in Fig. 6.1, however, even a 4th order expansion becomes a poor approximation as the potential becomes visibly anharmonic, necessitating the inclusion of even higher order terms.

Coming up with alternative approaches to implement controllable nonlinear Hamiltonians is an interesting research question. One can perhaps start to think outside the box; for example, it has been shown that a 1D Morse potential can be exactly cast using two bosonic modes under the Schwinger representation [Alhassid, Iachello, and Gürsey 1983]. Can this serve as a useful starting point for adding more degrees of freedom? Alternatively, perhaps it is possible to engineer Josephson circuits with a number of external control knobs to directly shape the potential of a few degrees of freedom to match that of a target molecule [Gunnarsson et al. 2008; Frattini et al. 2017; Kou et al. 2017].

6.2   Strongly interacting bosons on a lattice

Another promising direction to pursue are lattice models involving bosons such as the Bose-Hubbard model and extended versions thereof, initially introduced in [Gersch and Knollman 1963]. To properly contextualize these models requires unlocking the entire field of condensed matter physics (we refer the interested reader to [Girvin and Yang 2019]), and as such we simply discuss high-level points from the perspective of implementing a model bosonic Hamiltonian. The Bose-Hubbard Hamiltonian can be expressed as:

$$\mathcal{H}_{\text{BH}}/\hbar = -\mu \sum_i \hat{n}_i - \sum_{ij} t_{ij} \hat{a}_i^\dagger \hat{a}_j + \frac{U}{2} \sum_i \hat{a}_i^\dagger \hat{a}_i^\dagger \hat{a}_i \hat{a}_i \tag{6.7}$$

where μ is a chemical potential, $\{t_{ij}\}$ are nearest-neighbor tunneling energies, and U is an on-site interaction energy. The phase diagram of the Bose-Hubbard model has been (and continues to be) studied extensively, and has been numerically shown to reproduce a quantum phase transition between a superfluid and insulating state in one [Kühner and Monien 1998], two [Elstner and Monien 1999], and three dimensions [Capogrosso-Sansone, Prokof'Ev, and Svistunov 2007].

Atoms trapped in optical lattices have served as a wonderful platform for investigating

such models. Experimentally, the seminal work of [Greiner et al. 2002] observed the super-fluid to Mott insulator transition in a 3D Bose-Einstein condensate of 2×10^5 atoms, with single-site resolution being achieved roughly a decade later [Bakr et al. 2009; Sherson et al. 2010]. In parallel, the development of reconfigurable large scale optical tweezers [Dumke et al. 2002; Nogrette et al. 2014] has further expanded the flexibility and capability of atomic systems for quantum simulation.

The use of individually controllable atoms to model real materials is interesting not only from the perspective of going beyond the capabilities of going beyond classical computing, but also for creating and observing quantum mechanical phenomena in fully controlled systems. Following the spirit of this thesis, this begs the question: can one use create such interesting phases of matter with photons? And would doing so unlock new physics that would otherwise be inaccessible? The answers to these questions motivates the development of *topological photonics* [Ozawa et al. 2019] which holds promise for a wide range of applications and exploring correlated many-body physics.

Two of the primary challenges in this direction are that: 1) photons do not naturally interact with each other and 2) photons tend to spontaneously emit, violating the conservation of particle number. Circuit QED can facilitate these challenges by enabling photons to strongly interact via the Josephson nonlinearity while being confined to long-lived microwave resonators, and offering reservoir engineering schemes to stabilize many-body states of interest. The addition of chirality, i.e. allowing photons to acquire a nontrivial phase upon enclosing a closed loop in the lattice, enables the generation of fractional quantum Hall states of light. These ideas have been explored using superconducting circuits [Anderson et al. 2016; Roushan et al. 2017; Owens et al. 2018; Ma et al. 2019; Yanay et al. 2020; Owens et al. 2021], though the path forward faces a number of interesting challenges [Kurilovich et al. 2021] which will be sure to inspire innovative solutions and new directions.

We briefly present an architecture that is amenable to this research direction in Fig. 6.2. A 3x3 array of microwave cavities serves as the primary lattice sites, and individual transmons couple to each lattice site to provide the requisite nonlinearity as well as site-resolved state preparation and measurement capabilities. This architecture is also amenable
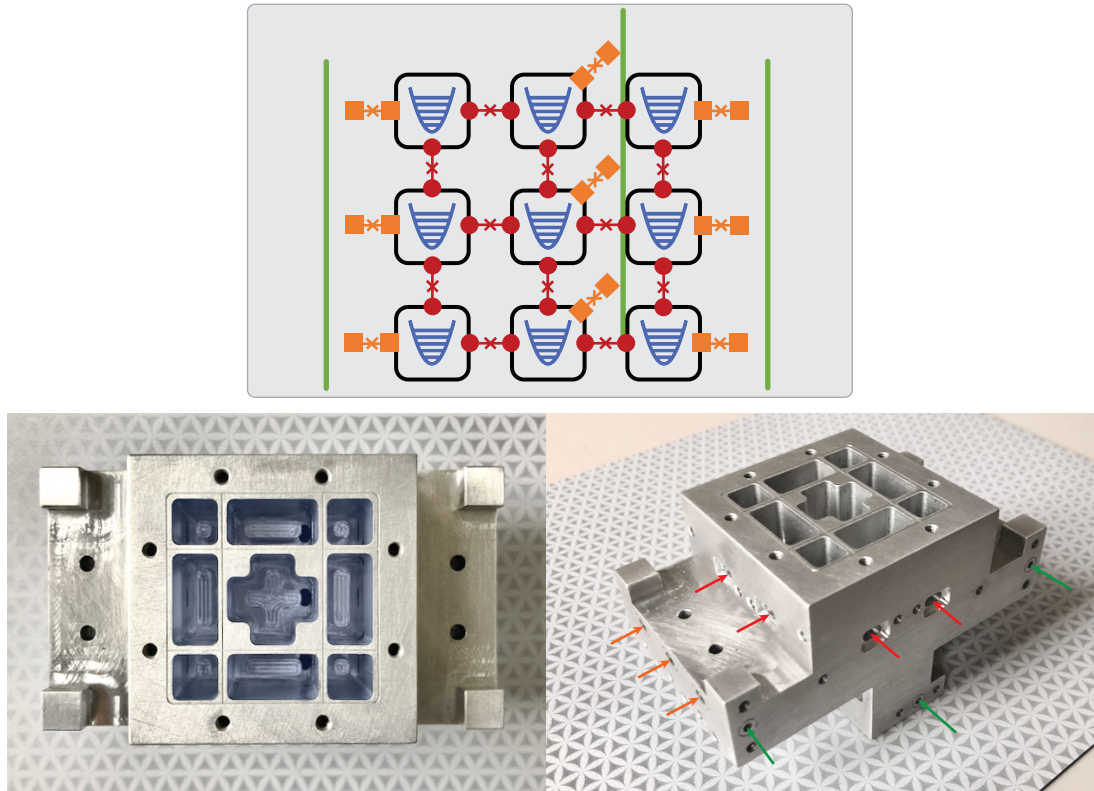
Figure 6.2 | **Architecture and prototype of a 3x3 array of cavity modes.** Each cavity mode couples to its nearest neighbor via coupler transmons (red) and individually to ancilla transmons (orange). Ancilla transmons are capacitively coupled to feedlines (green) for measurement in a hanger style configuration. The shape of the post cavities are chosen to facilitate tunnel openings for coupler transmons while keeping package modes high in frequency and outside the band of the lattice.

to stabilization schemes that require a "shadow" lattice with respect to the primary lattice [Kapit, Hafezi, and Simon 2014]. Coupler transmons bridge nearest-neighbor cavities and can be used to parametrically activate tunneling energies with full phase control.

A number of challenges need to be addressed if one is to move forward with this architecture. Delivering pumps in a controlled and localized manner to the desired junction(s) is critical — any unwanted crosstalk inhibits the ability to effectively calibrate the entire system. Higher-order terms invoked via parametric driving must be suppressed, necessitating, in part, a proper choice of frequencies of all the transmon modes. Nevertheless, scaling up is an inevitable step moving forward, and it will be interesting to discover and address the engineering challenges in controlling 3D systems with a larger number of modes.

Appendix A

Unitary transformations

A central tool for analyzing a seemingly complicated time-dependent Hamiltonian is to perform a set of unitary frame transformations to hopefully arrive at a simpler effective Hamiltonian that can be more easily understood. While the physics ultimately remains the same regardless of the choice of frame, the dynamics may qualitatively look different. Moreover, care needs to be taken when applying these transformations; often times approximations are made by neglecting certain terms, but one needs to properly justify these choices.

The general formula for transforming a Hamiltonian $\hat{H}$ via a time-dependent unitary transformation $\hat{U}(t)$ is:

$$\hat{H} \rightarrow \hat{U}\hat{H}\hat{U}^\dagger + i\hbar\dot{\hat{U}}\hat{U}^\dagger \tag{A.1}$$

A.1 Rotating frame transformation

We consider a harmonic oscillator with frequency ω_0 driven at frequency ω_d:

$$\hat{H}/\hbar = \underbrace{\omega_0\hat{a}^\dagger\hat{a}}_{\hat{H}_0} + \underbrace{2\varepsilon\cos(\omega_d t + \varphi_d)(\hat{a} + \hat{a}^\dagger)}_{\hat{H}_d} \tag{A.2}$$

We choose a general frame rotating at frequency ω and apply $\hat{U}(t) = e^{i\omega\hat{a}^\dagger\hat{a}t}$. We can first determine how $\hat{a}$ transforms:

$$
\begin{aligned}
\hat{U}\hat{a}\hat{U}^\dagger &= e^{i\omega\hat{a}^\dagger\hat{a}t}\hat{a}e^{-i\omega\hat{a}^\dagger\hat{a}t} \\
&= \hat{a} + (i\omega t)\underbrace{[\hat{a}^\dagger\hat{a}, \hat{a}]}_{-\hat{a}} + \frac{(i\omega t)^2}{2!}[\hat{a}^\dagger\hat{a}, [\hat{a}^\dagger\hat{a}, \hat{a}]] + ... \\
&= \hat{a} - i\omega t\hat{a} + \frac{(-i\omega t)^2}{2!}\hat{a} + ... \\
&= \hat{a}e^{-i\omega t}
\end{aligned}
\tag{A.3}
$$

From this, we can immediately transform $\hat{H}_0$ and $\hat{H}_d$:

$$
\begin{aligned}
\hat{H}_0 &\to \hat{H}_0 \\
\hat{H}_d &\to 2\hbar\varepsilon\cos(\omega_d t + \varphi_d)(\hat{a}e^{-i\omega t} + \hat{a}^\dagger e^{i\omega t})
\end{aligned}
\tag{A.4}
$$

Finally, we can evaluate the derivative term:

$$
i\hbar\dot{\hat{U}}\hat{U}^\dagger = i\hbar(i\omega t)\hat{U}\hat{U}^\dagger = -\hbar\omega
\tag{A.5}
$$

Putting it all together, we arrive at:

$$
\begin{aligned}
\hat{H}/\hbar &= (\omega_0 - \omega)\hat{a}^\dagger\hat{a} + \varepsilon(e^{i(\omega_d t+\varphi)} + e^{-i(\omega_d t+\varphi)})(\hat{a}e^{-i\omega t} + \hat{a}^\dagger e^{i\omega t}) \\
&\approx (\omega_0 - \omega)\hat{a}^\dagger\hat{a} + \varepsilon(\hat{a}e^{-i[(\omega-\omega_d)t+\varphi]} + \hat{a}^\dagger e^{i[(\omega-\omega_d)t+\varphi]})
\end{aligned}
\tag{A.6}
$$

where we have neglected terms rotating at $\omega + \omega_d$, which is valid in this case if $|\omega + \omega_d| \gg |\omega_0 - \omega|$. This is called the *rotating wave approximation* (RWA), and amounts to neglecting terms that are very off resonant.

A.2 Displacement transformation

All of the parametric operations used in this thesis involve driving our circuit QED system. The displacement transformation is useful for working in a frame that tracks with some average and often uninteresting trajectory, leaving behind the interesting dynamics that we

aim to engineer.

The basic form of the displacement transformation is $\hat{U} = e^{\xi(t)\hat{a}^\dagger - \xi^*(t)\hat{a}}$, which transforms $\hat{a}$ as:

$$
\begin{aligned}
\hat{U}\hat{a}\hat{U}^\dagger &= e^{\xi(t)\hat{a}^\dagger - \xi^*(t)\hat{a}}\hat{a}e^{\xi^*(t)\hat{a}^\dagger - \xi(t)\hat{a}} \\
&= \hat{a} + \underbrace{[\xi(t)\hat{a}^\dagger - \xi^*(t)\hat{a}, \hat{a}]}_{-\xi(t)}
\end{aligned}
\tag{A.7}
$$

where the higher order terms vanish as they involve commutators with scalars. The derivative term gives:

$$
i\hbar\dot{\hat{U}}\hat{U}^\dagger = i\hbar\big(\dot{\xi}(t)\hat{a}^\dagger - \dot{\xi}^*(t)\hat{a}\big)\hat{U}\hat{U}^\dagger
\tag{A.8}
$$

In practice, $\xi(t)$ is typically chosen to eliminate the drive term.

We take the time-independent example of a simple cavity driven off-resonance and working in the frame of the drive (following Eq. A.6 above). In this case, it is sufficient to choose $\xi(t) = \xi = \frac{\varepsilon}{\Delta}$ (note that the derivative term vanishes):

$$
\begin{aligned}
\hat{H}/\hbar &= \Delta\hat{a}^\dagger\hat{a} + \varepsilon(\hat{a} + \hat{a}^\dagger) \\
&\rightarrow \Delta(\hat{a}^\dagger - \xi^*)(\hat{a} - \xi) + \varepsilon(\hat{a} + \hat{a}^\dagger - \xi - \xi^*) \\
&= \Delta\hat{a}^\dagger\hat{a}
\end{aligned}
\tag{A.9}
$$

where $\Delta = \omega_0 - \omega_d$. Examples of the time-dependent case are used in Appendix B.

Appendix B

Parametric operations

B.1 Single-mode squeezing

We begin with Eq. 4.11 describing a transmon coupled to a cavity via the Josephson non-linearity under the presence of two drives on the transmon mode:

$$\hat{H}/\hbar = \omega_t \hat{t}^\dagger \hat{t} + \omega_a \hat{a}^\dagger \hat{a} - \frac{E_J}{4!}\left(\varphi_t(\hat{t} + \hat{t}^\dagger) + \varphi_a(\hat{a} + \hat{a}^\dagger)\right)^4 + \underbrace{\sum_{i=1}^{2} 2\varepsilon_i \cos(\omega_i t + \varphi_i)(\hat{t} + \hat{t}^\dagger)}_{f_0(t)} \quad \text{(B.1)}$$

We choose to work in the frame of the cavity and transmon $\hat{U}(t) = e^{i\omega_a \hat{a}^\dagger \hat{a} t}e^{i\omega_t \hat{t}^\dagger \hat{t} t}$:

$$\hat{H}/\hbar = -\frac{E_J}{4!}\left(\varphi_t(\hat{t}e^{-i\omega_t t} + \hat{t}^\dagger e^{i\omega_t t}) + \varphi_a(\hat{a}e^{-i\omega_a t} + \hat{a}^\dagger e^{i\omega_a t})\right)^4 + \underbrace{f_0(t)(\hat{t}e^{-i\omega_t t} + \hat{t}^\dagger e^{i\omega_t t})}_{\hat{f}_1(t)} \quad \text{(B.2)}$$

Our goal at this stage is to perform a displacement transformation to eliminate $\hat{f}_1(t)$. The condition for doing so is:

$$-i\left(\dot{\xi}(t)\hat{t}^\dagger - \dot{\xi}^*(t)\hat{t}\right) = \hat{f}_1(t) \quad \text{(B.3)}$$

The full expression for $\hat{f}_1(t)$ is:

$$\hat{f}_1(t) = \hat{t}\left(\varepsilon_1 e^{i[(\omega_1 - \omega_t)t + \varphi_1]} + \varepsilon_2 e^{i[(\omega_2 - \omega_t)t + \varphi_2]}\right) + \hat{t}^\dagger\left(\varepsilon_1 e^{-i[(\omega_1 - \omega_t)t + \varphi_1]} + \varepsilon_2 e^{-i[(\omega_2 - \omega_t)t + \varphi_2]}\right)$$

$$\text{(B.4)}$$

neglecting terms that rotate at $\omega_{1/2} + \omega_t$. By defining $\Delta_{1/2} = \omega_{1/2} - \omega_t$ and solving Eq. B.3, we get an expression for the dimensionless field trajectory of the transmon:

$$\xi(t) = -\xi_1 e^{-i\varphi_1} e^{-i\Delta_1 t} - \xi_2 e^{-i\varphi_2} e^{-i\Delta_2 t} \tag{B.5}$$

where $\xi_i = \frac{\varepsilon_i}{\Delta_i}$ for $i \in \{1, 2\}$. Under the displacement transformation, the transmon annihilation operator transforms as $\hat{t} \to \hat{t} + \xi(t)$, resulting in:

$$\hat{H}/\hbar = -\frac{E_J}{4!} \left(\varphi_t \big((\hat{t} + \xi(t)) e^{-i\omega_t t} + (\hat{t}^\dagger + \xi^*(t)) e^{i\omega_t t} \big) + \varphi_a (\hat{a} e^{-i\omega_a t} + \hat{a}^\dagger e^{i\omega_a t}) \right)^4 \tag{B.6}$$

Finally, by choosing $\omega_1 = \omega_a - \delta$ and $\omega_2 = \omega_a + \delta$, we can expand the cosine potential and keep terms that do not rotate. This finally gives us Eq. 4.12:

$$\hat{H}_{\text{sq}}/\hbar = |\xi_1|^2 (2\chi_{tt}\hat{t}^\dagger\hat{t} + \chi_{ta}\hat{a}^\dagger\hat{a}) + |\xi_2|^2 (2\chi_{aa}\hat{a}^\dagger\hat{a} + \chi_{at}\hat{t}^\dagger\hat{t}) + g_{\text{sq}}(e^{i\theta_{\text{sq}}}\hat{a}^2 + e^{-i\theta_{\text{sq}}}\hat{a}^{\dagger 2}) \tag{B.7}$$

where $\theta_{\text{sq}} = \varphi_1 + \varphi_2$.

B.2 Conditional displacement with a Rabi qubit encoded in a multi-level transmon

We begin with the static Hamiltonian of a transmon mode $\hat{q}$ dispersively coupled to a cavity mode $\hat{c}$:

$$\hat{H}_{\text{static}}/\hbar = \omega_c \hat{c}^\dagger\hat{c} + \omega_q \hat{q}^\dagger\hat{q} - \frac{\alpha_q}{2}\hat{q}^\dagger\hat{q}^\dagger\hat{q}\hat{q} - \chi\hat{c}^\dagger\hat{c}\hat{q}^\dagger\hat{q} \tag{B.8}$$

where α_q is the transmon anharmonicity and χ is the dispersive shift. At a high level, we will see that the conditional displacement interaction arises by transforming the cross-Kerr interaction between the transmon and the cavity. Thus, our approach will be to consider how driving each mode transforms the static interaction. Specifically, we drive the system with one tone coupled to the transmon and two coupled to the cavity:

$$\hat{H}_d/\hbar = 2\varepsilon_R \cos[(\omega_q + \Delta_R)t](\hat{q} + \hat{q}^\dagger) - 2i\varepsilon_1 \sin(\omega_1 t + \varphi_1)(\hat{c} - \hat{c}^\dagger) - 2i\varepsilon_2 \sin(\omega_2 t + \varphi_2)(\hat{c} - \hat{c}^\dagger) \tag{B.9}$$

such that the full system Hamiltonian is described by $\hat{H} = \hat{H}_{\text{static}} + \hat{H}_d$. For convenience, we re-group the terms such that we can write $\hat{H} = \hat{H}_q(\hat{q}, \hat{q}^\dagger) + \hat{H}_c(\hat{c}, \hat{c}^\dagger) + \hat{H}_{\text{int}}$, where $\hat{H}_{\text{int}}/\hbar = -\chi \hat{c}^\dagger \hat{c} \hat{q}^\dagger \hat{q}$. We first go into the rotating frame of the transmon drive via $\hat{U} = e^{i(\omega_q + \Delta_R)t\hat{q}^\dagger \hat{q}}$:

$$\hat{H}/\hbar = \underbrace{-\Delta_R \hat{q}^\dagger \hat{q} - \frac{\alpha_q}{2}\hat{q}^\dagger \hat{q}^\dagger \hat{q}\hat{q} + \varepsilon_R(\hat{q} + \hat{q}^\dagger)}_{\hat{H}_{\text{q}}/\hbar} + \hat{H}_c/\hbar - \chi \hat{c}^\dagger \hat{c} \hat{q}^\dagger \hat{q} \tag{B.10}$$

noting that we have performed the rotating-wave approximation (RWA) and discarded terms rotating at $\mathcal{O}(\omega_q)$. Furthermore, the cross-Kerr term remains unaffected since it is proportional to $\hat{q}^\dagger \hat{q}$. Now, we diagonalize $\hat{H}_q$ and re-express it in the resulting eigenbasis:

$$\hat{H}_{\text{q}}/\hbar = \sum_i \epsilon_i \ket{i} \bra{i} \tag{B.11}$$

where we label $i \in \{+, -, \tilde{f}, ...\}$ in correspondence with the fact that we will be working in a regime where the two lowest driven eigenstates strongly resemble those of a standard qubit that is driven on resonance, but now incorporate a weak dressing with higher levels of the transmon. We identify the Rabi frequency to be the energy difference between the lowest two eigenstates $\epsilon_+ - \epsilon_- = \Omega_R$ and define an effective anharmonicity as $\epsilon_- - \epsilon_{\tilde{f}} = \Omega_R + \tilde{\alpha}$. At this stage, we turn to numerics and construct a unitary basis transformation between the undriven and driven transmon eigenstates for a finite truncation of the transmon Hilbert space. We then re-express the cross-Kerr interaction in the driven basis, giving us:

$$\hat{H}/\hbar = \sum_i \epsilon_i \ket{i} \bra{i} + \hat{H}_c/\hbar - \chi \hat{c}^\dagger \hat{c} \sum_{jk} u_{jk} \ket{j} \bra{k} \tag{B.12}$$

We can further simplify this by going into the frame of the driven transmon $\hat{U} = e^{i\hat{H}_{\text{Rabi}}t/\hbar}$ which performs the transformations $\ket{j} \to e^{i\epsilon_j t/\hbar} \ket{j}$, resulting in:

$$\hat{H}/\hbar = \hat{H}_c/\hbar - \chi \hat{c}^\dagger \hat{c} \underbrace{\sum_{jk} u_{jk} e^{i(\epsilon_j - \epsilon_k)t/\hbar} \ket{j} \bra{k}}_{\hat{q}^\dagger \hat{q}} \tag{B.13}$$

where $u_{jk} = u_{kj}^*$. We consider the terms associated with the lowest three levels explicitly:

$$
\begin{aligned}
\hat{q}^\dagger \hat{q} = {}& u_{++} |+\rangle \langle+| + u_{--} |-\rangle \langle-| + u_{\tilde{f}\tilde{f}}|\tilde{f}\rangle\langle\tilde{f}| + u_{+-}e^{i\Omega_R t} |+\rangle \langle-| + u_{-+}e^{-i\Omega_R t} |-\rangle \langle+| \\
& + u_{-\tilde{f}}e^{i(\Omega_R+\tilde{\alpha})t} |-\rangle \langle\tilde{f}| + u_{\tilde{f}-}e^{-i(\Omega_R+\tilde{\alpha})t}|\tilde{f}\rangle \langle-| \\
& + u_{+\tilde{f}}e^{i(2\Omega_R+\tilde{\alpha})t} |+\rangle \langle\tilde{f}| + u_{\tilde{f}+}e^{-i(2\Omega_R+\tilde{\alpha})t}|\tilde{f}\rangle \langle+|
\end{aligned}
$$

$$(B.14)$$

At this stage, we pause and turn to simplify $\hat{H}_c$. First, we choose to parameterize the two drive frequencies $\omega_{1/2} = \omega_c - \Delta_c \mp \Omega_R$. By going into the rotating frame at the average of the drive frequencies $\hat{U} = e^{i(\omega_c-\Delta_c)t\hat{c}^\dagger\hat{c}}$, we arrive at:

$$
\hat{H}/\hbar = \hat{H}_{\text{int}}/\hbar + \Delta_c\hat{c}^\dagger\hat{c} - \varepsilon_1(\hat{c}e^{-i\Omega_R t+i\varphi_1}+\hat{c}^\dagger e^{i\Omega_R t-i\varphi_1}) - \varepsilon_2(\hat{c}e^{i\Omega_R t+i\varphi_2}+\hat{c}^\dagger e^{-i\Omega_R t-i\varphi_2}) \quad (B.15)
$$

Finally, we assume that the drive strengths are equal $\varepsilon_2 = -\varepsilon_1 = \varepsilon$ and parameterize the drive phases as their sum and differential components $\varphi_\Sigma = (\varphi_1 + \varphi_2)/2$ and $\varphi_\delta = (\varphi_1 - \varphi_2)/2$. This allows us to further simplify our Hamiltonian to:

$$
\hat{H}/\hbar = \hat{H}_{\text{int}}/\hbar + \Delta_c\hat{c}^\dagger\hat{c} - 2i\varepsilon\sin(\Omega_R t - \varphi_\delta)(\hat{c}e^{i\varphi_\Sigma} - \hat{c}^\dagger e^{-i\varphi_\Sigma}) \quad (B.16)
$$

We can observe here that the sum phase of the two sidebands contributes simply as a static rotation of $\hat{c}$, therefore we can always align to this frame by experimentally adjusting this phase. Hence, we will set $\varphi_\Sigma = 0$ here on out to simplify our expressions. At this stage, we aim to eliminate this time-dependent drive term by performing a displacement transformation $\hat{U} = e^{\xi(t)\hat{c}^\dagger - \xi^*(t)\hat{c}}$. This is achieved by choosing $\xi(t) = \frac{2\varepsilon}{\Omega_R}\cos(\Omega_R t + \varphi_\delta) =$

$\xi_0(e^{i(\Omega_R t+\varphi_\delta)}+e^{-i(\Omega_R t+\varphi_\delta)})$ where $\xi_0 = \frac{\varepsilon}{\Omega_R}$, which also transforms $\hat{c} \to \hat{c} + \xi(t)$. This gives:

$$
\begin{aligned}
\hat{H}/\hbar &= \Delta_c(\hat{c}^\dagger + \xi^*(t))(\hat{c} + \xi(t)) - \chi(\hat{c}^\dagger + \xi^*(t))(\hat{c} + \xi(t))\sum_{jk} u_{jk} e^{i(\epsilon_j-\epsilon_k)t/\hbar}\,|j\rangle\langle k| \\[1mm]
&= \Delta_c(\hat{c}^\dagger\hat{c} + \xi(t)(\hat{c} + \hat{c}^\dagger) + \xi_0^2) \\
&\quad - \chi\left(\hat{c}^\dagger\hat{c} + \xi_0(e^{i(\Omega_R t+\varphi_\delta)}+e^{-i(\Omega_R t+\varphi_\delta)})(\hat{c} + \hat{c}^\dagger) + \xi_0^2\right)\sum_{jk} u_{jk} e^{i(\epsilon_j-\epsilon_k)t/\hbar}\,|j\rangle\langle k|
\end{aligned}
$$

(B.17)

By substituting the expansion for $\hat{q}^\dagger\hat{q}$, discarding terms that rotate at Ω_R and higher, and neglecting constant offsets, we are left with an effective static interaction Hamiltonian:

$$
\begin{aligned}
\hat{H}/\hbar &= \Delta_c\hat{c}^\dagger\hat{c} - \chi\xi_0 u_{+-}(e^{-i\varphi_\delta}\,|+\rangle\langle -| + e^{i\varphi_\delta}\,|-\rangle\langle +|)(\hat{c} + \hat{c}^\dagger) \\
&\quad - \chi\hat{c}^\dagger\hat{c}(u_{++}\,|+\rangle\langle +| + u_{--}\,|-\rangle\langle -| + u_{\tilde{f}\tilde{f}}|\tilde{f}\rangle\langle\tilde{f}|)
\end{aligned}
$$

(B.18)

Importantly, this approximation requires larger Rabi frequencies as we drive harder to induce larger desired interaction strengths (see subsection A. for a more detailed analysis). Finally, by neglecting the final term (see subsection B.), we arrive at the conditional displacement Hamiltonian between the transmon and one cavity mode:

$$
\hat{H}/\hbar = \Delta_c\hat{c}^\dagger\hat{c} - g(\cos(\varphi_\delta)\hat{\sigma}_x + \sin(\varphi_\delta)\hat{\sigma}_y)(\hat{c} + \hat{c}^\dagger) \tag{B.19}
$$

where $g = \chi\xi_0 u_{+-} \approx \frac{\chi\xi_0}{2}$ and we have defined our Pauli operators such that $\hat{\sigma}_z = |+\rangle\langle +| - |-\rangle\langle -|$. Here, we have formally identified the qubit that we will use within the larger driven transmon Hilbert space. As we can see, the coupling axis of the qubit fully depends on the differential phase φ_δ of the cavity sidebands relative to the qubit phase (which we have defined as zero here), which can be easily adjusted experimentally without invoking additional Hamiltonian terms. Note that throughout our derivations, we have assumed no accidental frequency collisions that bring unintended Hamiltonian terms into resonance.

This scheme extends relatively straightforwardly to multiple cavity modes dispersively coupled to the same transmon. Incorporating a pair of sidebands on each additional cavity is sufficient to activate a conditional displacement involving the driven transmon, as long

as the resonance condition is satisfied. It is also worth noting that we have assumed that each sideband couples only to a single cavity mode - in practice, finite crosstalk complicates the calibration procedure of activating all sidebands together. In our experiment, we enact the aforementioned Hamiltonian Eq. (B.19) for two cavity modes $\hat{c} \in \{\hat{a}, \hat{b}\}$ coupled to orthogonal axes of the qubit.

B.2.1 Optimizing the static cross-Kerr

Here, we consider (Eq. B.17) and ask the questions: How large do we need the Rabi frequency to be in order to safely discard all the rotating terms? Does the answer to this question inform any design choices with regard to our static Hamiltonian? To answer this question, we consider all of the different terms that rotate at Ω_R, neglecting any phases:

$$\left(\Delta_c \xi_0 (\hat{c} + \hat{c}^\dagger) - \chi u_{+-} \hat{c}^\dagger \hat{c} \hat{\sigma}_\mp - \chi \xi_0^2 u_{+-} \hat{\sigma}_\mp \right) e^{\pm i \Omega_R t} \tag{B.20}$$

Note that there are also terms that rotate at $\tilde{\alpha}, 2\Omega_R, \Omega_R + \tilde{\alpha}, 2\Omega_R + \tilde{\alpha}$, and $3\Omega_R + \tilde{\alpha}$, but since the prefactors will all be of the same order, we consider the smallest rotating frequency for the most stringent condition. Importantly, we also require that $\tilde{\alpha} > \Omega_R$, otherwise other terms involving $|\tilde{f}\rangle$ will be activated and we can no longer restrict ourselves to a qubit subspace. This sets a limit on how large of a Rabi frequency can be used for a fixed anharmonicity α_q. The above terms reveal that our conditions for the RWA are:

$$\Omega_R \gg \{\Delta_a |\xi_0 \langle (\hat{c} + \hat{c}^\dagger) \rangle|, \frac{\chi}{2} \langle \hat{c}^\dagger \hat{c} \rangle, \frac{\chi}{2} \xi_0^2 \} \tag{B.21}$$

which notably depends on the state of the cavity. It is clear from this that as the conditional displacement interaction strength $g \approx \frac{\chi \xi_0}{2}$ increases, the approximation becomes less valid. However, we can instead rewrite the condition for a fixed g:

$$\Omega_R \gg \{\Delta_a |\xi_0 \langle (\hat{c} + \hat{c}^\dagger) \rangle|, \frac{g}{\xi_0} \langle \hat{c}^\dagger \hat{c} \rangle, g \xi_0 \} \tag{B.22}$$

which reveals that there is indeed an optimal value for ξ_0 given a fixed g. For considering photon numbers $\langle \hat{c}^\dagger \hat{c} \rangle \sim \mathcal{O}(1)$ and $g \approx \Delta_c$, we best satisfy all these conditions by choosing
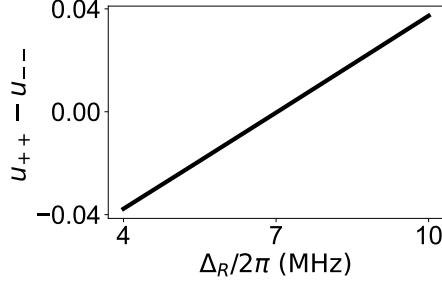
Figure B.1 | Optimizing the static detuning. By numerically diagonalizing $\hat{H}_q/\hbar$ for various values of Δ_R, we can plot the dimensionless factor that contributes to the residual cross-Kerr for $\Omega_R/2\pi = 80$ MHz and $\alpha_q/2\pi = 244$ MHz. We find an optimal value of $\Delta_R/2\pi \approx 7$ MHz.

$\xi_0 \approx 1$. This, in turn for a fixed g, suggests that we should roughly target a static cross-Kerr strength of $\chi \approx 2g$.

B.2.2 Choice of static detuning of the Rabi drive

The final term in Eq. (B.18) represents an effective cross-Kerr interaction between cavity photons and the driven transmon eigenstates. For a true two-level system driven on resonance, which is a good approximation for transmons in the regime that the Rabi frequency is much weaker than the anharmonicity $\Omega_R \ll \alpha_q$, one finds that $u_{++} = u_{--} = 1/2$ which results in a static frequency shift of the cavity and hence a nulled cross-Kerr. As the Rabi frequency Ω_R approaches the anharmonicity α_q, however, $u_{++} \neq u_{--}$ for a drive that is on resonance owing to the hybridization of the driven eigenstates with higher energy levels of the transmon. This results in a residual cross-Kerr which can be interpreted as a slight shift in the Rabi frequency due to the presence of photons in the cavity. This is problematic as it both changes the resonance condition of the interaction and biases our measurement scheme as a function of the cavity photon distribution.

By adding an additional static detuning knob Δ_R on the Rabi drive, we can determine an optimal working configuration that nulls this effective cross-Kerr. We show this optimization in Fig. B.1. The presence of this static detuning thus dictates that we perform an adiabatic preparation of our driven qubit eigenstates. This has the further benefit of eliminating leakage events associated with large Rabi frequencies and finite transmon anharmonicity.

Appendix C

Temperature stabilization

The resonance condition for enacting any interaction involving a Rabi qubit relies on matching the sideband detunings to the Rabi frequency. The Rabi frequency depends linearly on the amplitude of the Rabi drive (roughly speaking, using the two-level approximation that $\Omega_R = \sqrt{\epsilon_R^2 + \Delta_R^2}$ and we operate in a regime where $\epsilon_R \gg \Delta_R$, resulting in $\Omega_R \approx \epsilon_R(1 + \frac{\Delta_R^2}{2\epsilon_R^2}))$, and thus is susceptible to amplitude fluctuations such as those caused by variations in the gain at any stage of our microwave control chain, which include a Marki LXP IQ-mixer and MITEQ low noise amplifier. A dominant source of these variations is due to ambient temperature fluctuations in the lab, for instance owing to the temperature dependence of the nonlinear diodes present in the mixer. To this end, we suppress these fluctuations by anchoring the components (see turquoise box in Fig. 5.4) to a Thorlabs optical breadboard and placing the breadboard in a cardboard box. We then actively stabilize the temperature of the air in the box via an op-amp based PID feedback controller that heats an Ohmite ceramic resistor ($R = 2.5\ \Omega$) based on a differential measurement of the temperature using a 100 kΩ thermistor referenced to a set point. Fig. C.1 shows the typical performance of our stabilization and correlates the temperature variations with the amplitude variations as measured via the Rabi frequency. Over the course of 24 hours, we achieve an absolute temperature stability within 50 mK and a relative amplitude stability of 100 kHz / 72.9 MHz $\approx 10^{-3}$, suggesting that we have a relative amplitude sensitivity of 1% per 500 mK. We note that the timscale for a typical calibration and measurement of a dataset presented in Chapter 5 is roughly a few hours, meaning we can operate in a window
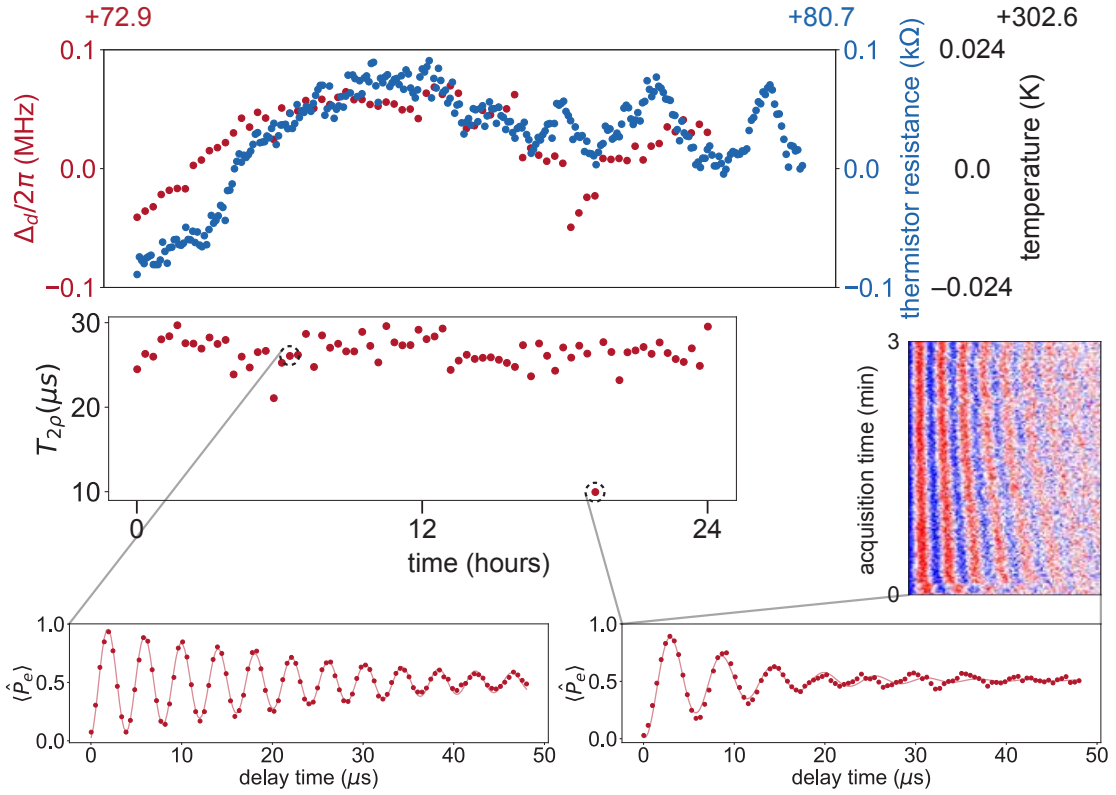
Figure C.1 | Tracking system stability over time. (Top panel) Simultaneous measurements of the Rabi frequency (red circles) and the ambient temperature (blue circles) where the active microwave components are held reveals correlations between temperature drifts and amplitude drifts. (Middle panel) Extracting driven coherences $T_{2\rho}$ suggests a stable amplitude noise spectrum within an acquisition time $\tau_{\mathrm{acq}} = 3$ minutes (bottom left panel: a typical time-domain Ramsey trace), with a single instance where the amplitude drift was large (bottom right panel), as confirmed via looking at the raw data binned 10 shots at a time over τ_{acq}.

where the relative amplitude stability can be much better than 10^{-3}.

References

[1] Aaronson, S. and A. Arkhipov, "The computational complexity of linear optics", in Proceedings of the forty-third annual acm symposium on theory of computing (2011), pp. 333–342.

[2] Alhassid, Y., F. Iachello, and F. Gürsey, "Group theory of the morse oscillator", Chemical Physics Letters **99**, 27–30 (1983).

[3] Anderson, B. M., R. Ma, C. Owens, D. I. Schuster, and J. Simon, "Engineering topological many-body materials in microwave cavity arrays", Physical Review X **6**, 041043 (2016).

[4] Arute, F., K. Arya, R. Babbush, D. Bacon, J. C. Bardin, R. Barends, R. Biswas, S. Boixo, F. G. Brandao, D. A. Buell, et al., "Quantum supremacy using a programmable superconducting processor", Nature **574**, 505–510 (2019).

[5] Aspuru-Guzik, A., A. D. Dutoi, P. J. Love, and M. Head-Gordon, "Simulated quantum computation of molecular energies", Science **309**, 1704–1707 (2005).

[6] Axline, C., M. Reagor, R. Heeres, P. Reinhold, C. Wang, K. Shain, W. Pfaff, Y. Chu, L. Frunzio, and R. J. Schoelkopf, "An architecture for integrating planar and 3d cqed devices", Applied Physics Letters **109**, 042601 (2016).

[7] Axline, C. J., L. D. Burkhart, W. Pfaff, M. Zhang, K. Chou, P. Campagne-Ibarcq, P. Reinhold, L. Frunzio, S. Girvin, L. Jiang, et al., "On-demand quantum state transfer and entanglement between remote microwave cavity memories", Nature Physics **14**, 705–710 (2018).

[8] Axline, C. J., "Building blocks for modular circuit qed quantum computing", PhD thesis (Yale University, 2018).

[9] Bakr, W. S., J. I. Gillen, A. Peng, S. Fölling, and M. Greiner, "A quantum gas microscope for detecting single atoms in a hubbard-regime optical lattice", Nature **462**, 74–77 (2009).

[10] Banaszek, K., C. Radzewicz, K. Wódkiewicz, and J. Krasiński, "Direct measurement of the wigner function by photon counting", Physical Review A **60**, 674 (1999).

[11] Barone, V., J. Bloino, and M. Biczysko, "Vibrationally-resolved electronic spectra in gaussian 09", Revision A **2**, 1–20 (2009).

[12] Bergeal, N., F. Schackert, M. Metcalfe, R. Vijay, V. Manucharyan, L. Frunzio, D. Prober, R. Schoelkopf, S. Girvin, and M. Devoret, "Phase-preserving amplification near the quantum limit with a josephson ring modulator", Nature **465**, 64–68 (2010).

[13] Bernien, H., S. Schwartz, A. Keesling, H. Levine, A. Omran, H. Pichler, S. Choi, A. S. Zibrov, M. Endres, M. Greiner, et al., "Probing many-body dynamics on a 51-atom quantum simulator", Nature **551**, 579–584 (2017).

[14] Bertet, P., A. Auffeves, P. Maioli, S. Osnaghi, T. Meunier, M. Brune, J.-M. Raimond, and S. Haroche, "Direct measurement of the wigner function of a one-photon fock state in a cavity", Physical Review Letters **89**, 200402 (2002).

[15] Blumoff, J. Z., "Multiqubit experiments in 3d circuit quantum electrodynamics", PhD thesis (Yale University, 2017).

[16] Born, M. and R. Oppenheimer, "Zur quantentheorie der molekeln (on the quantum theory of molecules)", Annalen der physik **389**, 457–484 (1927).

[17] Bravyi, S. B. and A. Y. Kitaev, "Fermionic quantum computation", Annals of Physics **298**, 210–226 (2002).

[18] Burkhart, L. D., J. D. Teoh, Y. Zhang, C. J. Axline, L. Frunzio, M. Devoret, L. Jiang, S. Girvin, and R. Schoelkopf, "Error-detected state transfer and entanglement in a superconducting quantum network", PRX Quantum **2**, 030321 (2021).

[19] Burkhart, L. D., "Error-detected networking for 3d circuit quantum electrodynamics", PhD thesis (Yale University, 2020).

[20] Cahill, K. E. and R. J. Glauber, "Density operators and quasiprobability distributions", Physical Review **177**, 1882 (1969).

[21] Capogrosso-Sansone, B., N. Prokof'Ev, and B. Svistunov, "Phase diagram and thermodynamics of the three-dimensional bose-hubbard model", Physical Review B **75**, 134302 (2007).

[22] Car, R. and M. Parrinello, "Unified approach for molecular dynamics and density-functional theory", Physical Review Letters **55**, 2471 (1985).

[23] Chakram, S., K. He, A. V. Dixit, A. E. Oriani, R. K. Naik, N. Leung, H. Kwon, W.-L. Ma, L. Jiang, and D. I. Schuster, "Multimode photon blockade", arXiv preprint arXiv:2010.15292 (2020).

[24] Chakram, S., A. E. Oriani, R. K. Naik, A. V. Dixit, K. He, A. Agrawal, H. Kwon, and D. I. Schuster, "Seamless high-q microwave cavities for multimode circuit quantum electrodynamics", Physical Review Letters **127**, 107701 (2021).

[25] Chou, K. S., "Teleported operations between logical qubits in circuit quantum electrodynamics", PhD thesis (Yale University, 2018).

[26] Clements, W. R., J. J. Renema, A. Eckstein, A. A. Valido, A. Lita, T. Gerrits, S. W. Nam, W. S. Kolthammer, J. Huh, and I. A. Walmsley, "Approximating vibronic spectroscopy with imperfect quantum optics", Journal of Physics B: Atomic, Molecular and Optical Physics **51**, 245503 (2018).

[27] Clerk, A. A., M. H. Devoret, S. M. Girvin, F. Marquardt, and R. J. Schoelkopf, "Introduction to quantum noise, measurement, and amplification", Reviews of Modern Physics **82**, 1155 (2010).

[28] Curtis, J. C., C. T. Hann, S. S. Elder, C. S. Wang, L. Frunzio, L. Jiang, and R. J. Schoelkopf, "Single-shot number-resolved detection of microwave photons with error mitigation", Physical Review A **103**, 023705 (2021).

[29] Cybenko, G., "Reducing quantum computations to elementary unitary operations", Computing in Science & Engineering **3**, 27–32 (2001).

[30] Cygorek, M., M. Cosacchi, A. Vagov, V. M. Axt, B. W. Lovett, J. Keeling, and E. M. Gauger, "Simulation of open quantum systems by automated compression of arbitrary environments", Nature Physics, 1–7 (2022).

[31] Dassonneville, R., R. Assouly, T. Peronnin, P. Rouchon, and B. Huard, "Number-resolved photocounter for propagating microwave mode", Physical Review Applied **14**, 044022 (2020).

[32] Devoret, M. H. et al., "Quantum fluctuations in electrical circuits", Les Houches, Session LXIII **7**, 133–135 (1995).

[33] Devoret, M. H., J. M. Martinis, and J. Clarke, "Measurements of macroscopic quantum tunneling out of the zero-voltage state of a current-biased josephson junction", Physical Review Letters **55**, 1908 (1985).

[34] DiCarlo, L., J. M. Chow, J. M. Gambetta, L. S. Bishop, B. R. Johnson, D. Schuster, J. Majer, A. Blais, L. Frunzio, S. Girvin, et al., "Demonstration of two-qubit algorithms with a superconducting quantum processor", Nature **460**, 240–244 (2009).

[35] Didier, N., J. Bourassa, and A. Blais, "Fast quantum nondemolition readout by parametric modulation of longitudinal qubit-oscillator interaction", Physical Review Letters **115**, 203601 (2015).

[36] Dierksen, M. and S. Grimme, "An efficient approach for the calculation of franck–condon integrals of large molecules", The Journal of Chemical Physics **122**, 244101 (2005).

[37] Doktorov, E., I. Malkin, and V. Man'Ko, "Dynamical symmetry of vibronic transitions in polyatomic molecules and the franck-condon principle", Journal of Molecular Spectroscopy **64**, 302–326 (1977).

[38] Domcke, W., D. Yarkony, and H. Köppel, *Conical intersections: electronic structure, dynamics & spectroscopy*, Vol. 15 (World Scientific, 2004).

[39] Domcke, W. and D. R. Yarkony, "Role of conical intersections in molecular spectroscopy and photoinduced chemical dynamics", Annual Review of Physical Chemistry **63**, 325–352 (2012).

[40] Duan, H.-G. and M. Thorwart, "Quantum mechanical wave packet dynamics at a conical intersection with strong vibrational dissipation", The Journal of Physical Chemistry Letters **7**, 382–386 (2016).

[41] Dumke, R., M. Volk, T. Müther, F. Buchkremer, G. Birkl, and W. Ertmer, "Micro-optical realization of arrays of selectively addressable dipole traps: a scalable configuration for quantum computation with atomic qubits", Physical Review Letters **89**, 097903 (2002).

[42] Dunning Jr, T. H., "Gaussian basis sets for use in correlated molecular calculations. i. the atoms boron through neon and hydrogen", The Journal of Chemical Physics **90**, 1007–1023 (1989).

[43] Duschinsky, F., "The importance of the electron spectrum in multi atomic molecules. concerning the franck-condon principle", Acta Physicochim. URSS **7**, 551–566 (1937).

[44] Eickbusch, A., V. Sivak, A. Z. Ding, S. S. Elder, S. R. Jha, J. Venkatraman, B. Royer, S. Girvin, R. J. Schoelkopf, and M. H. Devoret, "Fast universal control of an oscillator with weak dispersive coupling to a qubit", arXiv preprint arXiv:2111.06414 (2021).

[45] Elder, S. S., C. S. Wang, P. Reinhold, C. T. Hann, K. S. Chou, B. J. Lester, S. Rosenblum, L. Frunzio, L. Jiang, and R. J. Schoelkopf, "High-fidelity measurement of qubits encoded in multilevel superconducting circuits", Physical Review X **10**, 011001 (2020).

[46] Elstner, N. and H. Monien, "Dynamics and thermodynamics of the bose-hubbard model", Physical Review B **59**, 12184 (1999).

[47] Feynman, R., "Simulating physics with computers", International Journal of Theoretical Physics **21** (1982).

[48] Foster, R. M., "A reactance theorem", Bell System technical journal **3**, 259–267 (1924).

[49] Frattini, N., V. Sivak, A. Lingenfelter, S. Shankar, and M. Devoret, "Optimizing the nonlinearity and dissipation of a snail parametric amplifier for dynamic range", Physical Review Applied **10**, 054020 (2018).

[50] Frattini, N., U. Vool, S. Shankar, A. Narla, K. Sliwa, and M. Devoret, "3-wave mixing josephson dipole element", Applied Physics Letters **110**, 222603 (2017).

[51] Frattini, N. E., "Three-wave mixing in superconducting circuits: stabilizing cats with snails", PhD thesis (Yale University, 2021).

[52] Frisch, M. J., G. W. Trucks, H. B. Schlegel, G. E. Scuseria, M. A. Robb, J. R. Cheeseman, G. Scalmani, V. Barone, G. A. Petersson, H. Nakatsuji, et al., *Gaussian 16, revision a.03, gaussian, inc., wallingford, ct.* (2016) `https://gaussian.com/citation_a03/`.

[53] Gambetta, J., A. Blais, M. Boissonneault, A. A. Houck, D. Schuster, and S. M. Girvin, "Quantum trajectory approach to circuit qed: quantum jumps and the zeno effect", Physical Review A **77**, 012112 (2008).

[54] Gambetta, J., W. Braff, A. Wallraff, S. Girvin, and R. Schoelkopf, "Protocols for optimal readout of qubits using a continuous quantum nondemolition measurement", Physical Review A **76**, 012325 (2007).

[55] Gao, Y. Y., "Multi-cavity operations in circuit quantum electrodynamics", PhD thesis (Yale University, 2018).

[56] Gao, Y. Y., B. J. Lester, K. S. Chou, L. Frunzio, M. H. Devoret, L. Jiang, S. Girvin, and R. J. Schoelkopf, "Entanglement of bosonic modes through an engineered exchange interaction", Nature **566**, 509–512 (2019).

[57] Gao, Y. Y., B. J. Lester, Y. Zhang, C. Wang, S. Rosenblum, L. Frunzio, L. Jiang, S. Girvin, and R. J. Schoelkopf, "Programmable interference between two microwave quantum memories", Physical Review X **8**, 021073 (2018).

[58] Garg, A., J. N. Onuchic, and V. Ambegaokar, "Effect of friction on electron transfer in biomolecules", The Journal of Chemical Physics **83**, 4491–4503 (1985).

[59] Gersch, H. and G. Knollman, "Quantum cell model for bosons", Physical Review **129**, 959 (1963).

[60] Geva, E., R. Kosloff, and J. Skinner, "On the relaxation of a two-level system driven by a strong electromagnetic field", The Journal of Chemical Physics **102**, 8541–8561 (1995).

[61] Girvin, S. M. and K. Yang, *Modern condensed matter physics* (Cambridge University Press, 2019).

[62] Glazman, L. and G. Catelani, "Bogoliubov quasiparticles in superconducting qubits", SciPost Physics Lecture Notes, 031 (2021).

[63] Gleyzes, S., S. Kuhr, C. Guerlin, J. Bernu, S. Deleglise, U. B. Hoff, M. Brune, J.-M. Raimond, and S. Haroche, "Quantum jumps of light recording the birth and death of a photon in a cavity", Nature **446**, 297–300 (2007).

[64] Google AI Quantum and Collaborators, "Hartree-fock on a superconducting qubit quantum computer", Science **369**, 1084–1089 (2020).

[65] Goy, P., J. Raimond, M. Gross, and S. Haroche, "Observation of cavity-enhanced single-atom spontaneous emission", Physical Review Letters **50**, 1903 (1983).

[66] Greiner, M., O. Mandel, T. Esslinger, T. W. Hänsch, and I. Bloch, "Quantum phase transition from a superfluid to a mott insulator in a gas of ultracold atoms", Nature **415**, 39–44 (2002).

[67] Grimm, A., N. E. Frattini, S. Puri, S. O. Mundhada, S. Touzard, M. Mirrahimi, S. M. Girvin, S. Shankar, and M. H. Devoret, "Stabilization and operation of a kerr-cat qubit", Nature **584**, 205–209 (2020).

[68] Grimsley, H. R., S. E. Economou, E. Barnes, and N. J. Mayhall, "An adaptive variational algorithm for exact molecular simulations on a quantum computer", Nature Communications **10**, 1–9 (2019).

[69] Gunnarsson, D., J. Tuorila, A. Paila, J. Sarkar, E. Thuneberg, Y. Makhlin, and P. Hakonen, "Vibronic spectroscopy of an artificial molecule", Physical Review Letters **101**, 256806 (2008).

[70] Gustavsson, S., J. Bylander, F. Yan, P. Forn-Díaz, V. Bolkhovsky, D. Braje, G. Fitch, K. Harrabi, D. Lennon, J. Miloshi, et al., "Driven dynamics and rotary echo of a qubit tunably coupled to a harmonic oscillator", Physical Review Letters **108**, 170503 (2012).

[71] Hacohen-Gourgy, S., L. S. Martin, E. Flurin, V. V. Ramasesh, K. B. Whaley, and I. Siddiqi, "Quantum dynamics of simultaneously measured non-commuting observables", Nature **538**, 491–494 (2016).

[72] Hann, C. T., S. S. Elder, C. S. Wang, K. Chou, R. J. Schoelkopf, and L. Jiang, "Robust readout of bosonic qubits in the dispersive coupling regime", Physical Review A **98**, 022305 (2018).

[73] Heeres, R. W., P. Reinhold, N. Ofek, L. Frunzio, L. Jiang, M. H. Devoret, and R. J. Schoelkopf, "Implementing a universal gate set on a logical qubit encoded in an oscillator", Nature Communications **8**, 1–7 (2017).

[74] Heeres, R. W., B. Vlastakis, E. Holland, S. Krastanov, V. V. Albert, L. Frunzio, L. Jiang, and R. J. Schoelkopf, "Cavity state manipulation using photon-number selective phase gates", Physical Review Letters **115**, 137002 (2015).

[75] Heller, E. J., "The semiclassical way to molecular spectroscopy", Accounts of Chemical Research **14**, 368–375 (1981).

[76] Hempel, C., C. Maier, J. Romero, J. McClean, T. Monz, H. Shen, P. Jurcevic, B. P. Lanyon, P. Love, R. Babbush, et al., "Quantum chemistry calculations on a trapped-ion quantum simulator", Physical Review X **8**, 031022 (2018).

[77] Houck, A., J. Schreier, B. Johnson, J. Chow, J. Koch, J. Gambetta, D. Schuster, L. Frunzio, M. Devoret, S. Girvin, et al., "Controlling the spontaneous emission of a superconducting transmon qubit", Physical Review Letters **101**, 080502 (2008).

[78] Huggins, W. J., B. A. O'Gorman, N. C. Rubin, D. R. Reichman, R. Babbush, and J. Lee, "Unbiasing fermionic quantum monte carlo with a quantum computer", Nature, 1–5 (2022).

[79] Huh, J., G. G. Guerreschi, B. Peropadre, J. R. McClean, and A. Aspuru-Guzik, "Boson sampling for molecular vibronic spectra", Nature Photonics **9**, 615–620 (2015).

[80] Hulet, R. G., E. S. Hilfer, and D. Kleppner, "Inhibited spontaneous emission by a rydberg atom", Physical Review Letters **55**, 2137 (1985).

[81] Ithier, G., E. Collin, P. Joyez, P. Meeson, D. Vion, D. Esteve, F. Chiarello, A. Shnirman, Y. Makhlin, J. Schriefl, et al., "Decoherence in a superconducting quantum bit circuit", Physical Review B **72**, 134519 (2005).

[82] Jordan, P. and E. P. Wigner, "About the pauli exclusion principle", Z. Phys **47**, 14–75 (1928).

[83] Kandala, A., A. Mezzacapo, K. Temme, M. Takita, M. Brink, J. M. Chow, and J. M. Gambetta, "Hardware-efficient variational quantum eigensolver for small molecules and quantum magnets", Nature **549**, 242–246 (2017).

[84] Kandala, A., K. Temme, A. D. Córcoles, A. Mezzacapo, J. M. Chow, and J. M. Gambetta, "Error mitigation extends the computational reach of a noisy quantum processor", Nature **567**, 491–495 (2019).

[85] Kapit, E., M. Hafezi, and S. H. Simon, "Induced self-stabilization in fractional quantum hall states of light", Physical Review X **4**, 031039 (2014).

[86] Kendall, R. A., T. H. Dunning Jr, and R. J. Harrison, "Electron affinities of the first-row atoms revisited. systematic basis sets and wave functions", The Journal of Chemical Physics **96**, 6796–6806 (1992).

[87] Kjaergaard, M., M. E. Schwartz, J. Braumüller, P. Krantz, J. I.-J. Wang, S. Gustavsson, and W. D. Oliver, "Superconducting qubits: current state of play", Annual Review of Condensed Matter Physics **11**, 369–395 (2020).

[88] Koch, J., M. Y. Terri, J. Gambetta, A. A. Houck, D. I. Schuster, J. Majer, A. Blais, M. H. Devoret, S. M. Girvin, and R. J. Schoelkopf, "Charge-insensitive qubit design derived from the cooper pair box", Physical Review A **76**, 042319 (2007).

[89] Kou, A., W. Smith, U. Vool, R. Brierley, H. Meier, L. Frunzio, S. Girvin, L. Glazman, and M. Devoret, "Fluxonium-based artificial molecule with a tunable magnetic moment", Physical Review X **7**, 031037 (2017).

[90] Krastanov, S., V. V. Albert, C. Shen, C.-L. Zou, R. W. Heeres, B. Vlastakis, R. J. Schoelkopf, and L. Jiang, "Universal control of an oscillator with dispersive coupling to a qubit", Physical Review A **92**, 040303 (2015).

[91] Kühl, A. and W. Domcke, "Multilevel redfield description of the dissipative dynamics at conical intersections", The Journal of Chemical Physics **116**, 263–274 (2002).

[92] Kühner, T. D. and H. Monien, "Phases of the one-dimensional bose-hubbard model", Physical Review B **58**, R14741 (1998).

[93] Kurilovich, P. D., V. D. Kurilovich, J. Lebreuilly, and S. Girvin, "Stabilizing the laughlin state of light: dynamics of hole fractionalization", arXiv preprint arXiv:2111.01157 (2021).

[94] Leghtas, Z., G. Kirchmair, B. Vlastakis, R. J. Schoelkopf, M. H. Devoret, and M. Mirrahimi, "Hardware-efficient autonomous quantum memory protection", Physical Review Letters **111**, 120501 (2013).

[95] Lei, C. U., L. Krayzman, S. Ganjam, L. Frunzio, and R. J. Schoelkopf, "High coherence superconducting microwave cavities with indium bump bonding", Applied Physics Letters **116**, 154002 (2020).

[96] Lloyd, S. and S. L. Braunstein, "Quantum computation over continuous variables", in *Quantum information with continuous variables* (Springer, 1999), pp. 9–17.

[97] Low, G. H. and I. L. Chuang, "Optimal hamiltonian simulation by quantum signal processing", Physical Review Letters **118**, 010501 (2017).

[98] Lu, Y., S. Chakram, N. Leung, N. Earnest, R. K. Naik, Z. Huang, P. Groszkowski, E. Kapit, J. Koch, and D. I. Schuster, "Universal stabilization of a parametrically coupled qubit", Physical Review Letters **119**, 150502 (2017).

[99] Ma, R., B. Saxberg, C. Owens, N. Leung, Y. Lu, J. Simon, and D. I. Schuster, "A dissipatively stabilized mott insulator of photons", Nature **566**, 51–57 (2019).

[100] Malmqvist, P.-Å. and N. Forsberg, "Franck-condon factors for multidimensional harmonic oscillators", Chemical Physics **228**, 227–240 (1998).

[101] Martinis, J. M., M. H. Devoret, and J. Clarke, "Energy-level quantization in the zero-voltage state of a current-biased josephson junction", Physical Review Letters **55**, 1543 (1985).

[102] Martinis, J. M., M. H. Devoret, and J. Clarke, "Experimental tests for the quantum behavior of a macroscopic degree of freedom: the phase difference across a josephson junction", Physical Review B **35**, 4682 (1987).

[103] Martinis, J. M., M. H. Devoret, and J. Clarke, "Quantum josephson junction circuits and the dawn of artificial atoms", Nature Physics **16**, 234–237 (2020).

[104] McArdle, S., S. Endo, A. Aspuru-Guzik, S. C. Benjamin, and X. Yuan, "Quantum computational chemistry", Reviews of Modern Physics **92**, 015003 (2020).

[105] McClean, J. R., J. Romero, R. Babbush, and A. Aspuru-Guzik, "The theory of variational hybrid quantum-classical algorithms", New Journal of Physics **18**, 023023 (2016).

[106] Meschede, D., H. Walther, and G. Müller, "One-atom maser", Physical Review Letters **54**, 551 (1985).

[107] Michael, M. H., M. Silveri, R. Brierley, V. V. Albert, J. Salmilehto, L. Jiang, and S. M. Girvin, "New class of quantum error-correcting codes for a bosonic mode", Physical Review X **6**, 031006 (2016).

[108] Minev, Z. K., Z. Leghtas, S. O. Mundhada, L. Christakis, I. M. Pop, and M. H. Devoret, "Energy-participation quantization of josephson circuits", npj Quantum Information **7**, 1–11 (2021).

[109] Mirrahimi, M., Z. Leghtas, V. V. Albert, S. Touzard, R. J. Schoelkopf, L. Jiang, and M. H. Devoret, "Dynamically protected cat-qubits: a new paradigm for universal quantum computation", New Journal of Physics **16**, 045014 (2014).

[110] Mostame, S., P. Rebentrost, A. Eisfeld, A. J. Kerman, D. I. Tsomokos, and A. Aspuru-Guzik, "Quantum simulator of an open quantum system using superconducting qubits: exciton transport in photosynthetic complexes", New Journal of Physics **14**, 105013 (2012).

[111] Motzoi, F., J. M. Gambetta, P. Rebentrost, and F. K. Wilhelm, "Simple pulses for elimination of leakage in weakly nonlinear qubits", Physical Review Letters **103**, 110501 (2009).

[112] Murch, K., U. Vool, D. Zhou, S. Weber, S. Girvin, and I. Siddiqi, "Cavity-assisted quantum bath engineering", Physical Review Letters **109**, 183602 (2012).

[113] Naik, R., N. Leung, S. Chakram, P. Groszkowski, Y. Lu, N. Earnest, D. McKay, J. Koch, and D. Schuster, "Random access quantum information processors using multimode circuit quantum electrodynamics", Nature Communications **8**, 1–7 (2017).

[114] Nakamura, Y., Y. A. Pashkin, and J. Tsai, "Coherent control of macroscopic quantum states in a single-cooper-pair box", Nature **398**, 786–788 (1999).

[115] Nielsen, M. A. and I. Chuang, *Quantum computation and quantum information*, 2002.

[116] Nigg, S. E., H. Paik, B. Vlastakis, G. Kirchmair, S. Shankar, L. Frunzio, M. Devoret, R. Schoelkopf, and S. Girvin, "Black-box superconducting circuit quantization", Physical Review Letters **108**, 240502 (2012).

[117] Nogrette, F., H. Labuhn, S. Ravets, D. Barredo, L. Béguin, A. Vernier, T. Lahaye, and A. Browaeys, "Single-atom trapping in holographic 2d arrays of microtraps with arbitrary geometries", Physical Review X **4**, 021034 (2014).

[118] Noh, K., S. Girvin, and L. Jiang, "Encoding an oscillator into many oscillators", Physical Review Letters **125**, 080503 (2020).

[119] O'Malley, P. J., R. Babbush, I. D. Kivlichan, J. Romero, J. R. McClean, R. Barends, J. Kelly, P. Roushan, A. Tranter, N. Ding, et al., "Scalable quantum simulation of molecular energies", Physical Review X **6**, 031007 (2016).

[120] Ofek, N., A. Petrenko, R. Heeres, P. Reinhold, Z. Leghtas, B. Vlastakis, Y. Liu, L. Frunzio, S. Girvin, L. Jiang, et al., "Extending the lifetime of a quantum bit with error correction in superconducting circuits", Nature **536**, 441–445 (2016).

[121] Oh, C., Y. Lim, Y. Wong, B. Fefferman, and L. Jiang, "Quantum-inspired classical algorithm for molecular vibronic spectra", arXiv preprint arXiv:2202.01861 (2022).

[122] Owens, C., A. LaChapelle, B. Saxberg, B. M. Anderson, R. Ma, J. Simon, and D. I. Schuster, "Quarter-flux hofstadter lattice in a qubit-compatible microwave cavity array", Physical Review A **97**, 013818 (2018).

[123] Owens, J. C., M. G. Panetta, B. Saxberg, G. Roberts, S. Chakram, R. Ma, A. Vrajitoarea, J. Simon, and D. Schuster, "Chiral cavity quantum electrodynamics", arXiv preprint arXiv:2109.06033 (2021).

[124] Ozawa, T., H. M. Price, A. Amo, N. Goldman, M. Hafezi, L. Lu, M. C. Rechtsman, D. Schuster, J. Simon, O. Zilberberg, et al., "Topological photonics", Reviews of Modern Physics **91**, 015006 (2019).

[125] Paesani, S., Y. Ding, R. Santagati, L. Chakhmakhchyan, C. Vigliar, K. Rottwitt, L. K. Oxenløwe, J. Wang, M. G. Thompson, and A. Laing, "Generation and sampling of quantum states of light in a silicon chip", Nature Physics **15**, 925–929 (2019).

[126] Paik, H., D. I. Schuster, L. S. Bishop, G. Kirchmair, G. Catelani, A. P. Sears, B. Johnson, M. Reagor, L. Frunzio, L. I. Glazman, et al., "Observation of high coherence in josephson junction qubits measured in a three-dimensional circuit qed architecture", Physical Review Letters **107**, 240501 (2011).

[127] Peropadre, B., G. G. Guerreschi, J. Huh, and A. Aspuru-Guzik, "Proposal for microwave boson sampling", Physical Review Letters **117**, 140505 (2016).

[128] Peruzzo, A., J. McClean, P. Shadbolt, M.-H. Yung, X.-Q. Zhou, P. J. Love, A. Aspuru-Guzik, and J. L. O'brien, "A variational eigenvalue solver on a photonic quantum processor", Nature Communications **5**, 1–7 (2014).

[129] Pfaff, W., C. J. Axline, L. D. Burkhart, U. Vool, P. Reinhold, L. Frunzio, L. Jiang, M. H. Devoret, and R. J. Schoelkopf, "Controlled release of multiphoton quantum states from a microwave cavity memory", Nature Physics **13**, 882–887 (2017).

[130] Place, A. P., L. V. Rodgers, P. Mundada, B. M. Smitham, M. Fitzpatrick, Z. Leng, A. Premkumar, J. Bryon, A. Vrajitoarea, S. Sussman, et al., "New material platform for superconducting transmon qubits with coherence times exceeding 0.3 milliseconds", Nature Communications **12**, 1–6 (2021).

[131] Polli, D., P. Altoe, O. Weingart, K. M. Spillane, C. Manzoni, D. Brida, G. Tomasello, G. Orlandi, P. Kukura, R. A. Mathies, et al., "Conical intersection dynamics of the primary photoisomerization event in vision", Nature **467**, 440–443 (2010).

[132] Preskill, J., "Quantum computing in the nisq era and beyond", Quantum **2**, 79 (2018).

[133] Purcell, E. M., H. C. Torrey, and R. V. Pound, "Resonance absorption by nuclear magnetic moments in a solid", Physical Review **69**, 37 (1946).

[134] Raimond, J.-M. and S. Haroche, "Exploring the quantum", Oxford University Press **82**, 86 (2006).

[135] Reagor, M., W. Pfaff, C. Axline, R. W. Heeres, N. Ofek, K. Sliwa, E. Holland, C. Wang, J. Blumoff, K. Chou, et al., "Quantum memory with millisecond coherence in circuit qed", Physical Review B **94**, 014506 (2016).

[136] Reck, M., A. Zeilinger, H. J. Bernstein, and P. Bertani, "Experimental realization of any discrete unitary operator", Physical Review Letters **73**, 58 (1994).

[137] Reed, M. D., L. DiCarlo, S. E. Nigg, L. Sun, L. Frunzio, S. M. Girvin, and R. J. Schoelkopf, "Realization of three-qubit quantum error correction with superconducting circuits", Nature **482**, 382–385 (2012).

[138] Reed, M. D., B. R. Johnson, A. A. Houck, L. DiCarlo, J. M. Chow, D. I. Schuster, L. Frunzio, and R. J. Schoelkopf, "Fast reset and suppressing spontaneous emission of a superconducting qubit", Applied Physics Letters **96**, 203110 (2010).

[139] Reinhold, P., "Controlling error-correctable bosonic qubits", PhD thesis (Yale University, 2019).

[140] Reinhold, P., S. Rosenblum, W.-L. Ma, L. Frunzio, L. Jiang, and R. J. Schoelkopf, "Error-corrected gates on an encoded qubit", Nature Physics **16**, 822–826 (2020).

[141] Rosenblum, S., Y. Y. Gao, P. Reinhold, C. Wang, C. J. Axline, L. Frunzio, S. M. Girvin, L. Jiang, M. Mirrahimi, M. H. Devoret, et al., "A cnot gate between multiphoton qubits encoded in two cavities", Nature Communications **9**, 1–6 (2018).

[142] Roushan, P., C. Neill, A. Megrant, Y. Chen, R. Babbush, R. Barends, B. Campbell, Z. Chen, B. Chiaro, A. Dunsworth, et al., "Chiral ground-state currents of interacting photons in a synthetic magnetic field", Nature Physics **13**, 146–151 (2017).

[143] Ruhoff, P. T., "Recursion relations for multi-dimensional franck-condon overlap integrals", Chemical Physics **186**, 355–374 (1994).

[144] Sank, D., Z. Chen, M. Khezri, J. Kelly, R. Barends, B. Campbell, Y. Chen, B. Chiaro, A. Dunsworth, A. Fowler, et al., "Measurement-induced state transitions in a superconducting qubit: beyond the rotating wave approximation", Physical Review Letters **117**, 190503 (2016).

[145] Sawaya, N. P. and J. Huh, "Quantum algorithm for calculating molecular vibronic spectra", The Journal of Physical Chemistry Letters **10**, 3586–3591 (2019).

[146] Schile, A. J. and D. T. Limmer, "Simulating conical intersection dynamics in the condensed phase with hybrid quantum master equations", The Journal of Chemical Physics **151**, 014106 (2019).

[147] Schneider, R. and W. Domcke, "S1-s2 conical intersection and ultrafast s2→ s1 internal conversion in pyrazine", Chemical Physics Letters **150**, 235–242 (1988).

[148] Schuster, D., A. A. Houck, J. Schreier, A. Wallraff, J. Gambetta, A. Blais, L. Frunzio, J. Majer, B. Johnson, M. Devoret, et al., "Resolving photon number states in a superconducting circuit", Nature **445**, 515–518 (2007).

[149] Seeley, J. T., M. J. Richard, and P. J. Love, "The bravyi-kitaev transformation for quantum computation of electronic structure", The Journal of Chemical Physics **137**, 224109 (2012).

[150] Seidner, L., G. Stock, A. Sobolewski, and W. Domcke, "A binitio characterization of the s 1–s 2 conical intersection in pyrazine and calculation of spectra", The Journal of Chemical Physics **96**, 5298–5309 (1992).

[151] Sharp, T. and H. Rosenstock, "Franck—condon factors for polyatomic molecules", The Journal of Chemical Physics **41**, 3453–3463 (1964).

[152] Shen, Y., Y. Lu, K. Zhang, J. Zhang, S. Zhang, J. Huh, and K. Kim, "Quantum optical emulation of molecular vibronic spectroscopy using a trapped-ion device", Chemical Science **9**, 836–840 (2018).

[153] Sherson, J. F., C. Weitenberg, M. Endres, M. Cheneau, I. Bloch, and S. Kuhr, "Single-atom-resolved fluorescence imaging of an atomic mott insulator", Nature **467**, 68–72 (2010).

[154] Shor, P. W., "Algorithms for quantum computation: discrete logarithms and factoring", in Proceedings 35th annual symposium on foundations of computer science (Ieee, 1994), pp. 124–134.

[155] Shor, P. W., "Scheme for reducing decoherence in quantum computer memory", Physical Review A **52**, R2493 (1995).

[156] Steane, A. M., "Error correcting codes in quantum theory", Physical Review Letters **77**, 793 (1996).

[157] Strathearn, A., P. Kirton, D. Kilda, J. Keeling, and B. W. Lovett, "Efficient non-markovian quantum dynamics using time-evolving matrix product operators", Nature Communications **9**, 1–9 (2018).

[158] Sun, L., A. Petrenko, Z. Leghtas, B. Vlastakis, G. Kirchmair, K. Sliwa, A. Narla, M. Hatridge, S. Shankar, J. Blumoff, et al., "Tracking photon jumps with repeated quantum non-demolition parity measurements", Nature **511**, 444–448 (2014).

[159] Szabo, A. and N. S. Ostlund, *Modern quantum chemistry: introduction to advanced electronic structure theory* (Courier Corporation, 2012).

[160] Tang, H. L., V. Shkolnikov, G. S. Barron, H. R. Grimsley, N. J. Mayhall, E. Barnes, and S. E. Economou, "Qubit-adapt-vqe: an adaptive algorithm for constructing hardware-efficient ansätze on a quantum processor", PRX Quantum **2**, 020310 (2021).

[161] Teller, E., "The crossing of potential surfaces.", Journal of Physical Chemistry **41**, 109–116 (1937).

[162] Thompson, R., G. Rempe, and H. Kimble, "Observation of normal-mode splitting for an atom in an optical cavity", Physical Review Letters **68**, 1132 (1992).

[163] Thorwart, M., E. Paladino, and M. Grifoni, "Dynamics of the spin-boson model with a structured environment", Chemical Physics **296**, 333–344 (2004).

[164] Touzard, S., A. Kou, N. Frattini, V. Sivak, S. Puri, A. Grimm, L. Frunzio, S. Shankar, and M. Devoret, "Gated conditional displacement readout of superconducting qubits", Physical Review Letters **122**, 080502 (2019).

[165] Touzard, S., "Stabilization of bosonic codes in superconducting circuits", PhD thesis (Yale University, 2019).

[166] Vlastakis, B., G. Kirchmair, Z. Leghtas, S. E. Nigg, L. Frunzio, S. M. Girvin, M. Mirrahimi, M. H. Devoret, and R. J. Schoelkopf, "Deterministically encoding quantum information using 100-photon schrödinger cat states", Science **342**, 607–610 (2013).

[167] Vool, U., S. Shankar, S. Mundhada, N. Ofek, A. Narla, K. Sliwa, E. Zalys-Geller, Y. Liu, L. Frunzio, R. Schoelkopf, et al., "Continuous quantum nondemolition measurement of the transverse component of a qubit", Physical Review Letters **117**, 133601 (2016).

[168] Walls, D. F., "Squeezed states of light", Nature **306**, 141–146 (1983).

[169] Wang, C., Y. Y. Gao, P. Reinhold, R. W. Heeres, N. Ofek, K. Chou, C. Axline, M. Reagor, J. Blumoff, K. Sliwa, et al., "A schrödinger cat living in two boxes", Science **352**, 1087–1091 (2016).

[170] Wang, C., X. Li, H. Xu, Z. Li, J. Wang, Z. Yang, Z. Mi, X. Liang, T. Su, C. Yang, et al., "Towards practical quantum computers: transmon qubit with a lifetime approaching 0.5 milliseconds", npj Quantum Information **8**, 1–6 (2022).

[171] Wang, C. S., J. C. Curtis, B. J. Lester, Y. Zhang, Y. Y. Gao, J. Freeze, V. S. Batista, P. H. Vaccaro, I. L. Chuang, L. Frunzio, et al., "Efficient multiphoton sampling of molecular vibronic spectra on a superconducting bosonic processor", Physical Review X **10**, 021060 (2020).

[172] Weedbrook, C., S. Pirandola, R. Garcıa-Patrón, N. J. Cerf, T. C. Ralph, J. H. Shapiro, and S. Lloyd, "Gaussian quantum information", Reviews of Modern Physics **84**, 621 (2012).

[173] Wendin, G., "Quantum information processing with superconducting circuits: a review", Reports on Progress in Physics **80**, 106001 (2017).

[174] Woon, D. E. and T. H. Dunning Jr, "Gaussian basis sets for use in correlated molecular calculations. iii. the atoms aluminum through argon", The Journal of Chemical Physics **98**, 1358–1371 (1993).

[175] Wu, Y., W.-S. Bao, S. Cao, F. Chen, M.-C. Chen, X. Chen, T.-H. Chung, H. Deng, Y. Du, D. Fan, et al., "Strong quantum computational advantage using a superconducting quantum processor", Physical Review Letters **127**, 180501 (2021).

[176] Yan, F., "Coherence characterization with a superconducting flux qubit through nmr approaches", PhD thesis (Massachusetts Institute of Technology, 2013).

[177] Yanay, Y., J. Braumüller, S. Gustavsson, W. D. Oliver, and C. Tahan, "Two-dimensional hard-core bose–hubbard model with superconducting qubits", npj Quantum Information **6**, 1–12 (2020).

[178] Zhang, Y., J. C. Curtis, C. S. Wang, R. Schoelkopf, and S. Girvin, "Drive-induced nonlinearities of cavity modes coupled to a transmon ancilla", Physical Review A **105**, 022423 (2022).

[179] Zhang, Y., B. J. Lester, Y. Y. Gao, L. Jiang, R. Schoelkopf, and S. Girvin, "Engineering bilinear mode coupling in circuit qed: theory and experiment", Physical Review A **99**, 012314 (2019).

[180] Zhou, C., P. Lu, M. Praquin, T.-C. Chien, R. Kaufman, X. Cao, M. Xia, R. Mong, W. Pfaff, D. Pekker, et al., "A modular quantum computer based on a quantum state router", arXiv preprint arXiv:2109.06848 (2021).